Low Blood Oxygen Saturation Quantification in Human Arterial and Venous Circulation

by

Jacobus Engelbertus Schoevers

Thesis presented in partial fulfilment of the requirements for the degree of

Master of Science in Mechatronic Engineering

at Stellenbosch University

Department of Mechanical and Mechatronic Engineering
Stellenbosch University
Private Bag X1, 7602 Matieland, South Africa

Supervisor: Prof C. Scheffer

March 2008

Declaration

I, the undersigned, hereby declare that the work contained in this thesis is my own original work and that I have not previously in its entirety or in part submitted it at any university for a degree.

Signature: .....
J.E. Schoevers

Date: .....

Abstract

Conventional pulse oximetry has limited accuracy in measuring blood oxygen saturation in low saturation and perfusion scenarios. This limits the application of pulse oximetry in patients suffering from peripheral vascular afflictions.

A novel pulse oximetry system is presented in this study which proposes solutions to these low saturation and perfusion issues. The presented system was designed to overcome the low perfusion issues by inducing an artificial pulse in the detected photoplethysmograph. A novel arterio-venous hypothesis was formulated to extract arterial and venous saturation data from this artificial photoplethysmograph using arterial-to-venous compliance ratios. Sensor wavelengths were selected to provide high and low saturation accuracy, followed by an *in vitro* sensor calibration procedure. System performance was validated by means of *in vivo* human studies.

In vivo results indicate good accuracy for high saturation, with limited accuracy in low saturation scenarios. The arterio-venous hypothesis was validated, indicating that venous saturation information can be extracted from the artificial PPG.

Although inconclusive, results indicate that the proposed system might be able to accurately monitor arterial and venous saturation in severe hypoperfusion scenarios with recommended hardware and calibration modifications. It is recommended that further studies into the presented system's performance are conducted.

Uittreksel

Konvensionele 'pulse oximetry' sisteme het beperkte akkuraatheid tydens die meting van bloed suurstof saturasie in lae saturasie en perfusie gevalle. Dit beperk die bruikbaarheid van 'pulse oximetry' in pasiënte wat ly aan perifere vaskulêre siektes.

'n Nuwe 'pulse oximetry' sisteem, wat oplossings vir hierdie lae saturasie en perfusie beperkings voorstel, word in hierdie studie aangebied. Die voorgestelde sisteem is ontwerp om die lae perfusie beperkings te oorkom deur 'n kunsmatige polsslag in die 'photoplethysmograph' te induseer. 'n Nuwe arterio-veneuse hipotese is geformuleer om arteriële en veneuse saturasie inligting uit hierdie kunsmatige polsslag te onttrek deur middel van 'n arteriële-teenoor-veneuse styfheids verhouding. Die golflengtes wat gebruik is in die sensors, is spesifiek gekies om hoë en lae saturasie akkuraatheid te verskaf. 'n *In vitro* kalibrasie prosedure is gevolg om die sensors vir hoë en lae saturasie te kalibreer, waarna die werkverrigting van die sisteem getoets is deur middel van 'n *in vivo* validasie prosedure.

Die *in vivo* resultate toon goeie akkuraatheid vir hoë saturasie, met beperkte akkuraatheid vir lae saturasie. Die arterio-veneuse hipotese is gevalideer, wat aandui dat veneuse saturasie wel uit die kunsmatige 'photoplethysmograph' onttrek kan word.

Alhoewel die resultate wat in hierdie studie aangebied word nie omvattend of beslissend is nie, dui dit egter aan dat die voorgestelde sisteem dalk in staat kan wees om arteriële en veneuse saturasie in uiters lae perfusie gevalle te meet. Verbeteringe sal egter aan die sisteem aangebring moet word in terme van hardeware en kalibrasie, om 'n meer gestandardiseerde metings metode te verseker. Verdere navorsing oor die werkverrigting van die voorgestelde sisteem word ook voorgestel.

Acknowledgements

I would like to express my sincere thanks to the following people who contributed to this thesis and helped to make this work possible:

- To my promoter, Prof. Cornie Scheffer. Thank you for all the support, valuable advice and freedom you granted me throughout the project.
- To Dr. Ricky Dippenaar. Thank you for all the effort you put in with the prototype testing and the advice you provided on the medical side of the project. Without your friendliness and help, this project would have been near impossible.
- Thank you to my family for always supporting me in my efforts.
- To Maria, thank you for all the prayers and always believing in me.

Dedication

To Mom

Contents

List of Figures

List of Tables

Nomenclature

Variables

α	Attenuation Coefficient
β	Refractive Increment
λ	Wavelength
σ	Optical Cross-section
Σ	Optical Coefficient
v	Red Blood Cell Volume
A	Attenuation
c	Cross-sectional Fraction
d	Finger Diameter
D	Diffusion Coefficient
F	Melanosome Fraction
H	Hematocrit
I	Light Intensity
l	Mean Photon Path Length
me	Molar Extinction Coefficient
ψ	Scalar Photon Density
ρ	Distance from Photon Source
S	Source Function
se	Specific Extinction Coefficient
SO_2	Blood Oxygen Saturation
V	Volume Fraction

x Concentration

Abbreviations

AC Alternating

APG Artificial Pulse Generator

APO Artificial Pulse Oximetry

$COHb$ Carboxyhaemoglobin

DAQ Data Acquisition Module

DC Static

DIC Disseminated Intravascular Coagulation

GUI Graphical User Interface

Hb Reduced Haemoglobin

HbO_2 Oxygenated Haemoglobin

LDF Laser Doppler Flowmetry

LED Light Emitting Diode

MCU Microcontroller Unit

$MetHb$ Methaemoglobin

NIRS Near-infrared Spectroscopy

PC Personal Computer

PPG Photoplethysmograph

PSU Power Supply Unit

R Normalized red/infrared Ratio

RBC Red Blood Cell

RS Reference Signal

SD Standard Deviation

USB Universal Serial Bus

Subscripts

a Arterial

ab Absorption

art	Arterial
c	Co-oximetry
der	Dermis
epi	Epidermis
g	General
ir	Infrared Wavelength
m	Mixed Arterial and Venous
o	Incident
p	Pulse Oximetry
r	Red Wavelength
s	Scattering
$sder$	Subdermis
t	Transmitted
tis	Tissue
v	Venous
ven	Venous

Chapter 1

Introduction

Continuous, non-invasive and reliable blood oxygen saturation (SO_2) information might play a vital role in the choice of medical intervention in treating patients suffering from peripheral vascular afflictions. In treating patients suffering from diseases such as *meningococcemia* and *diabetes mellitus*, medical intervention often includes the surgical removal of tissue affected by advanced hypoxia as a result of ischaemia (Milonovich, 2007). The decision to amputate digits or limbs affected by necrosis and the severity of the amputation are currently based on an intermittent and qualitative evaluation by the medical practitioner and not on a continuous and quantitative oxygen supply and consumption background. Although continuous saturation recording cannot serve as the sole parameter on which amputation is based, it might provide the medical practitioner with a tool to enable a more informed decision.

The current benchmark for the continuous and non-invasive monitoring of arterial saturation (S_aO_2) is pulse oximetry. The application of conventional pulse oximetry principles in monitoring peripheral vascular afflictions is however, limited. Although accurate for S_aO_2 values in excess of 70-80%, studies have shown a marked decrease in precision in pulse oximeter arterial saturation ($S_{pa}O_2$) values for S_aO_2 values below 70-80% (Jensen *et al.*, 1998; Carter *et al.*, 1998; Razi and Hossein, 2006; Bickler *et al.*, 2005). Additionally, pulse oximetry principally depends on the presence of a pulsatile arterial component. This pulsatile component is often missing in ischaemic tissue. As conventional pulse oximeters are rendered unusable by these ischaemic conditions and only measures S_aO_2, there is a need to develop

an alternative system capable of continuously and non-invasively monitoring both S_aO_2 and venous saturation (S_vO_2).

All pulse oximeters rely on the detection of an alternating (AC) absorption pattern, however small, in a detected photoplethysmograph (PPG), caused by pulsatile arterial blood. In the absence of this AC pattern, an error message is usually displayed. Although Chan and Smith (2003) addressed the absence of an AC pattern by inducing an artificial AC pattern in the PPG, a system specifically designed for $S_{pa}O_2$ and $S_{pv}O_2$ measurement accuracy in low saturation and severe hypoperfusion scenarios is still needed.

This study presents the development of a modified pulse oximetry system to non-invasively monitor $S_{pa}O_2$ and $S_{pv}O_2$ in low saturation and severe hypoperfusion scenarios. The selection of the sensor hardware to facilitate low saturation measurement is discussed, followed by a design overview of an artificial pulse generator for low perfusion applications. Thereafter, a system calibration by means of an *in vitro* calibration procedure, to facilitate low saturation accuracy, is presented. An *in vivo* human validation procedure and results are presented to validate system performance in differing physiological and saturation scenarios. Throughout the calibration and validation procedures, results were tested against a photon diffusion theory model provided by Schmitt (1991), which was modified to incorporate the effect of venous pulsations.

It is concluded that the designed system, as presented in this thesis, is not suited for repeatable and accurate measurement of $S_{pa}O_2$ and $S_{pv}O_2$ in low saturation and perfusion scenarios. The validation results do however seem to indicate that continuous and non-invasive monitoring of $S_{pa}O_2$ and $S_{pv}O_2$ could possibly be achieved with the designed system if specific adjustments are made to improve measurement repeatability.

Chapter 2

Background

2.1 Blood Oxygen Saturation

The efficient regulation of oxygen absorption and distribution by the cardiopulmonary and cardiovascular systems is of cardinal importance to human wellbeing. If tissue is deprived of a sufficient supply of oxygen for an extended period, cell damage occurs which may eventually result in extended necrosis. On the other hand, a surplus of oxygen can result in brain damage in neonatal patients. The oxygen content of blood is thus an important indicator of cardiopulmonary and cardiovascular function, resulting in some forms of blood oxygen content monitoring being regarded as the fifth vital sign.

Oxygen is transported by blood in two forms, namely, as solute in blood plasma and bound to the pigment haemoglobin, found in red blood cells (RBCs). Approximately 1.5% of the oxygen content of arterial blood is dissolved in blood plasma, the remaining 98.5% is bound to haemoglobin (Martini and Bartholomew, 2003). It can thus be safely assumed that the oxygen content of RBCs is a good representation of the overall oxygen content of blood. Blood oxygen content is usually described in terms of partial pressure or saturation, and although partial oxygen pressure can be related to oxygen saturation, only the latter is important in the context of this study.

SO_2 is the concentration of oxygenated haemoglobin relative to the total concentration of haemoglobin in blood. As such, it is usually expressed as a percentage value. Adult blood usually contains four species of haemoglobin, namely oxy-

genated haemoglobin (HbO_2), reduced haemoglobin (Hb), methaemoglobin ($MetHb$) and carboxyhaemoglobin ($COHb$) (Kamat, 2002). As $MetHb$ and $COHb$ do not bind oxygen, SO_2 can be defined as functional and fractional, with functional SO_2 neglecting the effects of $MetHb$ and $COHb$, while fractional SO_2 takes the effects of $MetHb$ and $COHb$ into account. Unless otherwise stated, SO_2 values stated in this study will be functional.

SO_2 values in the human circulatory system differ according to the location of blood in the system. Arterial blood has a high SO_2, while venous blood has a lower SO_2. As such, arterial and venous saturation are expressed as S_aO_2 and S_vO_2, respectively. Additionally, the measurement system used is normally also indicated, with S_aO_2 indicating arterial SO_2 measured by means of a co-oximetry blood gas analysis and S_pO_2 indicating arterial SO_2 measured by means of pulse oximetry. Historically, the focus of SO_2 measurements has been on arterial oxygen content, not necessitating further expansion of the SO_2 term. In this study however, arterial and venous SO_2 values, measured by means of co-oximetry and pulse oximetry, were discussed. Arterial SO_2 measured by means of co-oximetry was thus stated as $S_{ca}O_2$, while venous SO_2 measured by means of pulse oximetry was stated as $S_{pv}O_2$.

2.2 SO_2 Monitoring Systems

Existing systems for measurement of the O_2 content of blood were studied to identify the system best suited to the system specifications of this study. SO_2 monitoring systems can be divided in two categories, namely, invasive and non-invasive. Only non-invasive measurement of SO_2 was important in the context of this study.

2.2.1 Transcutaneous Clark Electrode

The Clark electrode is a polarographic method of measuring the partial pressure of O_2 (pO_2) in a blood sample. Although not a direct SO_2 measurement method, pO_2 can be related to SO_2. Two electrodes, connected by an external bias source, are immersed in an electrolytic potassium chloride solution. The potassium chloride solution is separated from the blood sample by means of an O_2-permeable Teflon or polypropylene membrane that allows O_2 to diffuse into the electrolytic solution.

pO_2 is measured by means of an oxidation/reduction reaction occurring at the electrodes. O_2 is reduced at a noble metal cathode to form hydroxyl ions. This reaction consumes 4 electrons. The hydroxyl ions diffuse to a silver anode where silver is oxidised to silver ions. This reaction liberates a single electron. The silver ions combine with chloride ions to form silver chloride. Electrons liberated in the oxidation reaction at the anode migrates to the cathode to enable the reduction reaction. The flow of electrons, and thus the current, is directly proportional to the rate of O_2 reduction at the cathode and thus the concentration of O_2 in the electrolytic solution. The concentration of O_2 in the solution is representative of the rate of O_2 diffusion across the membrane and thus pO_2. pO_2 is thus directly proportional to current flowing through the external bias source.

The transcutaneous Clark electrode is a slightly modified version of the polarographic Clark electrode. Small heating coils are included in the housing of the sensor to cause vasodilation of the skin, enabling non-invasive pO_2 measurement through the skin (Enderle *et al.*, 2005).

2.2.2 Blood Oxygen Level Dependent Magnetic Resonance Imaging (BOLD MRI)

MRI is a three-dimensional imaging method that is frequently applied in medical scenarios. Medical MRI frequently uses the interaction of hydrogen atoms with an applied magnetic field to form an image of the human body. A hydrogen atom contains a proton in its nucleus, resulting in a small magnetic field as the nucleus spins. The frequency of this magnetic moment is termed the Larmor frequency and is unique to hydrogen. If the atom is placed in a strong magnetic field, the hydrogen atom aligns with the magnetic field so that the axis of nucleus spin is aligned with the magnetic field. Should a radio frequency magnetic field be applied perpendicular to the static magnetic field at the Larmor frequency, the hydrogen atoms are exited to a state where the axis of nucleus spin is not aligned with the static field. When the perpendicular magnetic field is shut off, the hydrogen atoms return to the equilibrium state, emitting a radio frequency signal that is detected by the coils of the static field magnet. These radio frequency signals are used to form a spatial image of tissue, based on the relative concentrations of hydrogen atoms in the tissue.

Functional MRI is a form of MRI that is used to measure brain activity. The increase in neural activity is monitored by means of a mechanism referred to as the blood-oxygen-level dependent (BOLD) effect. Changes in neural activity calls for changes in the O_2 supply. By monitoring the O_2 content of regional blood vessels, an indication of neural activity can be obtained. The monitoring of O_2 is achieved by means of measuring the magnetic susceptibility of haemoglobin, with oxygenated blood being dimagnetic and deoxygenated blood being paramagnetic (Enderle *et al.*, 2005). Signal processing is conducted by subtracting MRI images of the brain before and after task initiation. This is done because the changes in magnetic parameters in BOLD MRI are very small and result in BOLD MRI readings being reported as percentage change in the BOLD MRI signal (Enderle *et al.*, 2005).

2.2.3 Digital Infrared Thermal Imaging (DITI)

DITI is not an O_2 content sensor, but rather a measure of tissue perfusion. Tissue perfusion is closely related to the supply of O_2.

DITI is a non-invasive method of measuring skin surface temperature. An infrared camera is used to measure skin temperature by relating the infrared radiation of skin to skin temperature by means of Planck's Law (Jones and Plassmann, 2002). A spectral image is formed, relating different skin temperatures to different colours.

Skin surface temperature is indicative of the extent of dermal perfusion (Jones and Plassmann, 2002). Dermal vasodilation will result in increased blood flow in the dermis, resulting in an increase in skin surface temperature. As modern DITI systems have a sensitivity of up to 0.1 degrees Celsius, minor changes in tissue perfusion can be detected. As such, DITI can provide valuable information on a range of physiological processes that affect blood perfusion.

2.2.4 Pulse Oximetry

Pulse oximetry is a non-invasive method of directly measuring SO_2. This method is used extensively in modern ICU's and general monitoring.

SO_2 measurement is based upon the different optical absorption properties of HbO_2 and Hb. Light, at two different wavelengths specifically chosen to optimise

system performance, is shone onto the tissue of interest. A photodetector detects the intensity of light that is transmitted through, or reflected from, the tissue. These intensities are then related to SO_2. The detected light from the vascular bed has alternating intensity levels as a result of pulsatile arterial blood, enabling the pulse oximetry system to discern between the absorption by blood or bloodless tissue, skin and bone. By considering only the optical absorption of blood, the SO_2 of blood is then calculated. This measurement method will be discussed in more detail in Chapter 3.

2.2.5 Near-Infrared Spectroscopy

Near-infrared spectroscopy (NIRS) is a optical method of non-invasively measuring tissue oxygen saturation.

The use of NIRS to measure the concentration of different tissue chromophores is based upon a modified version of Beer-Lambert's law (Elwell and Hebden, 1999), which states that the absorption of light in an optically absorbing compound is related to optical pathlength, chromophore absorption coefficients and the concentrations of all chromophores in the compound. Beer-Lambert's law will be discussed in more detail in Section 3.1. Modern spectrometers, utilizing NIRS principles, usually utilize four laser diodes and a photodetector to measure reflected light intensities from the tissue of interest. These intensities are then related to tissue chromophore concentrations by means of the modified Beer-Lambert's law that accounts for variations in optical pathlength and scattering losses (Elwell and Hebden, 1999).

2.2.6 Laser Doppler Flowmetry

Laser Doppler Flowmetry (LDF) is an established method of non-invasively monitoring relative changes in tissue perfusion. As such it is not a O_2 content sensor, but is used for monitoring blood flow in scenarios including heart monitoring, transluminar coronary angioplasty and tissue blood flow on the body surface (Enderle *et al.*, 2005).

LDF is based upon the Doppler phenomenon when a moving object causes a frequency shift in incident light. This frequency shift, called Doppler shift, can

be related to the velocity of the moving object. Low power laser light is reflected from the tissue of interest and collected by means of a light sensitive probe. The Doppler shift is then calculated and related to blood flow velocities in the tissue. These velocities are used as an indicator of tissue perfusion.

2.3 O_2 Monitoring in Low Saturation and Perfusion Scenarios

In patients suffering from peripheral vascular afflictions, low peripheral saturation and perfusion conditions are often present. Low perfusion conditions are also often present in surgical skin grafts. Medical practitioners treating these conditions might benefit from the continuous and non-invasive monitoring of the O_2 supply and demand scenarios at the affected tissue. The monitoring of ischaemic digits in patients suffering from low peripheral saturation and perfusion as a result of *meningococcemia* forms the basic motivation of this study, although the monitoring of conditions such as *diabetes mellitus*, surgical skin grafts or peripheral vascular disease might deliver analogous results.

Meningococcemia is a severe febrile systematic disease, characterized by an acute infection of the bloodstream and the resulting inflammation of the blood vessels, known as vasculitis (Ramos-e-Silva and Pereira, 2005; Wener, 2005). Individuals suffering from severe cases of *meningococcemia* often display large and widespread haemorrhagic purpuric lesions (Ramos-e-Silva and Pereira, 2005). Large purpuric and necrotic areas are characteristic of disseminated intravascular coagulation (DIC) present in severe cases of *meningococcemia*. Purpuric lesions on the knees and feet of a baby affected by *meningococcemia* can be seen in Figure 2.1.

Antibiotic administration is the standard treatment that is used, with penicillin G, chloranphenicol and some cephalosporins being the drugs of choice (Ramos-e-Silva and Pereira, 2005; Mahmud and Shadab, 2007; Milonovich, 2007). The restoration of circulatory function is also aggressively handled, while surgical removal of digits affected by advanced ischaemia or hypoperfusion might be necessary (Milonovich, 2007). The decision whether to amputate depends on a balance between a possible further progression of hypoxia into lesser affected tissues and saving a digit that can possibly recover some functionality.

Figure 2.1: Purpuric lesions on knees of baby

Recently, Dippenaar *et al.* (2006) studied the treatment of tissue ischaemia by means of medicinal leeches, *Hirudo Medicinalis*. While feeding, these leeches inject the tissue with saliva, containing active products that reduce and reverse many of the processes contributing toward tissue ischaemia. Dippenaar *et al.* (2006) applied *H. Medicinalis* leeches for four consecutive days to the left hand of a 5-week old female infant. A definite improvement in tissue perfusion was noted, with the largest improvement being noted after the first day's treatment. It was postulated that the improvement was due to the vasodilatory effects, improved capillary permeability, platelet inhibition and an attenuation in endothelial damage. Leech treatment on an ischaemic hand can be seen in Figure 2.2.

Evaluation of the degree of treatment success is currently based on a visual inspection of tissue perfusion, with conventional invasive and non-invasive O_2 monitoring methods rendered ineffective. An invasive blood gas analysis is rendered ineffective as a result of the advanced degree of coagulation present in the digits, the difficulty in obtaining a blood sample from the finger of a neonate and its intermittance. The measurement of pO_2 by means of a transcutaneous Clark electrode

Figure 2.2: *H. Medicinalis* treatment of ischaemia

is hindered by the dependence of measured values on the degree of tissue perfusion (Tremper, 1984). Although measured pO_2 values might be indicative of changes in tissue perfusion, a reliable and quantitative measure of the O_2 content of the blood would not be possible in extreme cases of ischaemia. BOLD MRI, on the other hand, is capable of providing qualitative measurements of blood oxygenation, but is limited by its intermittance and cost. As mentioned earlier, DITI is only capable of measuring tissue perfusion and not the O_2 content of blood. Although DITI has been used in studies on occlusive vascular disorders (Jones, 1998), the quantitative monitoring of tissue O_2 content is not possible. Conventional pulse oximetry is ineffective as a result of the absence of pulsatile blood behaviour in the occluded tissue. The measurement of tissue oxygen saturation by means of NIRS would be a good indicator of the status of the affected tissue, but due to a lack in available equipment and the cost of acquiring a suitable system, it was not a viable option. As with DITI, LDF values are only a relative measure of blood

perfusion and as such cannot provide a quantitative measurement of the O_2 status of ischaemic tissue.

Additionally, the O_2 content of venous blood might be an important indicator of the status of affected tissue. Normally, pO_2 in the arterial and venous circulation differs by approximately 60 mmHg (Martini and Bartholomew, 2003). This is indicative of healthy tissue, where O_2 is consumed and CO_2 is formed. In tissue affected by extended necrosis, the amount of O_2 consumed would be much less, resulting in a decrease in pO_2 difference between arterial and venous circulation. An elevated local venous pO_2 might thus be indicative of extended necrosis, although the validity of this statement would have to be tested in a further study. None of the O_2 monitoring methods mentioned above is suited to the continuous and non-invasive monitoring of S_vO_2 (or venous pO_2).

As mentioned earlier, the effective monitoring of the degree of medicinal leech treatment success on *meningococcemia* induced digital ischaemia forms the basic motivation for this study. This was attempted by measuring arterial and venous oxygen saturation at the affected site through the use of an adapted pulse oximetry system capable of operating in a non-pulsatile environment. By continuously and quantatively monitoring both arterial and venous SO_2 in the affected tissue, the medical practitioner might be able to make a more informed decision regarding other therapeutic modalities such as medicinal leeches or ultimately amputation.

Chapter 3

Pulse Oximetry

The measurement of SO_2, based on the light absorption properties of oxygenated and deoxygenated blood, is called oximetry. More particularly, oximetry is based upon the relative concentrations of oxygenated HbO_2 and reduced hemoglobin Hb in blood, as these are the major factors that determine SO_2. HbO_2 and Hb have different light absorption properties and the effects of their relative concentrations can be seen in the distinctly different colors of oxygenated and deoxygenated blood.

Pulse oximetry is a non-invasive form of oximetry, where HbO_2 and Hb concentrations, and thus SO_2, are determined based upon the distinctive light absorption behaviour of tissue due to the pulsatile behaviour of blood in the arterial branch of the vascular bed.

3.1 Operating Principle

Oximetry is based upon Beer-Lambert's Law, which states that the amount of light absorbed by an absorbing species dissolved in a non-absorbing compound is a function of the specific extinction coefficient (se) of the species, the mean photon path length through the species (l) and the concentration of the species (x). This law can be summarized as follows (Enderle *et al.*, 2005):

$$I_t = I_o \times 10^{-se.l.x} \tag{3.1}$$

or alternatively (Elwell and Hebden, 1999),

$$A = log_{10}\left[\frac{I_o}{I_t}\right] = se.l.x \tag{3.2}$$

with I_t the transmitted light intensity, I_o the incident light intensity and A the attenuation. This relationship only holds for a singular species dissolved in a non-absorbing compound. If more than one absorbing species is present in the non-absorbing compound, Equation 3.2 can be stated as follows (Elwell and Hebden, 1999):

$$A = log_{10}\left[\frac{I_o}{I_t}\right] = \left[se_1.x_1 + se_2.x_2 + se_3.x_3 + ... + se_n.x_n\right].l \tag{3.3}$$

where the combined factor $se.x$ is also called the absorption coefficient of the absorbing species. As can be seen from Equation 3.3, a non-absorbing medium containing three different absorbing species would require three different equations to solve for x if A, se and l was known.

Tissue contains a large number of different absorbing species. These consist of compounds contained in the skin, the dermis, bone and blood. To solve the oximetry form of Equation 3.3 for the concentrations of HbO_2 and Hb in tissue would require a large number of independent equations. This would not be a viable option. Fortunately, the light absorption behaviour of tissue has some very distinctive characteristics that enables the calculation of x for HbO_2 and Hb using only two independent equations.

Light absorption in tissue can be shown in the form of a photoplethysmograph (PPG), as seen in Figure 3.1a. This PPG is recorded using a pulse oximeter, shown in Figure 3.1b, consisting of two high output LEDs and a highly sensitive silicon photodetector. The LEDs are of different wavelengths, one typically in the red (660-700 nm) wavelength range and the other in the infrared (880-950 nm) wavelength range. Wavelengths are selected, based on the absorption coefficients of HbO_2 and Hb (Figure 3.2 (Prahl, 1998)), to maximize sensor sensitivity and repeatability (Mannheimer *et al.*, 1997). The pulse oximeter setup shown in Figure 3.1 is that of transmission pulse oximetry, whereas reflection pulse oximetry has the LEDs and photodetector on the same side of the finger or tissue. Light emmitted by the LEDs propagates through the finger and its absorbing species and is detected by the photodetector. The light intensity detected by the photodetector is represented by the PPG. The PPG shown in Figure 3.1 is that of only one LED, whereas typical

PPGs will have two different data sets, one for each LED. The individual LEDs are sequentially switched and the data acquired by the photodetector separated for each LED.

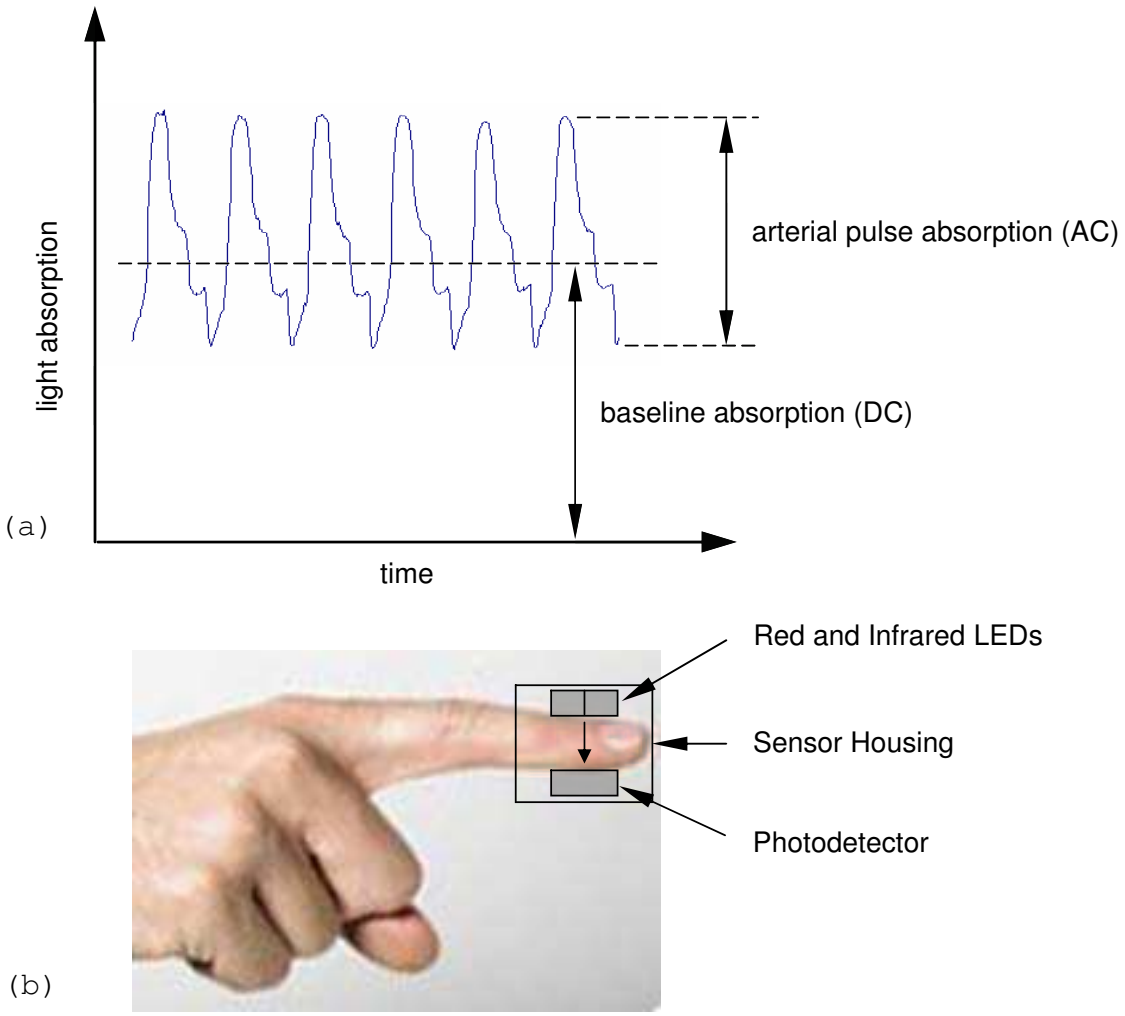

Figure 3.1: Photoplethysmograph Model and Transmission Pulse Oximeter

As can be seen from the PPG in Figure 3.1a, the light absorption of tissue has two distinct components, namely an arterial pulsatile (AC) component and a baseline component (DC). The AC component of the PPG is due to the modulation in photon path length as the arterial branch of the vascular bed expands and contracts during systole and diastole. The DC component of light absorption is due to the static absorption of skin and bloodless tissue, as well as the absorption

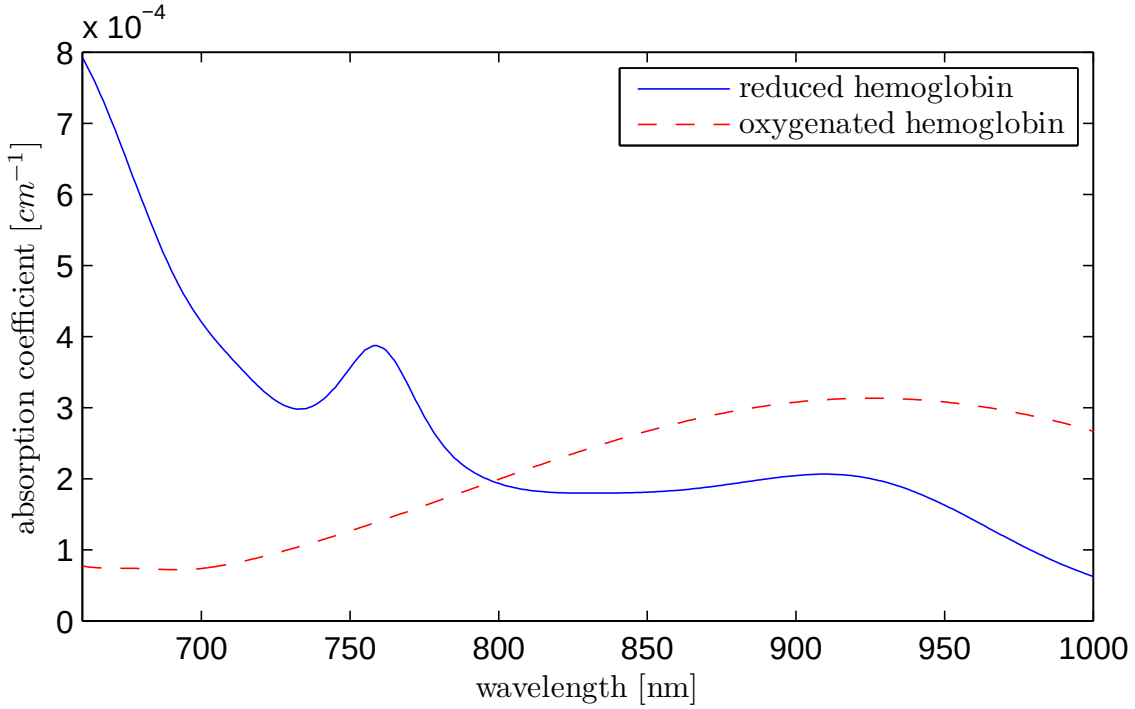

Figure 3.2: Absorption Spectrum for Oxygenated and Deoxygenated Haemoglobin (Prahl, 1998)

of resident arterial and venous blood. The AC component is thus only dependent on pulsatile blood behaviour, while the DC component includes the absorption by the rest of the light absorbing species. The absorption by blood can thus be separated from the absorption by the rest of the absorbing species by simply separating the AC and DC components of the PPG.

The amplitude of the AC component of the PPG is dependent on S_aO_2, as the relative concentrations of HbO_2 and Hb in the arterial blood determine the absorption of light, as stated by Equation 3.3. HbO_2 and Hb are not the only strong absorbers in blood, however, with methaemoglobin ($MetHb$) and carboxy-haemoglobin ($COHb$) also having strong absorption coefficients in the selected wavelength ranges. The effect of these additional haemoglobin species are usually neglected due to their small concentrations in blood under normal conditions (Kamat, 2002). This gives rise to the term 'functional haemoglobin saturation', as opposed to 'fractional haemoglobin saturation' where the effects of $MetHb$ and $COHb$ are included. The DC component is also dependent on S_aO_2 to a lesser extent, as the residual arterial blood also absorbs light according to HbO_2 and Hb

concentrations. Additionally, the incident light intensity also affects the AC component amplitude. Normalizing the original AC component with the DC component compensates for the residual blood and incident light intensity variations (Sinex, 1999). The normalized AC component of the PPG is now relatively independent of any DC component variations (Enderle *et al.*, 2005).

As can be seen from Equation 3.3, the calculation of the concentrations of HbO_2 and Hb requires two different equations, resulting in a need for two different PPGs. This is the reasoning behind using two LEDs in a pulse oximeter probe. In fractional haemoglobin saturation calculations, more PPGs are needed to satisfy Equation 3.2 for more variables, resulting in up to five LEDs being using in more comprehensive systems (Aoyagi, 2003). The normalized AC components of the red PPG is divided by the normalized AC component of the infrared PPG to obtain a normalized ratio R that is highly dependent on the concentrations of HbO_2 and Hb, and thus S_aO_2, and relatively independent of light absorption by the DC species. The calculation of R can be seen below as Equation 3.4.

$$R = \frac{AC_r/DC_r}{AC_{ir}/DC_{ir}} \tag{3.4}$$

In early pulse oximeters, R was used in conjunction with Beer-Lambert's Law to calculate $S_{pa}O_2$. Beer-Lambert's Law does not however, take the effects of light scattering, reflection and diffusion into account, all being major factors in light propagation through tissue (Stabile and Reynolds, 2002), leading to gross overestimation of $S_{pa}O_2$ (Sinex, 1999). Scattering, reflection and diffusion factors result in Beer-Lambert's Law being inaccurate in most scenarios, especially low saturation conditions (Coetzee and Elghazzawi, 2000). Several alternative and more complicated models have been developed that take scattering, reflection and diffusion into account (Schmitt, 1991; de Kock and Tarassenko, 1991, 1993; Lindberg *et al.*, 1995), but the validity of these models under a wide range of physiological scenarios are questionable (Coetzee and Elghazzawi, 2000).

Most pulse oximeter manufacturers thus resort to an empirical calibration approach to relate R to S_aO_2. Two calibration approaches exist, namely *in vivo* and *in vitro* calibration procedures. These procedures will be discussed in more detail in Section 4.5.1, but manufacturers currently employ *in vivo* desaturation procedures to obtain the calibration curves (Webster, 1997). These calibration procedures

result in calibration curves where R is related to S_aO_2 under conditions closely resembling normal physiological conditions. R values calculated from the red and infrared PPGs are compared to the calibration curves, resulting in the calculated $S_{pa}O_2$ value.

3.2 Pulse Oximetry in Low Saturation Value Scenarios

The proliferation of pulse oximeters in modern ICUs has led to a large variety of studies into pulse oximeter performance, in both high and low saturation scenarios (Lee *et al.*, 2002; Bickler *et al.*, 2005; Razi and Hossein, 2006; Lindholm *et al.*, 2007; Van de Louw *et al.*, 2001; Severinghaus *et al.*, 1989; Severinghaus and Naifeh, 1987; Uystepruyst *et al.*, 2000; Carter *et al.*, 1998). The above mentioned studies show increases or decreases in $S_{pa}O_2$ bias (mean difference between measurement method and golden standard) and a decrease in $S_{pa}O_2$ precision (standard deviation (SD) of error) as S_aO_2 decreases below 70-80%, while $S_{pa}O_2$ values above 70-80% generally agree closely with S_aO_2.

In a recent meta-analysis of pulse oximetry performance, Jensen *et al.* (1998) concluded that historically, pulse oximeters were accurate to within ±2% in the S_aO_2 range 70-100%, but that accuracy deteriorates rapidly for $S_aO_2 \leq 70\%$. These data were collected by studying pulse oximeter performance studies from 1974 to 1994.

Carter *et al.* (1998) compared the performance of *Ohmeda 3700* and *Hewlett-Packard M1020A* pulse oximeters in paediatric patients with S_aO_2 readings below 90%. Bias and precision values for the *Ohmeda* system was -2.8±4.8% ($S_aO_2 \geq 75\%$) and -0.8±8% ($S_aO_2 \leq 75\%$). A marked increase in $S_{pa}O_2$ variability for $S_aO_2 \leq 75\%$ was thus observed, although bias was improved.

In a study done by Razi and Hossein (2006), the performance of a pulse oximeter on 152 subjects diagnosed with chronic obstructive pulmonary disease was analyzed. $S_{pa}O_2$ and $S_{ca}O_2$ values measured for $S_aO_2 \geq 90\%$ was 94.17±3.71% and 94.37±2.18% (mean±SD), while $S_{pa}O_2$ and $S_{ca}O_2$ values measured for $S_aO_2 \leq 80\%$ was 74.4±10.24% and 70.63±9.13%. Discrepancies between $S_{pa}O_2$ and $S_{ca}O_2$ thus became more pronounced for $S_aO_2 \leq 80\%$.

Bickler *et al.* (2005) studied the effect of skin pigmentation on $S_{pa}O_2$ in a group of 11 subjects with darkly pigmented skin and 10 subjects with lightly pigmented skin. $S_{pa}O_2$ values for the darkly pigmented subjects showed substantial overestimation of S_aO_2 in the range 60-70%. $S_{pa}O_2$ values for the lightly pigmented subjects showed bias values in the range -1.62 to 1.91% for the three tested pulse oximeters, while precision values were within the range $\pm$ 1.6 to $\pm$ 3.42%.

It can thus be concluded from the above-mentioned studies, that $S_{pa}O_2$ bias and precision deteriorates for S_aO_2 $\leq$80%. The studies do not agree on over or underestimation of S_aO_2, but do indicate a pronounced decrease in precision. These errors may be due to a number of reasons.

Firstly, there is the issue of pulse oximeter calibration. As mentioned in Section 3.1, most pulse oximeter manufacturers use an *in vivo* calibration procedure. During this procedure, R values are collected on human volunteers that are systematically desaturated by breathing air with an increasingly leaner mixture of oxygen (Sinex, 1999). $S_{ca}O_2$ values are measured at each data collection stage using a reference *in vitro* co-oximetry system. A general calibration curve is obtained by fitting the R and $S_{ca}O_2$ data of a large number of volunteers. This calibration procedure can only be conducted for S_aO_2 $\geq$75-80% due to ethical ramifications such as possible hypoxic brain damage for S_aO_2 $\leq$75-80% (Stabile and Reynolds, 2002; Sinex, 1999). Extrapolation of the data for S_aO_2 $\geq$75-80% is used for S_aO_2 below this level (Kelleher, 1988; Wukitsch *et al.*, 1988). The inherent calibration errors as a result of the data extrapolation might be a reason for deteriorating performance at low S_aO_2 values.

Secondly, slight variations in LED output wavelengths generate large variations in calculated $S_{pa}O_2$ values in low saturation scenarios (Carter *et al.*, 1998). The effects of LED output wavelength discrepancies, as described by Wahr and Tremper (1995), although negligible at high S_aO_2, become more pronounced at low S_aO_2.

Thirdly, the high absorption coefficient of Hb causes strong absorption of the red wavelength at low saturations. This causes a disproportionally small AC component in the red PPG. To effectively use the red PPG, the sensor hardware compensates for the increased red wavelength absorption by increasing LED driving current and photodetector gain to increase the AC amplitude of the red PPG. Unfortunately, this also amplifies electronic and physiological noise, resulting in misleading $S_{pa}O_2$ values (Stabile and Reynolds, 2002; Reynolds *et al.*, 1992).

Fourthly, amplified multiple scattering effects, as described by Mannheimer *et al.* (1997) and Shimada *et al.* (1984), may also affect low $S_{pv}O_2$ calculations. In these studies, it was postulated that these scattering effects are due to discrepancies between changes in the mean photon path lengths (l) in Equation 3.1) of the two wavelengths used. The changes in mean photon path length resulted from tissue perturbations for calibration and *in vivo* use. Tissue perturbations were described as physiological tissue changes that significantly affect light propagation properties. It was postulated that mean photon path length mismatches are negligible at high saturation values, but that it becomes more important in low saturation scenarios.

Most studies on measures to improve pulse oximeter accuracy in low saturation scenarios have focused either on improving the accuracy of the calibration curves (Zonios *et al.*, 2004; Mannheimer and Porges, 2004) or minimizing the effects of tissue perturbations on pulse oximeter performance (Casciani *et al.*, 1995; Mannheimer *et al.*, 1997).

Zonios *et al.* (2004) presented a semi-empirical calibration approach to improve the accuracy of calibration curves at low saturations. The authors presented an exact solution to the transmission of light through human tissue by grouping all calibration uncertainties together into a single uncertainty parameter. This uncertainty parameter was included due to the fact that the number of unknowns in the exact solution of the pulse oximetry problem exceeds the number of known parameters. By grouping all the calibration unknowns into a single parameter, the application of the exact solution to pulse oximetry was made possible. The uncertainty parameter was empirically determined during *in vivo* desaturation studies on sheep fetuses where at best linear fit R and $S_{ca}O_2$ data was conducted. This semi-empirical calibration study displayed marked improvements in $S_{pa}O_2$ bias and precision.

In patent documentation presented by Mannheimer and Porges (2004), the authors described a pulse oximetry system with a piece-wise calibration curve. Modern pulse oximeters utilize physiological parameters to select an appropriate calibration curve from different sets of *in vivo* calibration curves stored in the system (Nellcor Technical Staff, 2004). Mannheimer and Porges (2004) developed this concept further by developing piece-wise calibration curves that take the range of $S_{pa}O_2$ into account. The segments of the calibration curves were obtained by approximating only *in vivo* calibration data for the specific S_aO_2 range. Different

calibration curves were selected based on physiological parameters, while specific calibration curve segments were selected based on the $S_{pa}O_2$ range.

Casciani *et al.* (1995) and Mannheimer *et al.* (1997) described pulse oximetry systems where the selection and placement of LEDs are specifically based on improved performance at low saturations. It was postulated that the deteriorating bias and precision of pulse oximeters are as a result of mean photon path length mismatches between the wavelengths used due to tissue perturbations, as described above. Tissue perturbations were described as physiological tissue changes that significantly affect light propagation properties. Perturbations listed included variations in tissue composition, haemoglobin concentration and application force between the sensor and measured tissue Casciani *et al.* (1995). The hypothesis proposed by Mannheimer *et al.* (1997) stated that the mean photon path length differences for a 660/910 nm LED combination are well-matched between calibration and actual use at high saturation. This match deteriorates however, at low saturations. A re-selection of LED wavelengths was recommended based on an improved match between mean photon path length differences for calibration and actual use at low saturation. It was demonstrated by Mannheimer *et al.* (1997), using Monte Carlo and photon diffusion models, that a 735/890 nm LED combination is optimally suited for low saturation scenarios, even though sensor sensitivity to S_aO_2 changes deteriorated.

3.3 Pulse Oximetry in Low Perfusion Scenarios

The use of pulse oximetry to determine $S_{pa}O_2$ accurately and repeatably is dependent on the presence of a clearly detectable AC component in the PPG. This AC component is used to calculate R, as described in Section 3.1. Unfortunately, the AC component is often missing in critically ill patients where accurate $S_{pa}O_2$ values are most important. Patients suffering from sepsis, hypothermia, hypovolemia, peripheral vascular disease, diabetes and various forms of shock often exhibit severe peripheral hypoperfusion (Schallom *et al.*, 2007; Sinex, 1999). Additionally, patients that have Raynaud's phenomenon may also exhibit poor pefusion (Kamat, 2002). Low peripheral perfusion will inevitably result in a small AC component, complicating the procedure of separating PPG AC and DC components in an en-

vironment where signal-to-noise ratios are low. Hypoperfusion states have been known to lead to pulse oximeter error messages of 'Low Signal Quality' or 'Inadequate Signal' (Kamat, 2002; Pologe, 1987). The importance of accurate $S_{pa}O_2$ values in critically ill patients has thus led to numerous studies into the performance of pulse oximeters in low perfusion scenarios (Schallom *et al.*, 2007; Jubran, 2004; Cooke, 2002, 2000; Villanueva *et al.*, 1999; Lutter *et al.*, 2001; Shah and Estanol, 2006; Hummler *et al.*, 2006, 2004).

Schallom *et al.* (2007) conducted a study on pulse oximeter performance in decreased peripheral perfusion scenarios. A study population of 30 critically ill patients at risk of decreased peripheral perfusion was used. Two different pulse oximeters were tested, namely the *Nellcor Oximax* N-595 and the *Philips CMS*. $S_{pa}O_2$ performance was stated as -2.61±3.61% (bias±precision) for the N-595, while the performance of the *CMS* model was given as -3.84±6.91%. The N-595 displayed measurement failures for 7% of the study population, while the *CMS* failed to display a measurement for 10% of the study population. The older *CMS* model thus displayed inferior performance in low perfusion scenarios to that of the newer N-595 system, providing evidence that advances in pulse oximetry technology has led to better performance.

Studies done by Cooke (2000) and Cooke (2002) examined low perfusion performance differences in a total of 19 different pulse oximeters using a *Bio-Tek Index* 2MF S_pO_2 simulator. Simulated low perfusion scenarios were monitored using the different pulse oximeters and the signal sensitivity values recorded where each oximeter ceased to function correctly. Signal sensitivity was defined as AC_{ir}/DC_{ir}. Sensitivity values for individual pulse oximeters spanned a wide range, with the best values being recorded for the *Nellcor* N-395, *Masimo* MS-3, *OSI Medical* 2100 and *Dolphin Medical* DD 3000 pulse oximeters as 0.05%, 0.06%, 0.06% and 0.06%, respectively. The worst sensitivity recorded was that of the *NovaMetrix* 513 model with a value of 0.4%.

Shah and Estanol (2006) and Lutter *et al.* (2001) conducted similar studies on the sensitivity and specificity of various modern pulse oximeter models in detecting hypoxic events. Shah and Estanol (2006) conducted rapid desaturation and resaturation studies with motion artifacts on 10 healthy volunteers, while Lutter *et al.* (2001) studied 108 subjects undergoing general or emergency surgery without motion artifacts. Sensitivity was defined as the system's ability to detect a hypoxic

event, while the ability to generate true alarms based on hypoxic events was termed as specificity. Best sensitivity and specificity values of 95% and 97% were recorded for the *Masimo Radical* model during the Shah and Estanol (2006) study, while the Lutter *et al.* (2001) study recorded very similar values for all three tested pulse oximeters.

Presently, low perfusion pulse oximetry technology is based on the adaptive filtering of the PPG to accurately extract R from the small AC component, as well as the minimization of noise contamination of the PPG. This is in contrast with the historical methods of simply increasing LED output intensity until an AC component could be extracted from the PPG (Tremper and Barker, 1989). As explained by Sinex (1999), this increases unwanted artifact amplification, resulting in noise contamination of the calculated R.

The *Masimo Corporation* was the first company to receive FDA clearance to claim accurate measurement of $S_{pa}O_2$ in decreased peripheral perfusion scenarios (Masimo Corporation, 2006). The accurate low perfusion measurement of $S_{pa}O_2$ was achieved through the design of the sensor hardware to minimize electronic noise contamination of the PPG, as well as an innovative signal processing algorithm that uses adaptive filters to eliminate the effects of noise artifacts (Masimo Corporation, 2006).

The application of adaptive filtering in biomedical signals such as a PPG has a lot of merit. Unfortunately, the adaptive filter needs a reference signal (RS) to calculate the filter coefficients in real-time. This reference signal is generally not available. *Masimo* solved this problem with their Signal Extraction Technology (SET) concept. SET extracts a reference signal from the red and infrared PPGs by manipulating the equation used to calculated R in conventional pulse oximetry. The reference signal is calculated by using the relationship stated as Equation 3.5 (Masimo Corporation, 2005).

$$RS = I_r - [R \times I_{ir}] \tag{3.5}$$

As can be seen from Equation 3.5, RS is dependent on R. *Masimo* now uses a technique it calls Discrete Saturation Transform (DST) to calculate $S_{pa}O_2$ using the reference signal and infrared PPG. A reference signal generator creates a range of reference signals that corresponds with R values correlated with $S_{pa}O_2$ values

ranging from 0-100%. These reference signals are used as input to an adaptive filter or adaptive noise canceller (ANC) to aggresively filter the infrared PPG. The filtered PPG is then analyzed for output power. The SET system can be seen as Figure 3.3.

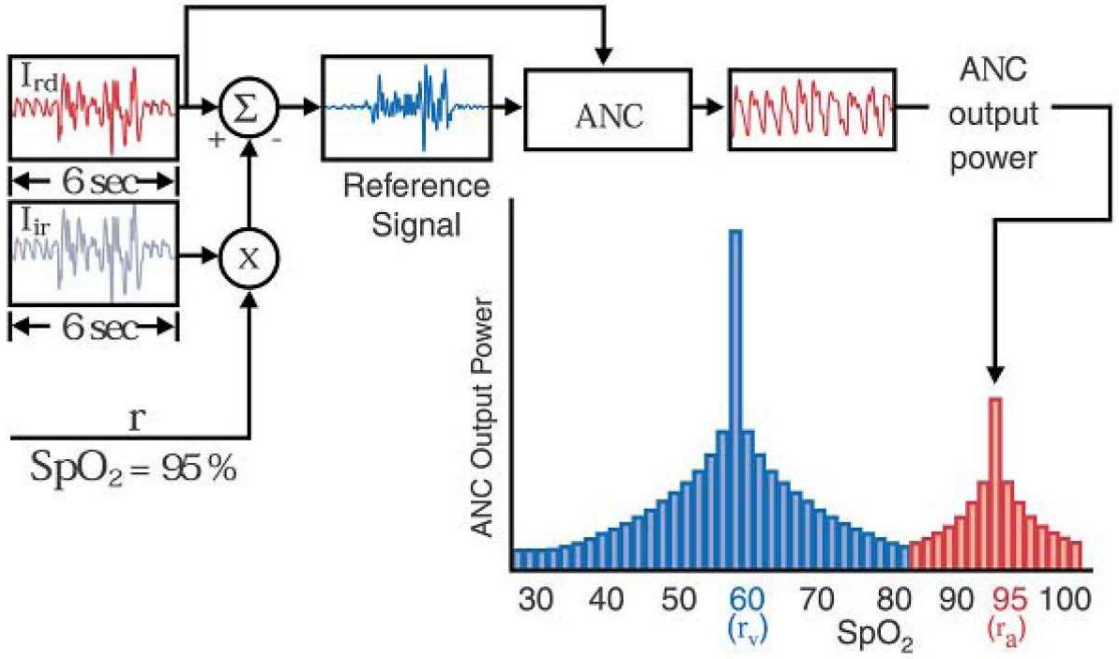

Figure 3.3: Masimo SET (Masimo Corporation, 2005)

As can be seen in Figure 3.3, the analysis of PPG output power can be presented in an output power graph. This graph can be interpreted by looking at the reference signal range. If the R value selected to calculate a reference signal is incorrect, the reference signal would be an inaccurate representation of PPG noise, resulting in significant parts of the true PPG signal being filtered out as well. This would result in a low output power filtered PPG. If the R value, however, is correct, the reference signal would be representative of PPG noise, resulting in only PPG noise being filtered out. The filtered PPG would thus have significant output power. These peaks in output power resulting from R values corresponding to $S_{pa}O_2$ and $S_{pv}O_2$ are identified and converted to $S_{pa}O_2$ and $S_{pv}O_2$ using a conventional calibration curve.

Masimo SET pulse oximetry has been shown to be superior in both sensitivity and specificity to conventional pulse oximeters in a number of low peripheral perfusion studies (Lutter *et al.*, 2001; Graybeal and Petterson, 2004; Shah and Estanol, 2006; Cooke, 2000). The calculation of $S_{pa}O_2$ is, however, still dependent on the detection of an AC component, however small, in the PPG.

In a study done by Foo and Wilson (2006), accelerometer outputs were used as input to an adaptive filter. The accelerometer outputs quantified motion artifact contamination of the PPGs, resulting in a reference signal that was used by the adaptive filter to cancel the corresponding motion artefact noise. Zero-phase digital filtering was also used in poor peripheral perfusion scenarios. The system was however, still dependent on the detection of an AC component in the PPG.

Coetzee and Elghazzawi (2000) proposed an adaptive filtering system that uses a synthetic reference signal derived from heart rate and an idealised pulse waveform shape. A clean segment of the PPG was selected from which the heart rate is calculated. A basic pulse signal waveform was derived from adult volunteer data and an individualized idealized pulse shape calculated for the PPG data. The pulse shape and heart rate data were used to create a synthetic reference signal that was used to adaptively filter the original PPG data to obtain a relatively noise-free PPG. R values were calculated from the noise-free AC component and related to $S_{pa}O_2$ by means of a conventional calibration curve.

It can thus be concluded that the performance of pulse oximeters in low perfusion scenarios varies widely between manufacturers and different manufacturer models. It does seem however, that the sensitivity and specificity of the so-called 'Generation 3' pulse oximeters have improved when compared to previous versions. The measurement of $S_{pa}O_2$ in severe hypoperfusion scenarios is, however, still a major issue, as all present time pulse oximeters need an AC (*ie.* pulsatile) component in the PPG to calculate $S_{pa}O_2$.

3.4 Pulse Oximetry in Determining Venous Saturation

The value of S_vO_2 measurement (mixed and central) in clinical monitoring is a subject that has been discussed for many years. Claims have been made that S_vO_2

is a good indicator of the oxygen supply-demand balance in the body (Kandel and Aberman, 1983), while studies done by Reinhart and Bloos (2005) indicated that an additional treatment of maintaining S_vO_2 levels in patients suffering from sepsis or septic shock increases survival. S_vO_2 may also be useful for assessing patients with peripheral vascular disease (Yoxall and Weindling, 1997). Three invasive types of S_vO_2 measurement are used today, namely the use of an pulmonary artery catheter (Kandel and Aberman, 1983), a central venous catheter (Reinhart *et al.*, 1989) or a venous blood gas sample, all with associated risks and disadvantages (Sise *et al.*, 1981). The main disadvantages of using a venous blood gas sample are its intermittence and invasiveness. A need thus exists for a continuous and non-invasive method of measuring S_vO_2.

Yoxall and Weindling (1997) and Yoxall and Weindling (1996) studied the non-invasive measurement of $S_{pv}O_2$ in adults and neonates by using a venous occlusion method. This method can not be classified as a pure pulse oximetry method, as pulse waveforms were not used to calculate $S_{pv}O_2$. A pressure cuff was inflated around the subject's forearm at a pressure of $30 - 40\,\text{mmHg}$ to induce occlusion of venous drainage for a short period of time. This occlusion of venous drainage caused a rise in HbO_2 and Hb concentrations as a result of increased venous volume. $S_{pv}O_2$ was calculated, using the modified Beer-Lambert's Law (Elwell and Hebden, 1999), to calculate HbO_2 concentration relative to total haemoglobin concentration. Yoxall and Weindling (1996) reported a $S_{pv}O_2$ bias and precision of $4.3\pm2.6\%$ for neonates. Yoxall and Weindling (1997) reported a $S_{pv}O_2$ bias and precision of $4.7\pm4.05\%$ for adults. The merits of venous occlusion methods are debatable, but its intermittance still remains a drawback (Echiadis *et al.*, 2007).

Chan *et al.* (2003) and Echiadis *et al.* (2007) conducted studies into a new pulse oximetry system capable of continuously monitoring $S_{pv}O_2$. The system, as described by Chan and Smith (2003), relies on pneumatically induced venous pulsations to calculate $S_{pv}O_2$ using conventional pulse oximetry methods. Pneumatic pressure and an artificial pulsation frequency was chosen to minimize interference with normal arterial pulsations. Chan *et al.* (2003) conducted a study into the performance of the new system on recovering cardiac surgery patients, while Echiadis *et al.* (2007) studied the system's performance on 23 subjects undergoing cardiac surgery. Both studies were inconclusive, but adequate correlation with reference systems was displayed to warrant further investigation.

In a study done by Aoyagi (2003), a five wavelength pulse oximetry system, capable of measuring $S_{pv}O_2$ was mentioned. This system relies on a combination of conventional pulse oximeter theory and scattering theory as presented by Schuster (1905). $S_{pv}O_2$ is to be calculated by means of artificially induced venous tremors or pulsations. This is, however, still a conceptual system and no studies into the system's performance could be found.

It can thus be concluded that the determination of $S_{pv}O_2$ has its merits and that a successful pulse oximeter prototype capable of measuring $S_{pv}O_2$ would be a valuable addition to modern ICU equipment. A number of prototypes have been presented, although no conclusive evidence of accurate and repeatable performance have been found.

Chapter 4

System Development

The artificial pulse oximeter (APO) system operates upon the principle of generating an artificial pulse in the tissue under consideration and using an adapted pulse oximetry system to measure both arterial and venous blood oxygen saturation from these pulses.

A list of system specifications was initially compiled to clarify the objectives of the study. These were:

1. The final commercial device should be a bed-side monitoring device.
2. The system should be able to non-invasively measure $S_{pa}O_2$ in adults, children, infants and neonates.
3. Accurate and repeatable measurement of $S_{pa}O_2$ in low saturation scenarios is desirable.
4. The system should be able to monitor $S_{pa}O_2$ in patients suffering from severe peripheral hypoperfusion.
5. The system must be adaptable to different parts of the body.

After a prototype was designed to meet the above mentioned objectives and initial tests conducted to analyzed the prototype's performance, two additional objectives were identified. These were:

1. To incorporate into the system design the capability to accurately and repeatably measure $S_{va}O_2$.

2. To evaluate the system's performance in monitoring $S_{va}O_2$.

The development of the APO system can be broadly divided into five different stages, namely a numerical simulation of expected system behaviour, hardware development, signal processing, *in vitro* calibration and *in vivo* validation.

4.1 Artificial Pulse Oximetry (APO)

As mentioned in Section 3.1, conventional pulse oximetry is entirely dependent on the detection of an AC-component in the photoplethysmograph. In the absence of an AC-component, or with the AC-component being very small in comparison with the DC-component, the red to infrared ratio R tends to become unity, regardless of the arterial blood oxygen saturation, S_aO_2. In commercial pulse oximeters, a false, but constant, S_aO_2 value of approximately 85% would be indicated, resulting in a lack of reliable information, which is often required for critically ill patients. Taking these factors into account, commercial pulse oximeters cannot reliably be used in severe hypoperfusion scenarios.

An alternative to conventional pulse oximetry was developed in this study. This alternative, called artificial pulse oximetry, attempted to bypass the above mentioned issues in low perfusion scenarios. This method is based upon the generation of a clearly detectable artificial pulse in the tissue under consideration. In normal tissue, and even tissue suffering from low perfusion, a residential or non-pulsatile blood volume is present in the circulatory system. With conventional pulse oximetry, the SO_2 of this non-pulsatile or DC blood component cannot be measured, but if pulsatile behaviour can be externally induced, normal pulse oximetry principles can be applied to measure SO_2.

The APO system is based upon a peristaltic induced artificial pulse in the tissue under consideration. In our case this tissue would be an extended finger. This peristaltic action is induced by a system of three inflatable tubes, much resembling a conventional sphygmomanometer or blood pressure cuff, around the finger. This principle can be seen as Figure 4.1.

In Figure 4.1, the inflatable tubes encircles the finger and are inflated in a specified sequence. In sequence one, the proximal tube is inflated, pushing residential blood in the circulatory system toward the finger tip. The tube situated in the

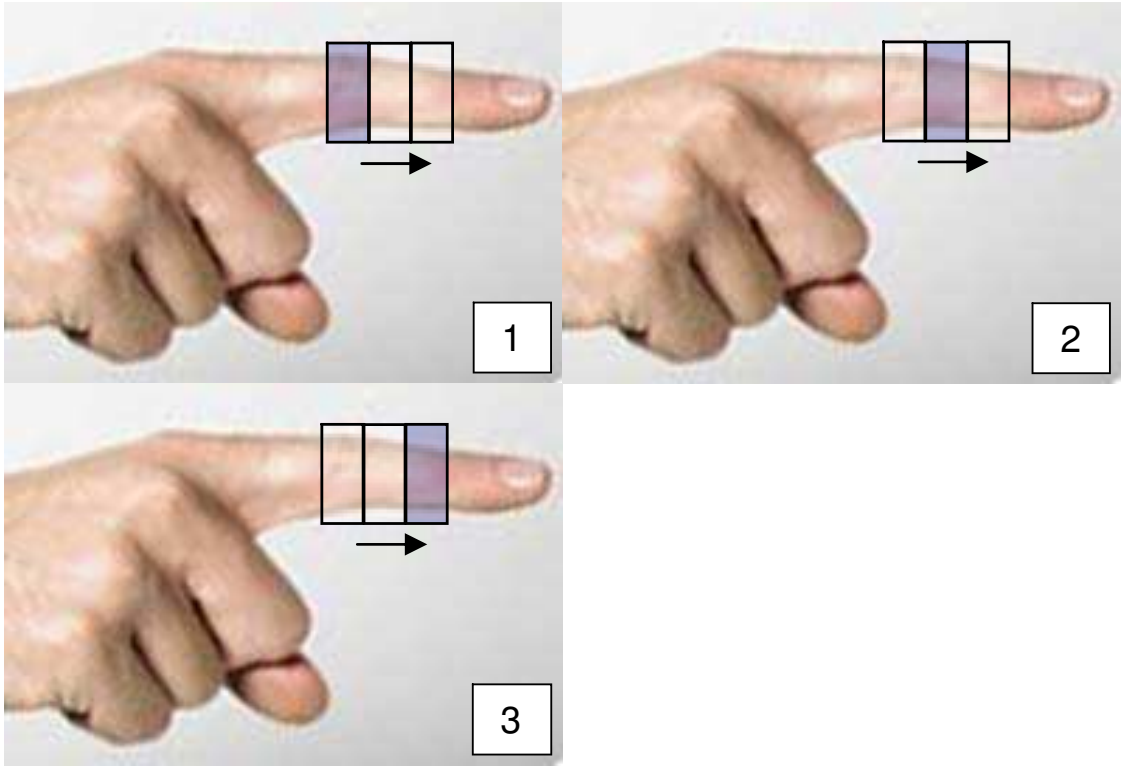

Figure 4.1: Peristaltic Action

middle of the the cuff is inflated in sequence two, while the proximal tube is kept in an inflated state. This forces the residential blood in the direction of the finger tip. Pulse propagation is represented by the arrows in Figure 4.1 After this, the distal tube is inflated in sequence three. Sequence three operates in the same principle as sequence two, with both proximal tube kept in an inflated state, and serves to further enhance the pulse amplitude. The timing of sequences one to three can be modified in order to obtain a sharp, artificially induced, peak. As mentioned earlier, having established clearly detectable pulsatile behaviour in the finger, conventional pulse oximetry principles could now be applied to measure the SO_2 of the residual blood.

The blood oxygen saturation, SO_2, of residential blood varies according to its location in the circulatory system, e.g. arterial or venous circulation. In normal transmittance pulse oximetry systems, the saturation difference between arterial and venous blood is not important, as only arterial blood is seen as having pulsatile behaviour. Jorgensen *et al.* (1995) reported on the independence of transmittance

pulse oximetry to venous pulsatile behaviour in situations where the sensors is properly positioned and attached. Any venous pulsatile behaviour is thus seen as minimal and ignored. However, in the case of the APO, pulsatile behaviour is induced in both arterial and venous circulation. The influence of venous blood cannot be ignored in this case, as the transmittance of light is influenced by both the arterial and venous pulses. If a normal transmittance pulse oximetry approach was followed, the measured S_aO_2 would be too low as a result of the influence of the much lower venous saturation, S_vO_2. A dual approach was thus followed to take S_vO_2 into account as well.

Using the APO system, coordinated pulses are induced in both the arterial and venous circulation. By processing the photoplethysmograph, a ratio R corresponding to a mixed arterial and venous saturation can be calculated. This mixed arterial and venous saturation, S_mO_2, is a linear combination of S_aO_2 and S_vO_2, according to the following:

$$S_mO_2 = P_aS_aO_2 + (1 - P_a)S_vO_2 \tag{4.1}$$

with P_a the arterial pulse volume fraction relating the pulse amplitudes in the arterial and venous circulation. This pulse volume fraction is mainly dependent on the volume of residual blood present in the arterial and venous circulation and the compliance of the arteriole and venule walls. This relationship will be referred to as the arterio-venous hypothesis in future and will be discussed in more detail in Section 4.2.2.C.

Assuming that P_a is a known variable, Equation 4.1 requires that either S_aO_2 or S_vO_2 be known in order to calculate the unknown saturation. To calculate S_vO_2, S_aO_2 would have to be known as a prerequisite. This value for S_aO_2 is obtained by using a conventional pulse oximetry sensor on an unaffected or healthy site such as a finger on the opposite hand or the forehead. In order to minimize the discrepancies between S_aO_2 on the affected and unaffected measurement sites, the unaffected site was chosen to be either as close as possible to the affected site or to be on a symmetrically similar body part such as the left hand if the right hand was affected. In using this approach, it is assumed that S_aO_2 will be similar in the affected and unaffected sites, even in situations of low perfusion, as oxygen diffusion mainly occurs at capillary level. In no perfusion states, it is possible

that this assumption would not be accurate, as S_aO_2 would drop in the arterial circulation during extended periods of tissue occlusion. This assumption would however be valid in scenarios where it is known that a certain degree of perfusion exists, such as in the case of medicinal leech treatment of ischaemia.

Using the APO system, it would thus be possible to measure S_mO_2, and derive S_aO_2 and S_vO_2 from this measurement using Equation 4.1. Knowing these tissue parameters, the physician might be able to make a more informed decision on the status of the affected tissue, with a normal S_aO_2 and spuriously high S_vO_2 being indicative of extended tissue damage.

4.2 System Simulation

A system simulation was conducted to verify whether the APO system would theoretically behave as expected, while also providing information on scenarios that could not be approximated in an *in vitro* or *in vivo* experiment. The simulation would also provide information on scenarios where experimental results were not as expected. Various simulations of conventional pulse oximeter systems have been conducted, but as far as the author could determine, none have made provision for the venous pulsations inherent to the APO system's operation.

4.2.1 Simulation Techniques

Earlier qualitative simulations were based on Beer-Lambert's Law, which describes tissue-photon interaction in a purely absorptive medium, while neglecting scattering. These simulations were soon upgraded to include scattering by introducing a factor, called the differential pathway factor (DPF), to provide for the increase in photon travel path, and an additive factor to provide for scattering losses as well (Elwell and Hebden, 1999). These simulations however, show significant deviation from calibration curves used for commercial pulse oximeters (Schmitt, 1991).

Photon diffusion theory has also been successfully used to model the propagation of light through biological mediums (Steinke and Shepherd, 1988; Schmitt *et al.*, 1990; Schmitt, 1991). Biological mediums are generally characterized by a high optical depth and short mean free path, making it well-suited to diffusion the-

ory modeling. Good correlation with commercial pulse oximeter curves have been shown by (Schmitt, 1991).

More recently, Monte Carlo simulations have been utilized to model the random behaviour of tissue-photon interactions due to the inherently random nature of multiple scattering events. The Monte Carlo method tracks the path of singular photons through the optical medium and calculates the probability of the photon emerging at a point and direction of interest. As singular photons are tracked and large numbers of photon enter the optical medium, considerable computation time is needed (Hiraoka *et al.*, 1993).

It was decided to model the light propagating properties of the finger tissue using photon diffusion theory, based on the reported correlation with existing pulse oximeter calibration curves, as well as the relative ease with which the governing equations could be adapted to provide for venous pulsations.

4.2.2 Photon Diffusion Theory

Photon diffusion theory approximates photon propagation through a medium as a diffusive process. As mentioned earlier, tissue is well suited to diffusive modelling as a result of a high optical depth and short mean free path. A short mean free path is an important prerequisite for diffusion modelling as predominantly scattering behaviour is assumed over absorption. In addition to this, it is assumed that scattering from a unit volume of tissue is isotropic. Although scattering in biological mediums is generally highly anisotropic, isotropic scattering can be assumed if the optical constants are adapted to account for highly forward scattering behaviour and if boundary conditions for the diffusion solution is appropriately chosen (Schmitt *et al.*, 1990).

4.2.2.A Conventional Photon Diffusion Model

The governing equation which describes photon propagation as a diffusive process,

$$\frac{1}{\rho^2}\frac{d}{d\rho}\left(\rho^2\frac{d\psi(\rho)}{d\rho}\right) - \alpha^2\psi(\rho) = -\frac{1}{D}S(\rho) \tag{4.2}$$

was derived by Schmitt (1991) using an angle-independent solution of the general transport equation. In Equation 4.2, ρ [mm] is the physical distance from the

photon source, $\psi(\rho)$ and $S(\rho)$ are the scalar photon density and source function, respectively, at point ρ, α [mm$^{-0.5}$] is the attenuation coefficient and D [mm] is the diffusion coefficient. α and D can be described in terms of the bulk absorption coefficient Σ_{ab} [mm^{-1}] and the transport corrected bulk scattering coefficient Σ'_s [mm^{-1}] as follows (Schmitt, 1991):

$$\alpha = \sqrt{3\Sigma_{ab}(\Sigma'_s + \Sigma_{ab})} \tag{4.3}$$

$$D = \frac{1}{3(\Sigma'_s + \Sigma_{ab})} \tag{4.4}$$

The bulk absorption and scattering coefficients will be discussed in the following section.

From the subsequent solution of Equation 4.2 by Schmitt (1991), blood oxygen saturation S_aO_2 was related to the red/infrared ratio R through the following:

$$S_aO_2 = \frac{R\sigma^{0\%}_{ab,ir} - K'_t\sigma^{0\%}_{ab,r}}{K'_t(\sigma^{100\%}_{ab,r} - \sigma^{0\%}_{ab,r}) + R(\sigma^{0\%}_{ab,ir} - \sigma^{100\%}_{ab,ir})} \tag{4.5}$$

with

$$K'_t = \frac{\Sigma'_{s,r}\left(\frac{\alpha_r d-1}{\alpha_r^2 d}\right)}{\Sigma'_{s,ir}\left(\frac{\alpha_{ir} d-1}{\alpha_{ir}^2 d}\right)} \tag{4.6}$$

where $\sigma^{0\%}_{ab,r}$ [um^2] and $\sigma^{100\%}_{ab,r}$ [um^2] are the optical absorbtion cross-sections for red blood cells (RBCs) containing totally deoxygenated and oxygenated haemoglobin, respectively. A subscript r or ir indicates an optical property at the lower red wavelength (r) or higher infrared wavelength (ir). Optical absorption cross-sections will be discussed in Section 4.2.2.B. In Equation 4.6, d [mm] is the finger diameter.

Results for this approach will be discussed in Section 5.1.

4.2.2.B Bulk Absorption and Scattering Coefficients

As can be noted from Equations 4.3 to 4.6, diffusive photon propagation properties in biological mediums can be entirely described in terms of the bulk absorption coefficient Σ_{ab} [mm^{-1}] and the transport corrected scattering coefficient Σ'_s [mm^{-1}] of the tissue. The transport corrected scattering coefficient is derived from the

isotropic scattering coefficient to account for the highly forward scattering characteristics of tissue.

The bulk absorption coefficient Σ_{ab} [mm^{-1}] in Equation 4.3 can be seen as a cumulative function of the absorption coefficients of oxygenated and deoxygenated blood, Σ_{ab}^{art} [mm^{-1}] and Σ_{ab}^{ven} [mm^{-1}] respectively, as well as that of blood perfused tissue Σ_{ab}^{tis} [mm^{-1}]. This function can be formulated as follows (Schmitt, 1991):

$$\Sigma_{ab} = V_a\Sigma_{ab}^{art} + V_v\Sigma_{ab}^{ven} + [1 - (V_a + V_v)]\,\Sigma_{ab}^{tis} \tag{4.7}$$

with V_a and V_v the respective volume fractions of resident oxygenated and deoxygenated blood in the tissue.

The absorption coefficient for whole blood in Equation 4.7 is a function of hematocrit H, RBC volume υ_i [cm^3], fractional arterial or venous blood oxygen saturation S_aO_2 or S_vO_2 and the optical absorption cross sections for an single RBC, $\sigma_{ab}^{0\%}$ [um^2] and $\sigma_{ab}^{100\%}$ [um^2]. These relationships were stated by Schmitt (1991) as:

$$\Sigma_{ab}^{art} = \frac{H}{\upsilon_i}\left[S_aO_2\sigma_{ab}^{100\%} + (1 - S_aO_2)\sigma_{ab}^{0\%}\right] \tag{4.8}$$

$$\Sigma_{ab}^{ven} = \frac{H}{\upsilon_i}\left[S_vO_2\sigma_{ab}^{100\%} + (1 - S_vO_2)\sigma_{ab}^{0\%}\right] \tag{4.9}$$

The $\frac{H}{\upsilon_i}$ factor at the beginning of Equations 4.8 and 4.9 scales the optical cross sections to the macroscopic coefficients for whole blood. Alternative scaling factors have been proposed, but according to Faber *et al.* (2004) good correlation with experimental data were obtained through the use of the $\frac{H}{\upsilon_i}$ scaling factor.

The optical cross sections for a particle, as used in Equations 4.8 and 4.9, can be defined as the total absorbed or scattered power, divided by the incident power flux density (Steinke and Shepherd, 1988). The absorption cross section for an RBC was approximated by a Mie theory approximation which provides exact solutions to Maxwell's equations. Mie algorithms provided by Michel (2007) were used to calculate σ_{ab} for a singular RBC. By geometrically approximating the irregular shape of an RBC with the homogeneous spherical particle Mie model, this inherently remains an approximation, but good correlation between calculated and experimental values for σ_{ab} were reported by Reynolds *et al.* (1974, 1976) and Pierce (1972) for a spherical particle with a volume equal to that of an RBC.

As inputs to the algorithms provided by Michel (2007), the complex index of refraction $\mathbf{n}(\lambda) = n(\lambda) + i\kappa(\lambda)$ for a singular RBC and the index of refraction for blood plasma were needed. The index of refraction for blood plasma used in the Mie calculations was taken as 1,35 (Gonchukov *et al.*, 2000; Lu *et al.*, 2005). The complex index of refraction for an RBC is directly proportional to the absorption coefficients of haemoglobin at a specific wavelength of light. The complex part of $\mathbf{n}(\lambda)$, $i\kappa(\lambda)$ relates to the molar extinction coefficient of HbO_2 or Hb through the following relationship (Hammer *et al.*, 1998):

$$\kappa(\lambda) = \frac{ln10}{4\pi} x\lambda\,[me(\lambda)] \tag{4.10}$$

with with x the concentration of haemoglobin (335 g/L), $me(\lambda)$ [$\mathrm{cm^{-1}M^{-1}}$] the molar extinction coefficient of HbO_2 or Hb at the vacuum wavelength λ [cm]. Molar extinction coefficient values were obtained from Prahl (1998). The real part of $\mathbf{n}(\lambda)$, $n(\lambda)$ was derived by Friebel and Meinke (2006) using Fresnel reflectance measurements on haemoglobin solutions obtained by haemolysing human RBCs. The following relationship was used:

$$n(\lambda) = n_{water}(\lambda)\,[\beta(\lambda)x + 1] \tag{4.11}$$

with $n_{water}(\lambda)$ the wavelength dependent refractive index of water and $\beta(\lambda)$ the wavelength dependent refractive increment as provided by Friebel and Meinke (2006). This relationship does not take effect of haemoglobin saturation into account. Values for $n(\lambda)$ obtained by Faber *et al.* (2004) take this effect into account, but unfortunately the values stated are for haemoglobin concentrations other than those used in the context of this study. These values, however, do show an approximately constant difference between oxygenated and deoxygenated haemoglobin solutions. This difference was used to modify $n(\lambda)$ according to haemoglobin oxygenation. The complex indices of refraction and absorption cross-sections of an RBC containing HbO_2 and Hb at the wavelengths of interest are shown in Table 4.1. These values are in good agreement with those provided by Meinke *et al.* (2007) and Schmitt *et al.* (1986).

Values for the absorption coefficient of bloodless tissue Σ_{ab}^{tis} [$\mathrm{mm^{-1}}$] in Equation 4.7 were found using the approximations as stated by Jacques (1998). The total absorption coefficient for bloodless tissue can be seen as a cumulative function

Table 4.1: Complex Indices of Refraction and Absorption Cross-Sections

(λ)	HbO_2		Hb	
	Index of Refraction	Absorption Cross-section	Index of Refraction	Absorption Cross-section
660	$1.4179 + i1.948e^{-5}$	0.03668	$1.4129 + i1.967e^{-4}$	0.36528
740	$1.4159 + i3.048e^{-5}$	0.05102	$1.4109 + i7.626e^{-5}$	0.12656
880	$1.4148 + i9.378e^{-5}$	0.13149	$1.4098 + i5.904e^{-5}$	0.08231
910	$1.4154 + i1.02e^{-4}$	0.13837	$1.4104 + i6.509e^{-5}$	0.08780
940	$1.4155 + i1.054e^{-4}$	0.13843	$1.4105 + i6.012e^{-5}$	0.07852

of the absorption coefficients of the epidermis Σ_{ab}^{epi}, dermis Σ_{ab}^{der} and subcutaneous tissue or subdermis Σ_{ab}^{sder}. In all tissue layers, the absorption coefficient is a function of the wavelength of light used. The total absorption coefficient for bloodless tissue Σ_{ab}^{tis} [mm^{-1}] was thus approximated as follows:

$$\Sigma_{ab}^{tis} = c_{epi}\Sigma_{ab}^{epi} + c_{der}\Sigma_{ab}^{der} + (1 - c_{epi} - c_{der})\Sigma_{a}^{sder} \qquad [cm^{-1}] \qquad (4.12)$$

with c_{epi} and c_{der} the cross-sectional fraction of the finger diameter occupied by the epidermis and dermis, respectively.

The effect of the epidermal absorption coefficient Σ_{ab}^{epi} [mm^{-1}] in Equation 4.12 can be seen as a combination between baseline skin absorption and absorption due to melanin. Melanin is a polymer found in melanosomes, particles found in varying concentrations in the epidermis. Differing melanosome concentrations are the main reason behind differences in skin colour. Melanosome fractions can be seen below as Table 4.2 for different skin colours (Jacques, 1998).

Table 4.2: Melanosome Fraction

Skin Colour	Melanosome Fraction
Light	0.013-0.063
Moderate	0.11-0.16
Dark	0.18-0.43

The overall epidermal absorption coefficient Σ_{ab}^{epi} [cm^{-1}], as used in Equation 4.12, can be found as defined by Jacques (1998):

$$\Sigma_{ab}^{epi} = F\Sigma_{ab}^{mel} + (1 - F)\Sigma_{ab}^{eb} \qquad (4.13)$$

with F the melanosome volume fraction as found in Table 4.2, Σ_{ab}^{eb} the baseline epidermal absorption coefficient and Σ_{ab}^{mel} the absorption coefficient due to melanin absorption.

The baseline epidermal absorption coefficient Σ_{ab}^{eb} [cm^{-1}] in Equation 4.13 is defined by Jacques (1998) as follows:

$$\Sigma_{ab}^{eb} = 0.244 + 85.3e^{\frac{-(\lambda-154)}{66.2}} \tag{4.14}$$

with λ the wavelength [nm] used. This approximation was empirically derived using bloodless rat skin due the similarities to neonatal skin.

The melanin induced absorption coefficient Σ_{ab}^{mel} [cm^{-1}] from a single melanosome, as used in Equation 4.13 is obtained from Jacques (1998).

$$\Sigma_{ab}^{mel} = 6.6e^{-11}\lambda^{-3.33} \tag{4.15}$$

As this only provides a coefficient for a single melanosome, a multiplying factor had to be included in the calculation of overall Σ_{ab}^{epi} [mm^{-1}] to account for the amount of melanosomes per unit volume of epidermis. It has to be noted that the melanin content of melanosomes differs in varying degrees between individuals, causing this expression to be viewed as a general approximation at best.

The dermal and subdermal absorptive coefficients, Σ_{ab}^{der} [mm^{-1}] and Σ_{ab}^{sder} [mm^{-1}], as used in Equation 4.12, was approximated by Simpson *et al.* (1998) using an inverse Monte Carlo simulation on diffuse reflectance and transmittance single integrating sphere measurements on *ex vivo* human skin.

The transport-corrected scattering coefficient Σ_s' [mm^{-1}] for blood-perfused tissue can be expressed as a cumulative function of the coefficients of the major scattering components. Σ_s', as used in Equation 4.3 was expressed by Schmitt (1991) as follows:

$$\Sigma_s' = (V_a + V_v)\Sigma_s'^{b} + [1 - (V_a + V_v)]\,\Sigma_s'^{tis} \tag{4.16}$$

with $\Sigma_s'^{b}$ [mm^{-1}] and $\Sigma_s'^{tis}$ [mm^{-1}] the transport corrected scattering coefficient for blood and tissue, respectively. $\Sigma_s'^{tis}$ is the representative coefficient of Mie and Raleigh scattering caused by epidermal, dermal and subdermal tissue components. Raleigh scattering is scattering caused by particles much smaller than the wavelength of incident light, such as cellular structures, while Mie scattering is

scattering caused by particles with diameters the same order of magnitude as the incident wavelength, such as large collagen fibers (Jacques, 1998)

Various approaches exist for calculating $\Sigma_s'^b$ as used in Equation 4.16. Steinke and Shepherd (1988) calculated $\Sigma_s'^b$ by using a spherical particle Mie scattering approach to calculate the scattering cross-section σ_s of a singular RBC, as well as the anisotropy factor g. The anisotropy factor g can be defined as the mean cosine of the scattering angle. This factor is an indication of the scattering behaviour of the medium, with g $\approx$ 1 indicating highly forward scattering behaviour and g $<<$ 1 indicating highly back scattering behaviour. $\Sigma_s'^b$ was obtained by adapting σ_s with a (1-g) factor to account for the highly forward scattering nature of blood and a factor dependent on hematocrit H and RBC volume υ_i. Good correlation with experimental values has been found for σ_s (Reynolds *et al.*, 1974, 1976), but experiments have shown that Mie theory significantly overestimates the true g value. This significance is due to the fact that even small variations in the value of g result in large variation in the (1-g) factor as the (1-g) factor is small. The discrepancy between experimental and Mie values for g is a result of the lesser forward peaked scattering function, inherent to randomly orientated, non-spherical particles such as RBCs, than that of the volume equivalent spherical particles used for the Mie approximation (Lovell *et al.*, 1999). It was thus decided to rather use the approach followed by Meinke *et al.* (2007) who determined empirical functions to model the hematocrit and suspending medium dependence of $\Sigma_s'^b$ directly. In this approach, $\Sigma_s'^b$ for RBCs in blood plasma is related to the transport corrected scattering coefficient for RBCs suspended in a saline solution. This coefficient $\Sigma_s'^{sa}$ [mm^{-1}] can be expressed as follows:

$$\Sigma_s'^{sa} = 0.1167\Sigma'_{sST}(\lambda)H \tag{4.17}$$

with $\Sigma'_{sST}(\lambda)$ [mm^{-1}] the wavelength dependent scattering coefficient for a standardized saline RBC suspension as provided by Meinke *et al.* (2007). This value for $\Sigma_s'^{sa}$ was adapted to $\Sigma_s'^b$ by reducing the original value by the recommended 35% in the $600 - 1100$ nm wavelength range, as noted by Meinke *et al.* (2007) for blood plasma RBC suspensions.

As noted earlier, $\Sigma_s'^{tis}$ in Equation 4.16 is a function of scattering coefficients as a result of Mie and Raleigh scattering. Due to the thinness of the epidermis and

similarity between scattering coefficients for the epidermis and dermis, $\Sigma_s^{'tis}$ can be seen as a combination of the transport corrected scattering coefficients of just the dermis and subdermis, $\Sigma_s^{'der}$ [mm^{-1}] and $\Sigma_s^{'sder}$ [mm^{-1}]. Values for $\Sigma_s^{'der}$ and $\Sigma_s^{'sder}$ were obtained from Simpson *et al.* (1998). An expression for $\Sigma_s^{'tis}$ [mm^{-1}] can be found below.

$$\Sigma_s^{'tis} = C_{der}\Sigma_s^{'der} + (1 - C_{der})\Sigma_s^{'sder} \qquad [cm^{-1}] \tag{4.18}$$

In Equation 4.18, c_{der} is the same finger diameter fraction as used in Equation 4.12.

The bulk absorption and scattering properties of whole blood, bloodless tissue and blood perfused tissue for all wavelengths of interest can be seen below as Table 4.3.

Table 4.3: Absorption and Scattering Properties

Wavelength		660 nm	740 nm	880 nm	910 nm	940 nm
Property [mm^{-1}]	Equation					
Σ_{ab}^{art} @ 100% S_aO_2	4.8	0.183	0.256	0.657	0.692	0.692
Σ_{ab}^{art} @ 50% S_aO_2	4.8	1.005	0.444	0.535	0.565	0.542
Σ_{ab}^{art} @ 0% S_aO_2	4.8	1.826	0.633	0.412	0.439	0.393
$\Sigma_s^{'b}$	4.17	1.536	1.441	1.410	1.393	1.444
Σ_{ab}^{tis}	4.12	0.015	0.012	0.011	0.015	0.018
$\Sigma_s^{'tis}$	4.18	1.617	1.447	1.259	1.239	1.227
Σ_{ab} @ 100% S_aO_2	4.7	0.049	0.040	0.073	0.080	0.082
Σ_{ab} @ 50% S_aO_2	4.7	0.132	0.059	0.061	0.067	0.067
Σ_{ab} @ 0% S_aO_2	4.7	0.197	0.074	0.051	0.057	0.073
Σ_s'	4.16	1.609	1.447	1.274	1.254	1.249

Constants used: H=0.45, V_a=V_v=0.05, υ_i=90 um^3, D=8,4 mm, Epidermal Thickness=60 um, Dermal Thickness=1,2 mm, Arteriovenous Saturation Δ=10%

4.2.2.C Photon Diffusion Theory for Arterial and Venous Pulsations

As mentioned earlier, all previous photon diffusion theory simulations found by the author, only took the arterial pulsatile component into consideration when simulating the relationship between R and arterial blood oxygen saturation S_aO_2.

This is normally a valid approach as the small diameter capillaries in the capillary bed reduces the arterial systolic pulses to an acceptably low value in the venous circulation. Even if there is a venous pulsatile component, the influence on the peak-to-trough values, as obtained from the PPG, should be negligibly small.

Using this approach, Schmitt (1991) derived the relationship between R and S_aO_2 by assuming that the AC component in the PPG is caused by the influx of arterial blood during systole, resulting in an increase in the bulk absorption coefficient of the blood perfused tissue. This increase in Σ_{ab} was expressed as follows:

$$\Sigma_{ab} + \Delta\Sigma_{ab} = (V_a + \Delta V_a)\Sigma_{ab}^{art} + V_v\Sigma_{ab}^{ven} + [1 - (V_a + \Delta V_a + V_v)]\,\Sigma_{ab}^{tis} \tag{4.19}$$

with ΔV_a the influx of arterial blood during systole. The AC component caused by the increase in the bulk scattering coefficient of the blood perfused tissue was neglected due to the similarity between $\Sigma_s^{'b}$ at the red and infrared wavelength. This scattering AC component only results in a DC offset of the absorption AC component in the PPG. By assuming that $\Sigma_{ab}^{art} >> \Sigma_{ab}^{tis}$, as can be noted from Table 4.3, Schmitt (1991) concluded the following:

$$\Delta\Sigma_{ab} = \Delta V_{ab}\Sigma_a^{art} \tag{4.20}$$

Using Equation 4.20, Schmitt (1991) derived Equation 4.5.

In the case of the APO, the assumption of a non-important venous pulsatile component can not be validated. As blood is pushed into the measurement zone via peristalsis, both arterial and venous absorption contributes toward the AC component in the PPG. If the venous pulsatile component is ignored in this scenario, the ratio, and thus arterial saturation, calculated would indicate a lower value that is in fact the case. This is as a result of the much lower saturation in the venous circulation. The S_aO_2 would thus be a mixture of arterial and venous saturation, resulting from the averaged value being calculated.

This effect was taken into account by modifying Equation 4.19 to include the effect of venous pulsatile blood. By including a ΔV_v factor to account for the influx of venous blood into the measurement zone, Equation 4.19 becomes,

$$\begin{aligned}\Sigma_{ab} + \Delta\Sigma_{ab} &= (V_a + \Delta V_a)\Sigma_{ab}^{art} + (V_v + \Delta V_v)\Sigma_{ab}^{ven} \\ &\quad + [1 - (V_a + \Delta V_a + V_v + \Delta V_v)]\,\Sigma_{ab}^{tis} \end{aligned} \tag{4.21}$$

so that,

$$\Delta\Sigma_{ab} = \Delta V_a(\Sigma_{ab}^{art} - \Sigma_{ab}^{tis}) + \Delta V_v(\Sigma_{ab}^{ven} - \Sigma_{ab}^{tis}) \tag{4.22}$$

If it is assumed that Σ_{ab}^{art} and $\Sigma_{ab}^{ven} >> \Sigma_{ab}^{tis}$, it can be concluded that

$$\Delta\Sigma_{ab} \approx \Delta V_a\Sigma_{ab}^{art} + \Delta V_v\Sigma_{ab}^{ven} \tag{4.23}$$

Using the same approach as Schmitt (1991) to obtain Equation 4.5, ratio R can now be expressed as

$$R = K_t' \frac{\Sigma_{ab,r}^{art}\Delta V_a + \Sigma_{ab,r}^{ven}\Delta V_v}{\Sigma_{ab,ir}^{art}\Delta V_a + \Sigma_{ab,ir}^{ven}\Delta V_v} \tag{4.24}$$

with K_t' calculated using Equation 4.6.

The relationship between ΔV_a and ΔV_v was needed to obtain a solution to Equation 4.24. This relationship was obtained by comparing arterial and venous compliance, with compliance being the change in volume for a given change in pressure. If it is assumed that the APG generates an equal pressure wave in both the arterial and venous circulation, compliance would determine the magnitude of ΔV_a and ΔV_v. *In vivo* compliance is not a static property, but is in fact a very dynamic property due to the autonomic reflexes responsible for blood pressure regulation (Jagomagi *et al.*, 2005; Martini and Bartholomew, 2003). Due to this and the wide variation in compliance values recorded in literature for arterial and venous compliance (Jagomagi *et al.*, 2005; Kawarada *et al.*, 1988; Krenz and Dawson, 2003), universal arterial and venous compliance values could not be established. It was thus decided to model the arterial-to-venous compliance ratio as 1:1 as a first approximation. This ratio could easily be revised if the results indicated that compliance had a major effect on R values. Using this compliance ratio, R could be expressed in terms of S_aO_2 and S_vO_2 as follows:

$$R = K_t' \frac{S_aO_2(\sigma_{ab,r}^{100\%} - \sigma_{ab,r}^{0\%}) + S_vO_2(\sigma_{ab,r}^{100\%} - \sigma_{ab,r}^{0\%}) + 2\sigma_{ab,r}^{0\%}}{S_aO_2(\sigma_{ab,ir}^{100\%} - \sigma_{ab,ir}^{0\%}) + S_vO_2(\sigma_{ab,ir}^{100\%} - \sigma_{ab,ir}^{0\%}) + 2\sigma_{ab,ir}^{0\%}} \tag{4.25}$$

By stating S_aO_2 as a constant and specifying S_vO_2 as values ranging from 0% to 100%, R could thus be calculated. Results for this approach will be discussed in Section 5.1.

4.3 Hardware Development

The hardware development phase consisted of the design and integration of several subsystems. These systems were: the optical components, the A/D converter and optical driver and the artificial pulse generator (APG). An integrated representation of these systems can be seen as Figure 4.2. The software system shown in Figure 4.2 will be discussed in Section 4.4.2.

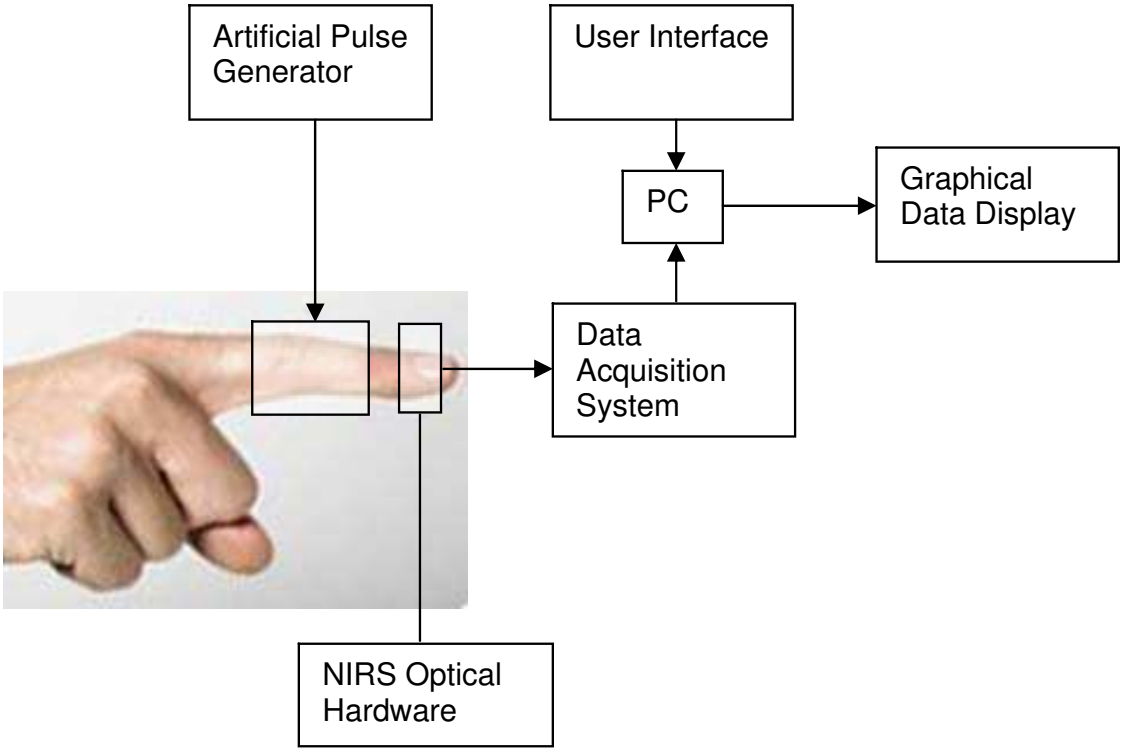

Figure 4.2: Overall APO System

In Figure 4.2, the NIRS hardware comprises of the LEDs that transmits the light through the finger to the photosensitive detector. The data-acquisition system comprises of the A/D converter and optical components driver.

4.3.1 Optical Components

The optical components of the APO system consist of two sensors, both consisting of a dual-wavelength LED assembly and the highly sensitive silicon photosensitive detector. The basic hardware structure that was used was that of a disposable pulse oximetry sensor as provided by Nonin Medical, Inc., the $Purelight^{TM}$ 7000A. The optical components of one of these sensors had to be modified to satisfy the low saturation system specifications, as stated earlier. These modifications entailed replacing the sensor LEDs with LEDs specifically suited to the measurement scenario. The other sensor, to be used in the unaffected tissue, high saturation scenario, was used with its original optical components.

The sensitivity and accuracy of pulse oximetry is highly reliant on the combination of LEDs used in the sensor design. In conventional pulse oximetry systems, the wavelengths of the two LEDs are chosen as to maximize the sensitivity of the sensor. This is achieved by choosing at least one of the wavelengths in a band where the difference in absorption coefficient for Hb and HbO_2 is notable (Mannheimer *et al.*, 1997). Absorption coefficients for Hb and HbO_2 can be seen in Figure 3.2. Commercial sensors usually employ a 660 nm (red) LED and a second LED in the 880-910 nm band or near to 940 nm.

Unfortunately, this combination is only suited to measuring saturation values in excess of 70%. Below this value, accuracy deteriorates drastically. Schmitt (1991) postulates that accuracy is affected by amplified variance in unbalanced multiple scattering effects caused by normal variations in physiological parameters such as residual blood volume, arteriovenous saturation difference and finger diameter.

This accuracy deficiency was addressed by utilizing light wavelengths other than those used in commercial sensors. These wavelengths were specifically chosen to improve accuracy at low saturations. The choice was based upon the work of Mannheimer *et al.* (1997), who tried to optimize accuracy at low saturations by matching perturbations in photon pathlength at the two wavelengths caused by physiological variations. Additionally, it was attempted to match the penetration depths of the two wavelengths to minimize the effects of tissue heterogeneity. After animal verification, it was concluded that a 735/890 nm LED combination would perform best in low saturation scenarios (Mannheimer *et al.*, 1997).

The new LEDs used in the design of the modified sensor were of the wavelengths

740 nm and 880 nm. The datasheets of these LEDs, ELS-740-994 and ELS-880-894-3, as supplied by Epigap Optoelektronik GmbH, can be found in Appendix A. Precise matches for the wavelengths required, could not be obtained, but the influence of the small wavelength discrepancies was assumed to be negligible. Although suited to low saturation value measurements, this combination has the negative effect of reducing sensor sensitivity drastically, resulting in small variations in R causing big variations in measured saturation values. This effect can be seen in the *in vitro* calibration curves, presented in Section 5.2. In selecting the above mentioned LEDs, three factors were considered, namely peak forward current, viewing angle and availability. As can be seen from Appendix A, the first two factors compared well for the selected LEDs. Ideally, selection would have been based upon radiant intensity as well, but values for this parameter were not provided for the available LEDs. The approach followed in this study thus assumed that intensity discrepancies would have a negligible effect on sensor performance. This assumption was based upon the possibility that the *in vitro* calibration would inherently compensate for the effects of an intensity mismatch.

The original LEDs, as used in the sensor for the unaffected tissue, were in the form of a dual wavelength LED of the wavelengths 660 nm and 910 nm. As explained earlier, this original combination is well-suited for a high sensitivity setup to measure saturation values in the range above 70%.

The photosensitive detectors, as supplied in the original sensors, were used in both prototypes. Two sensors were thus available for use in different scenarios, namely a highly sensitive 660/910 nm wavelength combination for use in high saturation scenarios and a less sensitive 740/880 nm wavelength combination for use in low saturation scenarios.

4.3.2 A/D Converter and Optical Driver

The analogue-to-digital (A/D) converter and optical driver system was designed as a combined system that is compatible with the Nonin *Purelight*^{TM} 7000A sensor, as mentioned in Section 4.3.1. The A/D converter converts and transmits the analog sensor PPG output, as produced by the photodetector, as the digital output needed by the PC. The optical driver drives the dual wavelength LED assembly at a specified duty cycle and emitting strength. The A/D converter and optical driver

system, as designed by GeoAxon (Pty.) Ltd., can be seen in Appendix B. Only this system was used as originally designed by another party, all other modifications and design were done by the author.

In Figures B.1 and B.2, the photodiode amplifier and A/D converter base is responsible for the microcontroller unit (MCU) and sensor integration. The analogue photodetector output is typically very small and needs to be amplified before A/D conversion. This variable gain amplification is done through the use of CD4053BC multiplexers and TLC2264 operational amplifiers. Amplifier gain is controlled by the MCU by means of ports PDA-SW-A to C and ports ADC-SW-A and B. Port CCP in Figure B.2 transmits the amplified sensor output to the MCU.

The power supply unit (PSU) in Figure B.3 consists of positive and negative voltage regulators, REG71050 and MAX889T, respectively. These regulators are responsible for the specified supply voltages as needed for the CD4053BC multiplexers. Power supply to these regulators is maintained via the USB port, in the form of port V-BUS.

A/D conversion is conducted in the MCU, as shown in Figure B.4. This system comprises mainly of a 18-bit PIC18F252 microcontroller, responsible for A/D conversion, photodiode amplifier gain regulation and LED control. The amplified sensor output, received via port CCP, is converted to a 16-bit digital representation and transmitted to the USB universal asynchronous receiver/transmitter (USB UART) unit via port TXD. The USB UART can be seen in Figure B.5. As mentioned earlier, photodiode amplifier gain is controlled via ports PDA-SW-A to C and ports ADC-SW-A and B. The dual LED assembly is directly driven by the MCU in a bridge configuration at a frequency of 50 Hz, with a measured 1% duty cycle and V_{on} = 4,4 V. Six output ports on the microcontroller have been connected in parallel to source the needed LED driving current for the specified emitting strength.

The USB UART is responsible for the transmittance of serial data to the PC via the USB port. This data transfer occurs using the communication setup as specified in Table 4.4.

In adapting the LEDs of the sensor, resistor R13 in Appendix B.4 had to be replaced to limit the current through the LEDs. Peak forward current for both LEDs is specified as 100 mA and peak pin source current for the microcontroller as 25 mA. This translated into a combined peak source current of 150 mA for the

Table 4.4: USB UART Communication Setup

Parameter	Setting
Baud Rate	38400
Data Bits	8
Stop Bits	1
Parity	None
Flow Control	Hardware Controlled

microcontroller. The LED peak forward current was thus the limiting factor and resistor R13 was replaced with a 51 Ω resistor to limit the current to (4.4/51) = 86 mA.

4.3.3 Artificial Pulse Generator (APG)

The artificial pulse generator (APG) forms the basis upon which this form of low perfusion oximetry rests. By inducing an artificial blood pulse in occluded or nearly occluded tissue, non-invasive pulse oximetry principles can be used to measure blood oxygen saturation. The APG consists of three subsystems, namely, the pneumatic pressure generator, electronic control system and pressure cuff. A basic layout of the APG can be seen below as Figure 4.3.

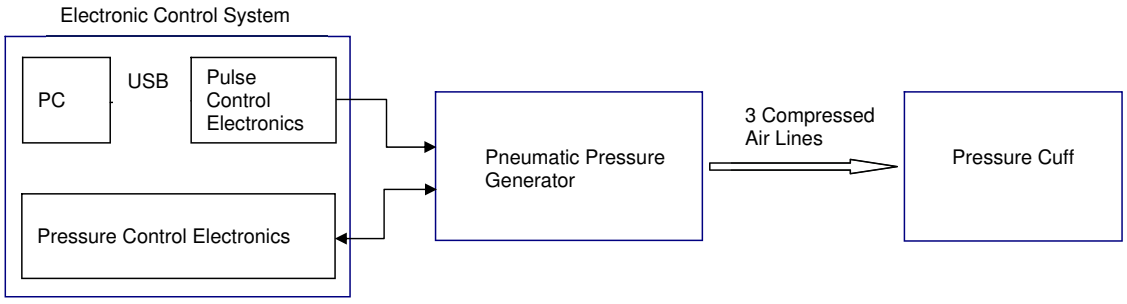

Figure 4.3: APG Layout

The pneumatic pressure generator was responsible for maintaining and supplying compressed air at a pressure of 600 mmHg. This pressure was chosen to ensure that cuff pressure sufficiently exceeds the normal systolic blood pressure of 120 mmHg and thus to ensure that a definite arterial pulse is generated in the affected tissue. A pressure slightly higher than systolic would normally be sufficient,

but due to the design of the pressure cuff, a much higher pressure had to be used. These design effects will be discussed in more detail in Section 5.4. The pneumatic setup and prototype can be seen as Figures 4.4 and 4.5, respectively. A dual compressor setup was used to ensure the correct air supply-demand balance, because the QJT-27QB compressor, as supplied by Mantech Electronics, can only supply 1,3l/min, which is less than the required flow rate. The accumulator was included to minimize the decrease in system pressure in high demand scenarios. The flow regulators were included to control the inflation speed of the pressure cuff. Uncontrolled inflation could rupture a tube in the pressure cuff. All components, except the compressors, were standard components, supplied by Festo. Catalog numbers for all the components can be found in Appendix C.

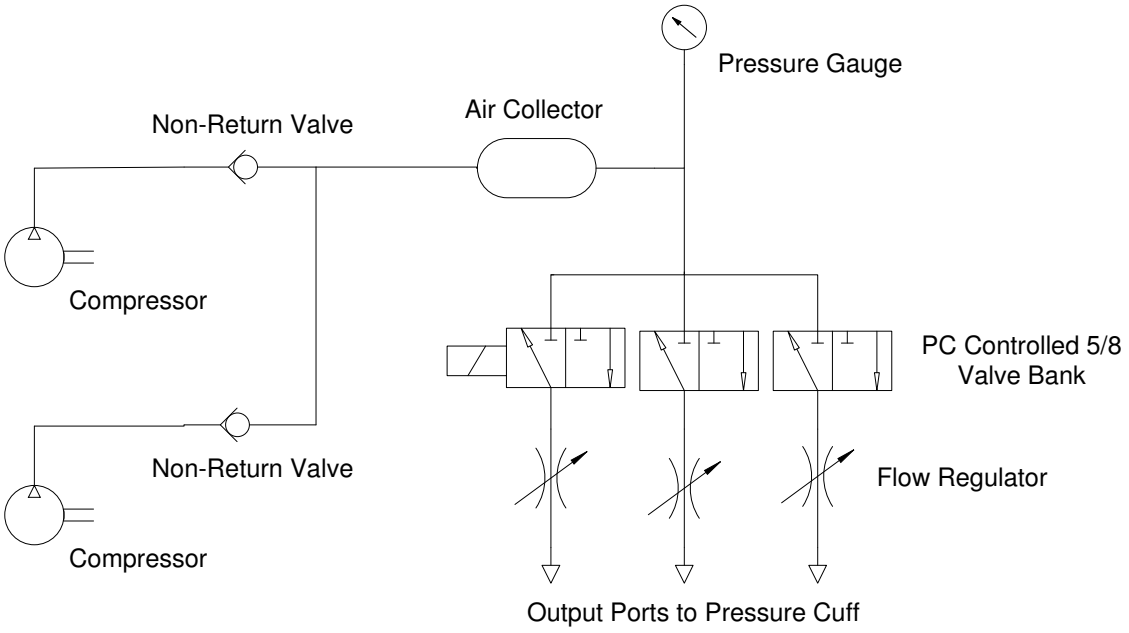

Figure 4.4: Pressure Generator

As can be seen from Figure 4.3, the electronic control system consists of two separate subsystems, namely, the PC-based pulse control system and the pressure control system. The pulse control system controls the pulse number, sequence, frequency and duty cycle, whilst the pressure control system regulates overall system pressure.

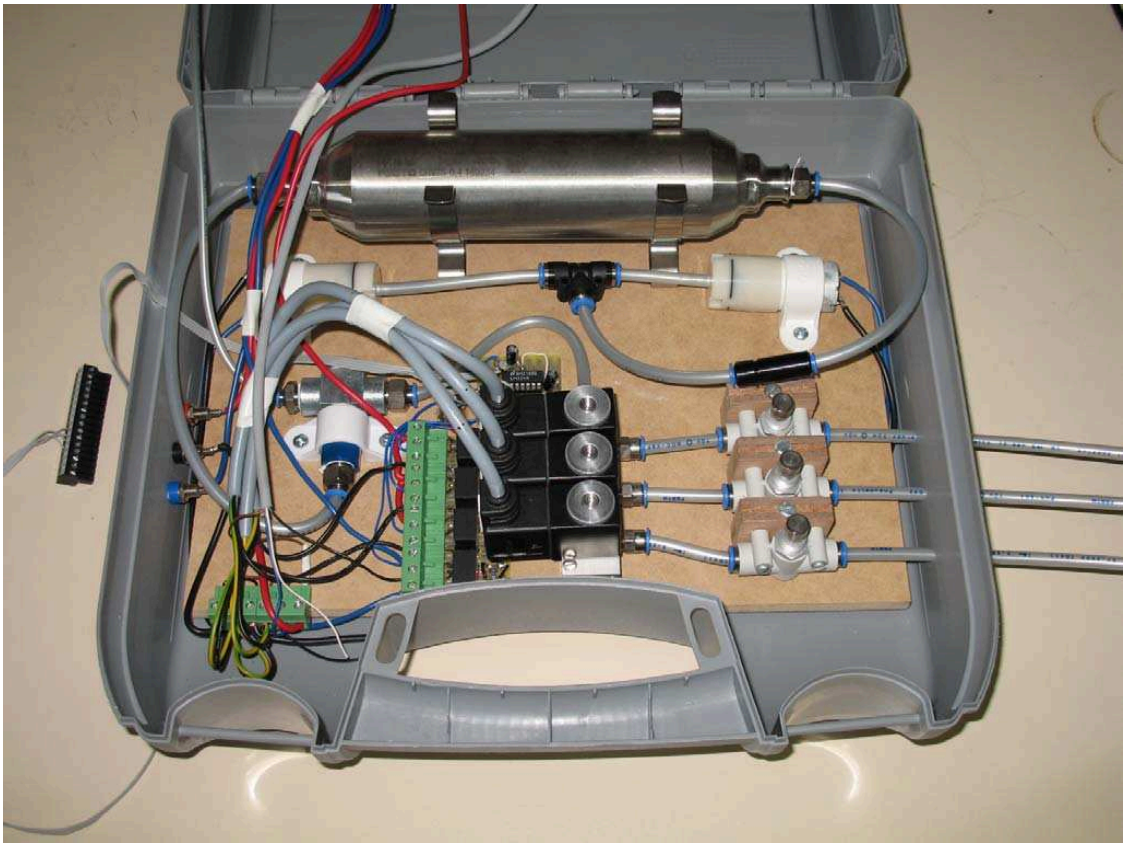

Figure 4.5: APG Prototype

The pulse control system consists of a Matlab based user interface to specify control parameters, a data acquisition module to generate hardware control outputs and output amplification hardware to control the solenoid-valve assembly. The Matlab based user interface will be discussed in Section 4.4.2.

A National Instruments USB-6218 data acquisition module (DAQ), was used to generate the control outputs according to the user specified control parameters. This module's digital output options and availability made it well-suited for this purpose, although it was not the most elegant solution. The active control output was a logic high to activate the solenoid controlled valve and to allow air to flow into the pressure cuff. The spring-loaded valve stopped air flow automatically in the event of a logic low output level.

The USB-6218 DAQ is only capable of sourcing a maximum output current of 16 mA at a logic high output of 3,7 V (National Instruments Technical Communi-

cations, 2006). Since the MSFG-24DC/42AC solenoid coils require a operating DC voltage of 24 V and source current of 188 mA (Festo Technical Communications, 2004), the DAQ would not be able to directly drive the coils. Output amplification hardware had to be included to achieve this. This hardware consisted of a voltage regulator, power amplifier and power relay. The voltage regulator was needed to convert the available 12 VDC to the 6 VDC needed by the power amplifier. The power amplifier was included to source the current needed to control the power relays, which in turn would switch the solenoid coils. A circuit diagram of the combined voltage regulator, power amplifier and relay can be seen in Figure B.6.

As can be seen from Figure B.6, a LM317 3-terminal adjustable regulator from Texas Instruments was used as a positive voltage regulator. The regulator circuit was provided by Fairchild Semiconductor Technical Communications (2005). Resistance values for R1 and R2 were calculated using the relationship

$$V_o = 1.25\left(1 + \frac{R2}{R1}\right) \tag{4.26}$$

with $V_o = 6\,\text{V}$. Values for C1 and C3 were obtained from Fairchild Semiconductor Technical Communications (2005). Capacitor C1 was included to prevent ripple amplification as the output voltage was raised. Regulator oscillation effects were reduced by including capacitor C2 into the design.

The power amplifier, as seen in Figure B.6, was designed using a LM324 operational amplifier to drive a 2N222 BJT transistor. By utilizing this setup, the transistor was used to deliver the needed switching current to the power relay. The FRS1-S power relay from Mantech Electronics was used to connect the solenoid coil to the 24 VDC it needs in its active state. Resistor R3 was included as current limiter, while capacitor C3 was included as default protection against supply ripple.

The pressure control system operated on the so-called 'bang-bang' control principle. By constantly comparing system pressure to a fixed set point, the compressors were either switched fully on or off. The compressors were switched on as soon as system pressure decreased below 0,78 bar and were switched off as soon as system pressure increased above 0,8 bar. This control principle was employed due to the need to minimize the time to return to the specified pressure. System pressure was monitored using a SDE1 pressure sensor from Festo, as can be seen in Figure 4.6 and Appendix C. Overvoltage protection was included in the form of a 4 A fuse.

The SDE1 uses a PNP output to provide a logic high output of 24 V if the pressure drops below the set point. Maximum output current for this pressure sensor is specified as 120 mA, eliminating the possibility of directly driving the compressors, as each QJT-27QB compressor draws a nominal current of 250 mA. A FRS1-S power relay was used to drive the compressor, with the control circuit connected to the SDE1, as shown in Figure B.7. Resistor R1 was included to limit the SDE1 output current to 50 mA.

Figure 4.6: APG Pressure Control

The pressure cuff was responsible for inducing the artificial pulse by inflating a system of tubes around the finger. Pressure exerted by the cuff was used to push residual blood into the area of interest. The cuff operated on the same principle as a conventional sphygmomanometer used to measure blood pressure. The cuff consisted of three separately inflatable, expandable tubes, each with an independent air supply. The inflatable tubes were contained in a fabric enclosure that would not yield under pressure. To account for patient variability, the deflated cuff was designed to wrap around the finger and be fixed at the right diameter with Velcro. By fixing the diameter in this way, tube inflation would decrease the inner diameter of the cuff and exert a definite internal force on the finger, regardless of finger diameter. The three independent air supplies can be seen in Figure 4.5 as the three tubes extending to the right. By inflating the three expandable cuffs in sequence, a

peristaltic effect was induced in the finger to create the artificial pulse. The whole cuff assembly can be seen as Figure 4.7, while all pneumatic components used can be seen in Appendix C.

Figure 4.7: APG Pressure Cuff

4.4 Software Development and Signal Processing

The software development entailed the development of a graphical user interface (GUI) to enable any user to easily operate the data acquisition system. The signal processing of the collected data was not included in the GUI, although this would be feasible for future versions.

4.4.1 Graphical User Interface

The Matlab-based GUI was primarily developed to simplify the data acquisition procedure. It was thus mainly used during the *in vitro* calibration and *in vivo* validation stages of the project. These stages will be discussed in Sections 4.5.3 and 4.6.2. A screen shot of the GUI can be seen in Figure 4.8.

The GUI only incorporated the most basic input parameters needed to collect and store the PPG and reference saturation data in MS Excel format. Other, more advanced, parameters were hard coded into the GUI m-file. These included

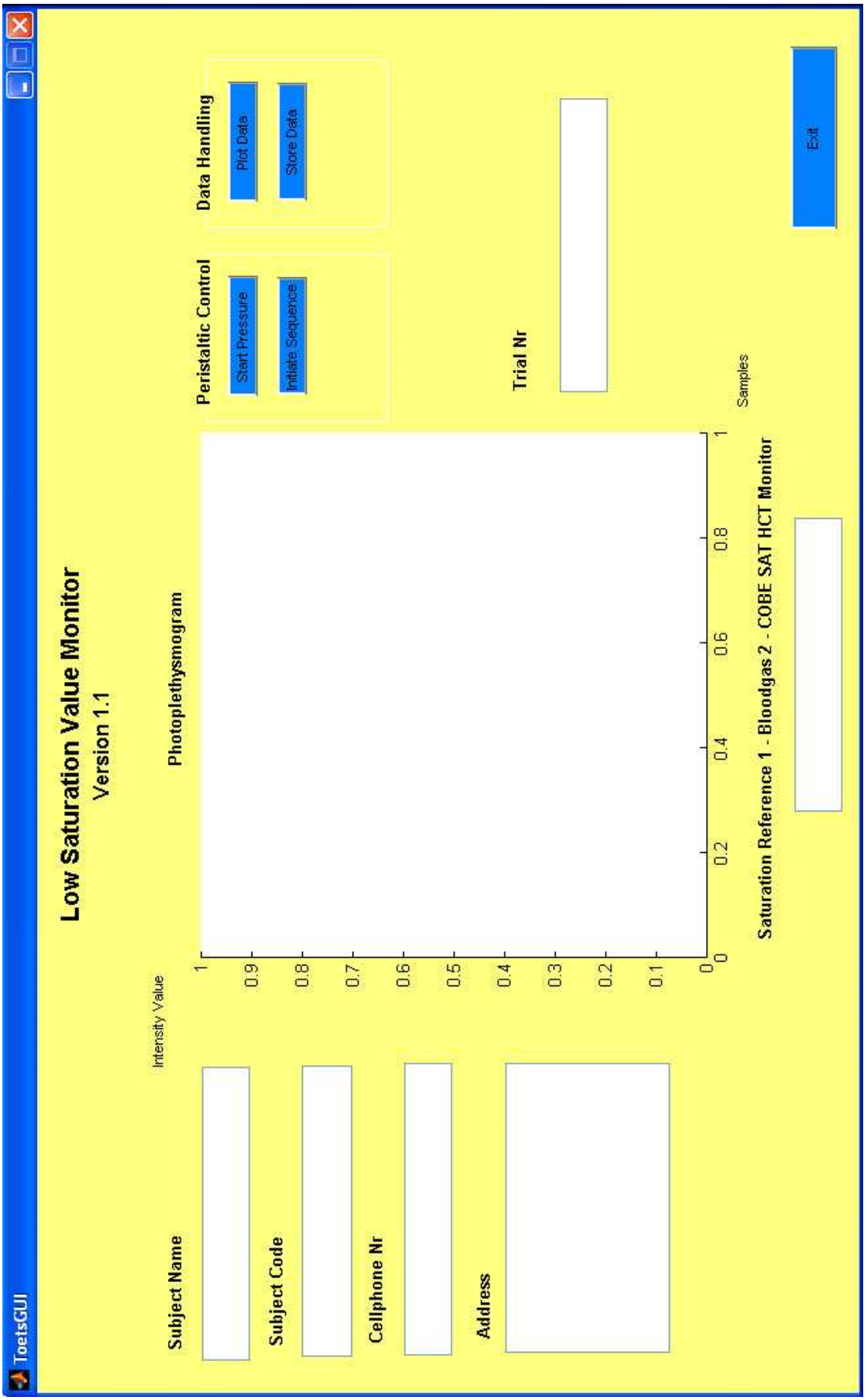

Figure 4.8: GUI

pressure cuff inflation sequence and timing and data collection time. In future versions of the GUI, inclusion of these parameters would be an option under an advanced parameter tab.

4.4.2 Signal Processing

The processing of the red and infrared PPGs was done using Matlab. The PPGs were processed to extract the normalized red-over-infrared ratio R. This ratio was then correlated with a specific blood oxygen saturation. The basic R extraction process can be seen as Figure 4.9. As the processing methods for both red and infrared PPGs were the same, the method will only be discussed in general.

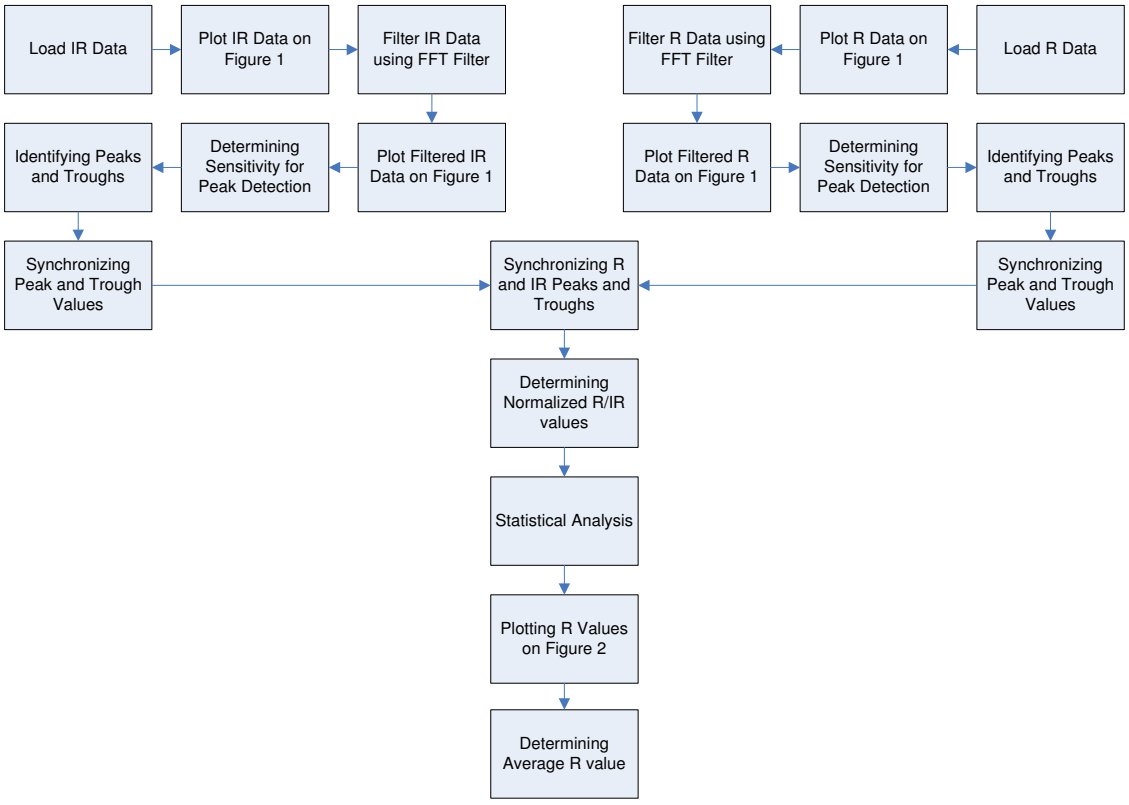

Figure 4.9: Signal Processing Overview

In Figure 4.9, the first steps were to load and plot PPG data. These data were stored in MS Excel format during the data acquisition stage, as explained in Section 4.4.1. Typical PPG data can be seen in Figure 4.10.

The frequency content of every PPG was initially examined using a Fast Fourier Transform, as seen in Figure 4.10(b). The y-axis values of the PPG in Figure 4.10(a) are arbitrary values allocated during the A/D conversion of the detected light intensities. The initial examinations revealed that random noise was almost always present in the PPGs. This noise would cause accuracy problems, as the actual peak and trough values of the PPG were used to calculate R. The major frequencies of this noise was always above 5 Hz and since the major pulse frequency content was usually below this frequency, a low pass digital filter was implemented at 5 Hz. In selecting this filter frequency, care was taken to ensure that only low energy harmonic pulse frequencies were filtered. It was assumed that since both red and infrared PPGs had the same major frequencies, filtering out pulse harmonics would not have a major effect on the calculation of R. After filtering the signal, the filtered signal was plotted with the unfiltered signal to allow visual inspection.

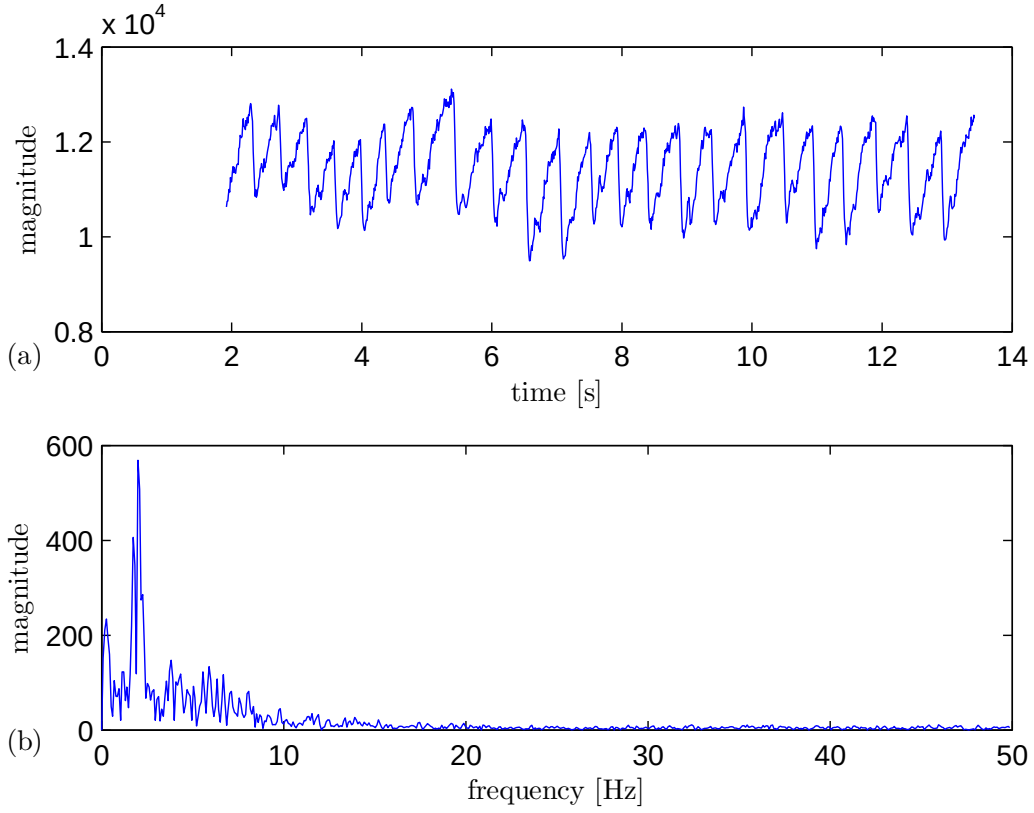

Figure 4.10: Typical PPG (a) and FFT (b)

The next step in processing the filtered PPG was to identify peaks and troughs. This was done using algorithms provided by Billauer (2007). This algorithm operates on the basis of detecting peaks and troughs in a signal and verifying their authenticity by checking if data points can be found on either side that are lower by a specified margin in the case of peaks and higher in the case to troughs. This margin corresponds to the sensitivity parameter shown in Figure 4.9. Detection sensitivity was calculated by subtracting the minimum signal value from the maximum and dividing the result with a user specified parameter. This parameter was usually in the range two to five and was selected based on an initial visual inspection of peak detection efficiency. This parameter was included to provide a simple method of adapting the peak and trough detection for poor PPG quality scenarios. By calculating sensitivity in this manner, it was ensured that peaks and troughs would not be missed in low perfusion scenarios.

After identifying all the peaks and troughs in the PPG, individual peak and trough values had to be synchronized. This was done to ensure that instantaneous values were as accurate as possible. Peak and trough values were identified where the time elapsed in between the peak and trough was less than half the average period of the PPG. In the event of a peak having both the trough before and after falling into this window, the closest trough was selected. This combination of a peak and its closest trough will be referred to as a peak-trough throughout this thesis.

Having identified the peak and trough pairs for the simultaneously recorded red and infrared PPGs, the red and infrared pairs had to be synchronized. This was achieved by grouping red and infrared pairs together where the time associated with each infrared peak fell into a 0,3 sec window around the red peak.

The normalized red/infrared ratio R was calculated for each peak-trough pair by first calculating the difference between individual peak and trough values for the red and infrared PPGs. This difference was then normalized with the average between the peak and trough values. After this, the normalized difference for each red peak-trough pair were divided by the normalized difference for the corresponding infrared peak-trough pair to obtain R.

These values for R were statistically analyzed before averaging using a box-and-whisker analysis as outlined by Vining (1997). Using this method, mild and extreme outliers were identified and discarded, provided that the unquestionable R

values were enough to deliver a meaningful average value for R. In the event of a lack of unquestionable values, the sensitivity parameter and filter cutoff frequency were revised. If this did not increase the number of unquestionable values, the averaged value for R was marked as possibly corrupt. Results for an exaggerated and real situation box-and-whisker analysis can be seen as Figures 4.11 and 4.12. In Figures 4.11 and 4.12 a range of R values were analyzed for mild and extreme outliers and marked accordingly. The exaggerated results of Figure 4.11 were obtained from initial experiments where the stability of R was low, while Figure 4.12 shows more stable R values from later experiments.

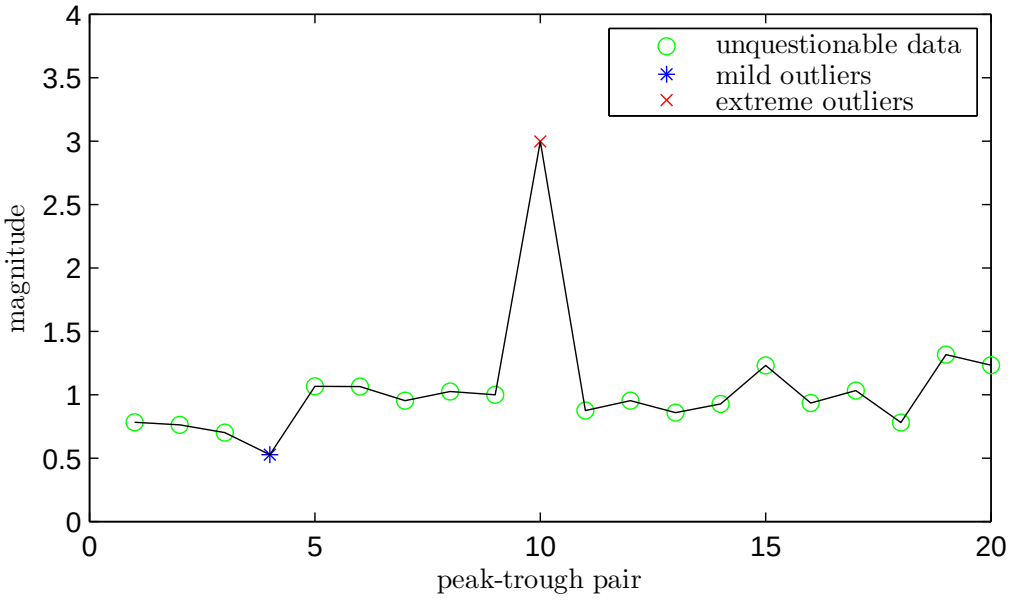

Figure 4.11: Exaggerated Statistical Analysis of R

After the averaged value for R was calculated, the blood oxygen saturation that corresponded with this value of R were found by utilizing a lookup table formulated during the *in vitro* calibration phase. This stage of the project will be discussed in Section 4.5. An alternative to this approach was to utilize a calibration curve calculated using the system simulation as discussed in Section 4.2.2.A for S_aO_2 and Section 4.2.2.C for S_vO_2. Results for both these approaches will be discussed in Chapter 5.

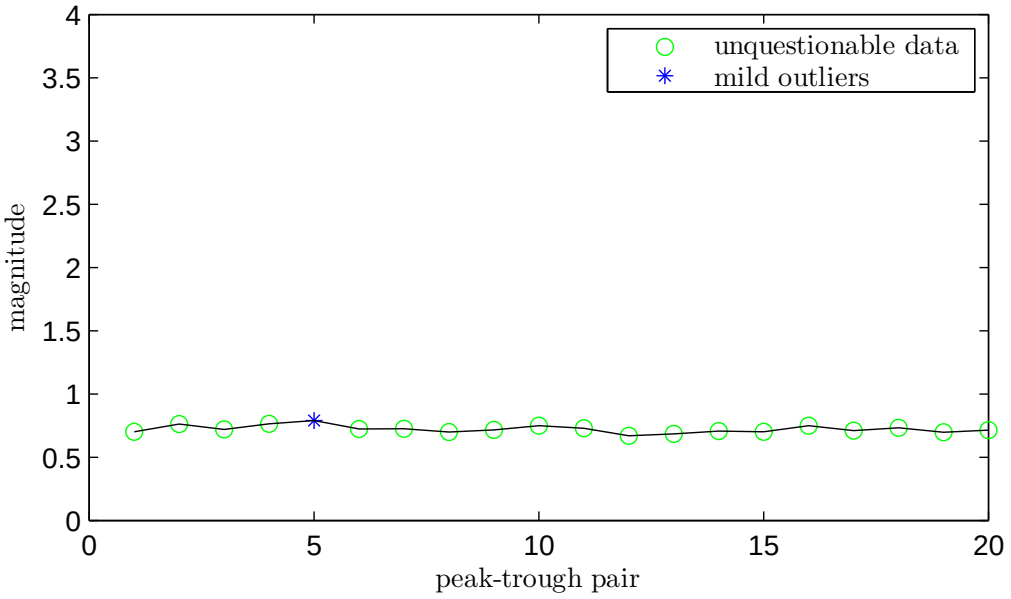

Figure 4.12: Real Statistical Analysis of R

4.5 System Calibration

All pulse oximeters rely on a calibration procedure to obtain R values for specific S_pO_2 values. This calibration procedure is a critical stage in the development of a pulse oximeter and eventually plays a major role in the accuracy of the system.

Two calibration approaches are possible, namely theoretical and empirical. The theoretical approach based on Beer-Lambert's law has been shown to be inaccurate, although recent revisions of Beer-Lambert's law have shown improved accuracy (Schmitt, 1991). Empirical calibration is currently the method of choice for pulse oximeter manufacturers, due to its accuracy (Webster, 1997). The empirical calibration route was also followed in this study, although theoretical results, as obtained from the model discussed in Section 4.2.2.A, will be compared with this approach in Section 5.4.

Empirical calibration procedures typically entails measuring a reference quantity, with optical properties resembling human tissue with a known S_aO_2, to obtain R values correlating to a specific S_pO_2. As stated earlier, the end result of this calibration procedure is a calibration curve which correlates R to S_pO_2.

4.5.1 Available Empirical Calibration Methods

The empirical calibration approach can be divided into two different categories, namely *in vivo* and *in vitro* procedures.

In vivo calibration entails directly comparing R values obtained by measuring human subjects to S_aO_2 values obtained from blood samples withdrawn from the subjects. Subjects are systematically desaturated by inhaling mixtures of air that contains decreasing concentrations of oxygen. S_aO_2 values are obtained by analyzing blood samples from the subjects at each step using a multi-wavelength co-oximeter. Measured R values are plotted against the reference S_aO_2 values to obtain the calibration curve. The *in vivo* procedure is currently used by the majority of manufacturers (Stabile and Reynolds, 2002), due to its inherent accuracy as a result of the real physiological parameters present during the calibration procedure. One disadvantage of this procedure lies in the fact that due to the possibility of brain damage at saturations below 70%, *in vivo* calibration curves are only based on real values in the region of 70-100% saturation (Stabile and Reynolds, 2002; Hornberger *et al.*, 2002). Below 70% saturation, the calibration curve is based on the extrapolation of the real data, resulting in notoriously inaccurate readings below 70%. Additionally, effective *in vivo* calibration is a costly and complex procedure and is only conducted by the manufacturers themselves and a few specialized laboratories (Hornberger *et al.*, 2002).

In vitro calibration entails comparing R values obtained by measuring the transmittance or reflectance of light of a tissue phantom or simulator that is able to accurately mimic the optical properties of tissue perfused with blood at a specific saturation. The type of tissue phantom distinguishes the different types of *in vitro* procedures. Tissue phantoms vary in composition of the optical absorbing substance, some utilizing blood, others blood simulating substances and some opto-electronic or purely electronic systems (Stabile and Reynolds, 2002).

Blood phantoms, as used by Edrich *et al.* (1998), Edrich *et al.* (2000) and Volgyesi *et al.* (1990), are phantoms where human blood is used as primary absorber in a *cuvette* which mimics the absorption and scattering properties of bloodless tissue, bone and skin. Blood is pulsed through the *cuvette* or rotated in a mechanical system to mimic the pulsatile behaviour of blood in the arterioles and capillaries (Stabile and Reynolds, 2002). The saturation of this blood is controlled using

an oxygenator and measured using a reference co-oximetry system. R values are measured on the phantom whilst the blood is systematically desaturated. The main advantages of using this approach includes the use of blood as an absorber and the ability to desaturate the blood to very low values. Disadvantages include the difficulty of obtaining stable saturation values, the complexity of obtaining a *cuvette* which accurately mimics tissue absorbing and scattering properties (Stabile and Reynolds, 2002) and the detrimental effects of pulse shape and blood flow velocity in *cuvette* systems (Edrich *et al.*, 1998).

Tissue phantoms that employ techniques that simulate the absorption and scattering properties of human blood, have been used by Leuthner (1994), Mundley *et al.* (1989), Aoyagi (1994) and Zhou *et al.* (1993). In the first three of these systems, the light absorption properties of blood was simulated by either solutions infused with differing amounts of dye or tinted resins. These blood simulating absorbers were mechanically manipulated to induce pulsatile absorption behaviour. The system used by Zhou *et al.* (1993), utilized a liquid crystal retarder (LCR) to simulate the pulsatile absorption properties of blood. By adjusting the supply voltage to the LCR, the intensity of the light transmitted through the LCR could be modulated, while polarizers provided the static absorption that originates from bloodless tissue, skin and bone. The advantage of using these systems was the degree of standardization that could possibly be achieved, as well as eliminating the problems associated with working with human blood. Disadvantages included the complexity of accurately preparing the absorbers and scatterers to simulate the optical properties of human blood and bloodless tissue, skin and bone, as well as ignoring many of the complex liquid crystal properties in the case of Zhou *et al.* (1993) (Stabile and Reynolds, 2002).

An opto-electronic calibrator, as designed by Hornberger *et al.* (2002), operated under the principle of isolating the sensors LEDs from the photodetector and simulating light-tissue interaction based on data stored on a PC. In the system designed by Hornberger *et al.* (2002), a spectrometer and photodetector unit were used to analyze the sensor LED's optical properties. These properties were used as input to a computer algorithm with access to a large database of patient transmission spectra. Using user-specified patient spectra, with their corresponding arterial saturations, the transmission properties of light emitted by the sensor LEDs were calculated and simulated using LEDs on the calibrator. Light emitted by the cali-

brator LEDs were detected by the sensor photodetector. Main advantages of using this system, includes the re-usability of recorded patient data and the high degree of standardization that can be achieved. The main disadvantages of this system are the limitations on sensor models that can be tested, as a result of the calibrator LED wavelengths, as well as the fact that infrared emission by the red LED was ignored (Hornberger *et al.*, 2002).

Purely electronic simulators, such as the SmartSat Pulse Oximetry Analyzer manufactured by the Clinical Dynamics Corporation (Clinical Dynamics Corporation, 1996), employ a probe that directly plugs into the sensor port of the pulse oximeter. The simulator processes the LED driving currents and sources a simulated photodetector current to the pulse oximeter. This photodetector current is modulated according to LED driving current and a database containing manufacturer supplied calibration information. Advantages of using this system includes the high degree of standardization that can be achieved and the capability of effectively simulating a variety of physiological scenarios. The main disadvantage is the dependency of the simulator on manufacturer supplied calibration information (Stabile and Reynolds, 2002).

A calibration technique using a blood phantom as described by Edrich *et al.* (2000), was used in this study. The selection of this technique was based upon the need to calibrate the APO at high and very low saturations and the special wavelengths of light used at low saturations. The low saturation calibration requirement eliminated the possibility of using an *in vivo* calibration technique. Additionally, the complexity and repeatability issues of preparing solutions that accurately simulate the light absorbing properties of human blood at various saturations, eliminated the blood simulators as a possibility. The opto-electronic and electric calibrators were not an option, based upon their dependency on data collected for specific wavelengths used by specific sensors. As mentioned earlier, the selected blood phantom method also has its drawbacks, but care was taken to minimize these factors during calibration.

4.5.2 Calibration Setup

The *in vitro* setup utilized to calibrate the sensor hardware was selected based on the ability for low saturation calibration and the inherent accuracy that could

be obtained through the use of human blood. This calibration setup was derived from studies done by Edrich *et al.* (1998) and Edrich *et al.* (2000) and is shown in Figure 4.13.

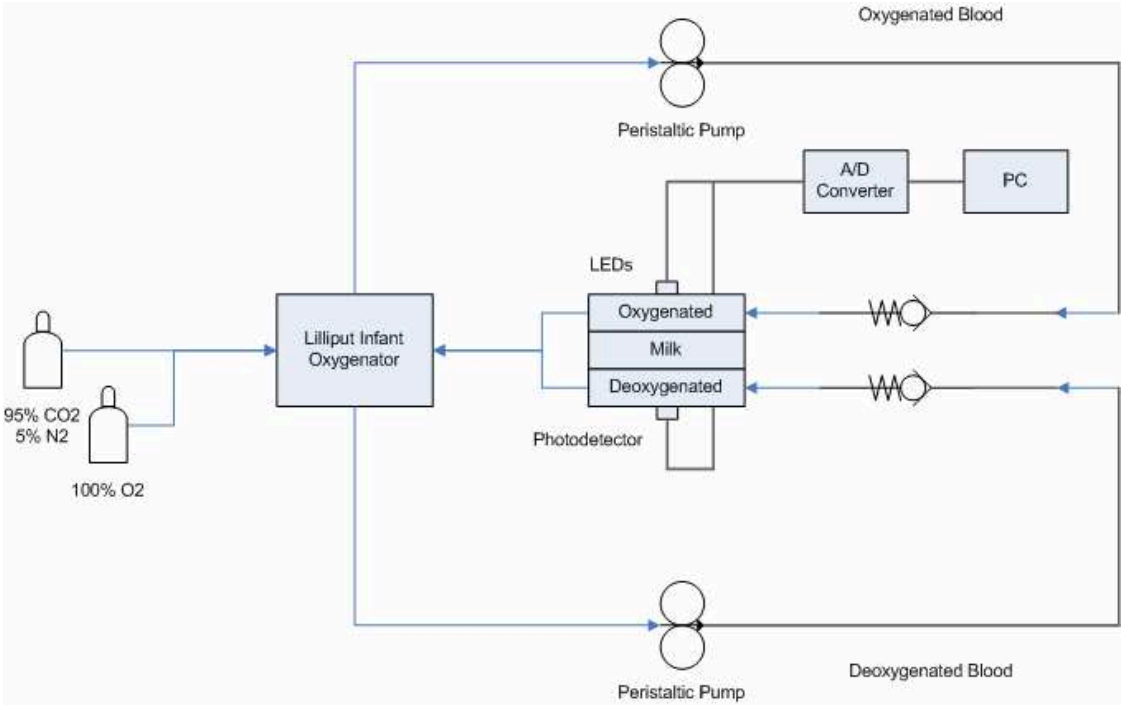

Figure 4.13: *In Vitro* Calibration Layout

The calibration setup consisted of two identical calibration sub-circuits, namely the arterial and venous circuits. These circuits could be connected by means of a three-way valve assembly. The arterial circuit was used to calibrate the sensors for conventional operation, while the venous circuit was used in conjunction with the arterial circuit to verify the hypothesis that the overall absorption by two volumes of blood with differing oxygen saturations would be a linear combination of the individual saturation values. The circuit was an open system designed to circulate human blood through an optical *cuvette* at a user-specified oxygen saturation.

A constant flow peristaltic pump was used to circulate the blood after removing one of the two impeller arms to obtain pulsatile flow. Non-return valves from Festo had to be included to prevent blood flowing back to the pump during the non-

contact periods caused by removing the impeller arm. Pulse rate was controlled by adjusting the rotational speed of the pump.

A D901 Lilliput 1 oxygenator from *Dideco* was used to oxygenate or deoxygenate the circulating blood. Oxygenation or deoxygenation was achieved by either connecting a 100% oxygen supply or a 95% nitrogen and 5% carbon dioxide mixture to the oxygenator. A lean mixture of carbon dioxide was used decrease the degree of desaturation during a desaturation step. This increased the resolution of the calibration curve by increasing the amount of saturation points measured during the desaturation sequence. The laboratory setup, showing the Lilliput oxygenator on the left and the peristaltic pump on the right, can be seen in Figure 4.14

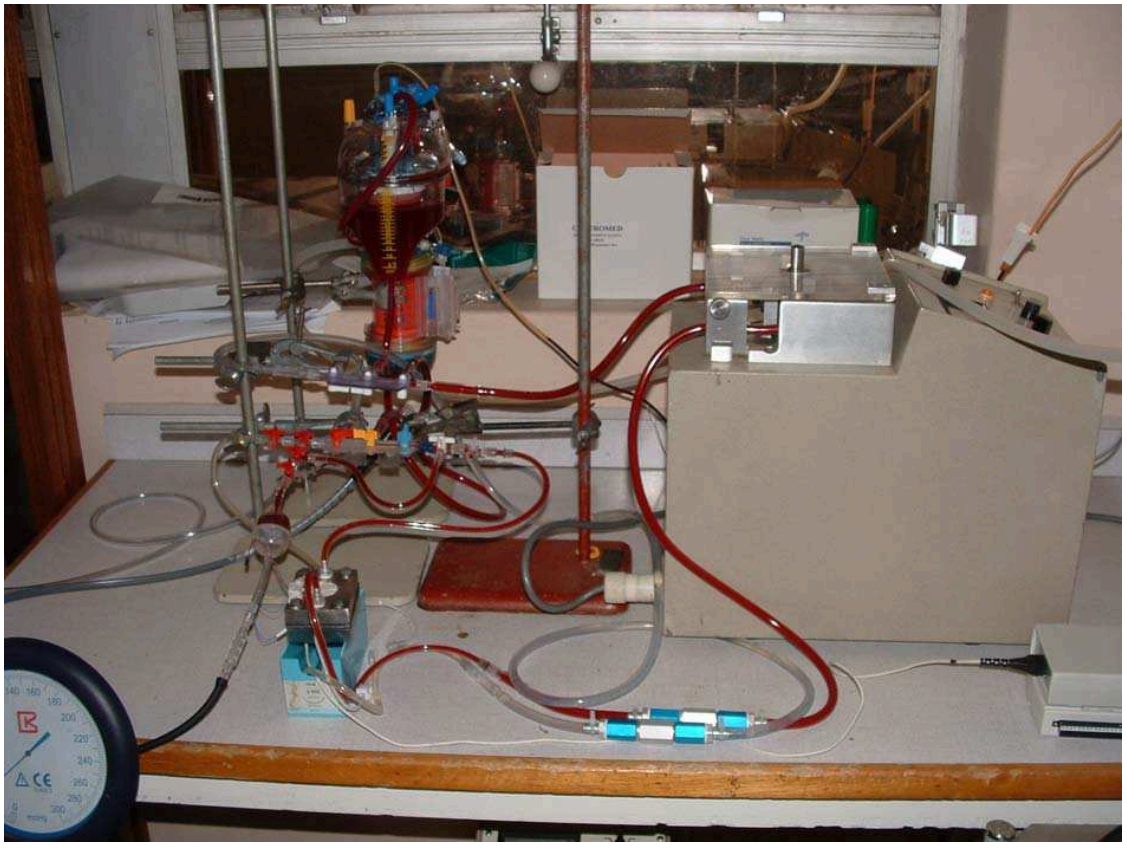

Figure 4.14: *In Vitro* Calibration Setup

A tri-chamber stainless steel *cuvette* was used in this study, inspired by the dual-chamber *cuvette* designed by Edrich *et al.* (2000). The tri-chamber *cuvette*

was designed to provide for separate arterial and venous blood channels, as well as a diffusor chamber. A cross-sectional view of the *cuvette* is shown in Figure 4.15.

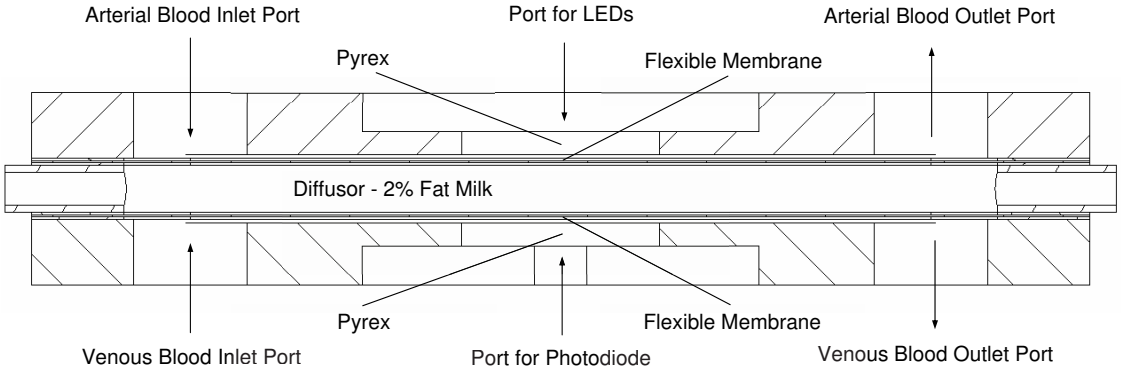

Figure 4.15: *Cuvette* Cross-section

Homogenized 2% low fat milk was used as a diffusor to simulate the scattering properties of bloodless tissue, skin and bone (Edrich *et al.*, 2000). The chambers were seperated by flexible membranes that would outwardly deform if pressure was applied to the chambers. This simulated the physiological conditions studied by Aoyagi (1994), where light absorption changed inversely with respect to absorber depth. AC behaviour in the PPG was mainly due to changes in blood channel depth during pressure fluctuations caused by the pump. Milk pressure was not regulated in this study. The blood flow channel and diffusor chamber dimensions was selected at 0,3 and 4,0 mm to simulate a blood volume percentage of approximately 10% in human tissue. The *cuvette* was designed using stainless steel to prevent external light contamination of the PPGs. Pyrex glass was selected as the windows for the LEDs and photodiode, based on the assumption that any optical interference by the glass would be included in the DC component of the PPG.

The assembled *cuvette* can be seen as Figures 4.16 and 4.17, while detailed drawings can be found in Appendix C. Barbed nipple fittings from Festo, with catalogue numbers specified in Appendix C, were used as interface with the circulatory system.

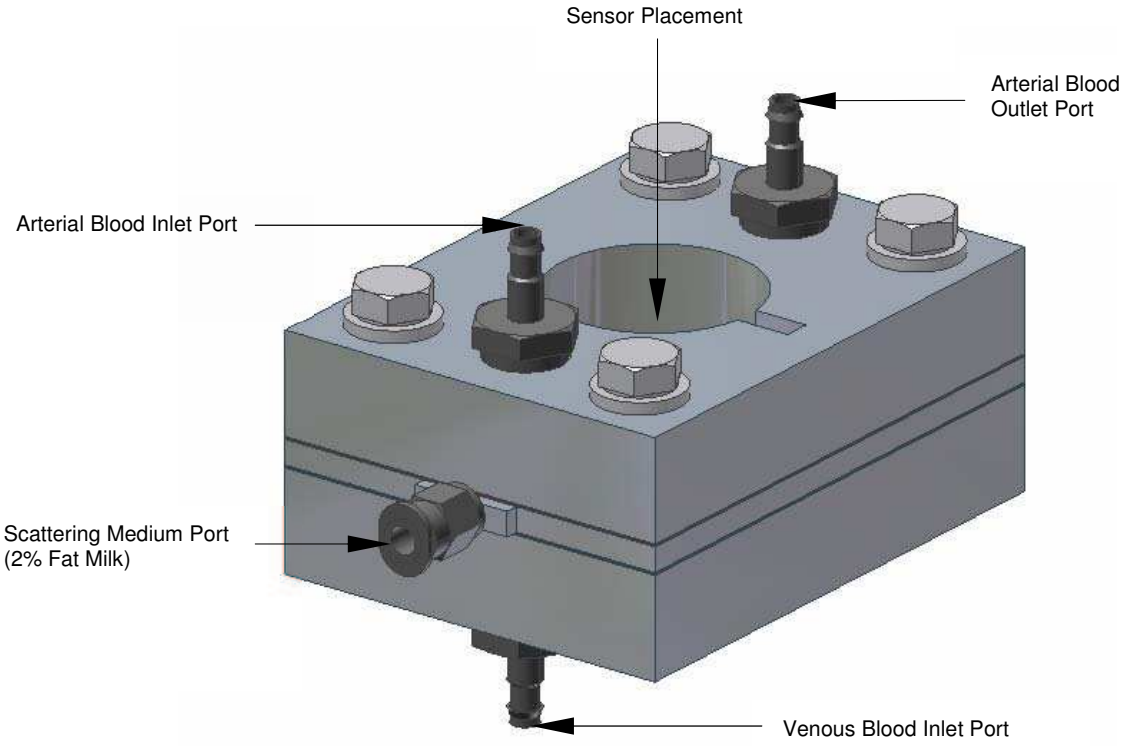

Figure 4.16: 3-D *Cuvette* Model

4.5.3 Calibration Procedure

The overall goal of the calibration procedure was to obtain a calibration curve, where the APO's output ratio R could be correlated with blood oxygen saturation values. This process entailed measuring R whilst desaturating fully saturated human blood to a value of $SO_2 \leq 10\%$.

Expired whole human blood from the blood repository at Tygerberg Academical Hospital was used as principal absorber during the calibration test. Care was taken to ensure that blood more than three days past the expiry date was not used. Older blood displays advanced levels of haemolysis, resulting in different optical properties than that of normal human blood. Three days were assumed a safe cutoff limit, as blood that is close, but still within its expiry date, is still suitable for human use and does not deteriorate rapidly under refrigerated conditions. All blood was tested before calibration for elevated lactate and low hematocrit levels, both being indicators of haemolysis. A hematocrit of 26% was considered to be the lower limit

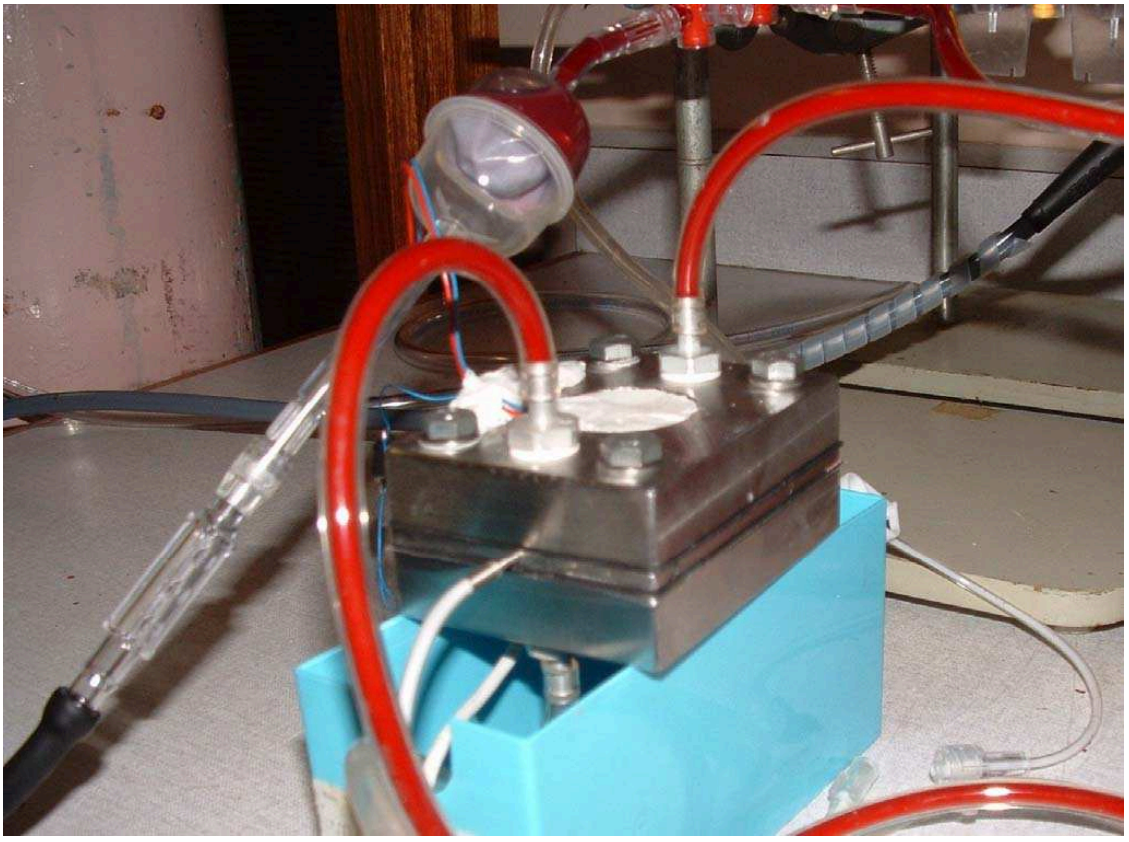

Figure 4.17: Assembled *Cuvette*

for inclusion.

The calibration procedure was divided into two phases, namely conventional arterial calibration and arterio-venous validation. During the conventional arterial calibration only the arterial circuit in the calibration setup was used. Both the arterial and venous circuits were used during the arterio-venous validation stage. The calibration procedures for the 660/910 nm and 740/880 nm sensors were conducted as two separate runs, although the procedures were identical for both sensors.

For the arterial calibration, the entire circuit was first primed using a 0.9% saline solution. Homogenised 2% low fat milk was injected into the diffusor chamber. All excess saline in the oxygenator's reservoirs was drained via a three-way valve at the lower part of the circuit. Approximately 500 ml of blood was directly injected into the oxygenator's venous reservoir via an input port on the reservoir. The peristaltic pump was started and the drainage valve was used again to drain excess saline in the piping of the system. This excess saline drainage was done to keep hematocrit

levels as close as possible to normal.

A 100% supply of O_2 was connected to the gas port of the oxygenator and enough time was allowed for the whole blood sample to be fully oxygenated whilst the pump circulated the blood. A blood sample was taken via a sample port included in the circuit directly after the oxygenator. This sample was analyzed for S_cO_2 using a Bayer Rapidlab 865 blood gas analyzer. This analyzer was used as the golden standard reference system throughout the *in vitro* calibration phase. The sensor being calibrated was activated and PPG data recorded for a period of 48 seconds using the GUI as discussed in Section 4.4.1. These data were stored in conjunction with the reference S_cO_2 value as determined using the blood gas analyzer.

The O_2 supply was now disconnected and replaced with the 95% N_2/CO_2 gas supply to deoxygenate the blood. A short period of time was allowed for a volume of blood to be partially deoxygenated as the blood was circulated by the pump. The deoxygenation process occurs as a result of the low O_2 concentration in the capillary gas exchange surfaces of the oxygenator. O_2 diffusing from the blood to the gas exchange system is removed from the system by the flow of excess N_2/CO_2 that vents to the atmosphere. The N_2/CO_2 supply was stopped after a short period and enough time was allowed for the saturation to stabilize throughout the system at a lower value. A reference blood gas sample was taken and analyzed for S_cO_2. PPG data was again recorded and stored in conjunction with the reference S_cO_2 value.

This deoxygenation process was conducted repeatedly to obtain data at stepwise decreasing saturation values, down to a saturation value $\leq 10\%$. This completed the data recording stage of the arterial calibration.

The stored PPG data were analyzed and averaged R values calculated using the software approach as outlined in Section 4.4.2. Using the calculated R and corresponding S_cO_2 values, the arterial calibration curves for the 660/910 nm and 740/880 nm sensors were constructed. These curves will be displayed and discussed in Section 5.2.

As mentioned earlier, the arterio-venous validation phase used both the arterial and venous circuits. Both circuits were primed in a similar manner to the arterial calibration phase and milk injected into the diffusor chamber. Approximately 1000 ml of whole blood was injected into the oxygenator's venous reservoir and

excess saline drained.

The blood was fully oxygenated using the O_2 supply, whilst circulating through both the arterial and venous circuits. Reference blood samples were taken from both the arterial and venous circuits and analyzed, whilst PPG data for the sensor were collected. This PPG data was stored in conjunction with the reference S_cO_2 values for both circuits.

The arterial circuit was then isolated from the venous circuit using a three-way valve system. Only the venous blood now circulated through the oxygenator, whilst the arterial blood bypassed the oxygenator and was fed back directly to the pump and *cuvette*. The N_2/CO_2 supply was now connected to the gas port, replacing the O_2 supply. A short period of time was allowed for a volume of the venous blood to be partially deoxygenated. The N_2/CO_2 supply was stopped and time allowed for the saturation in the venous circuit to stabilize. This dual process was conducted to provide two separate circuits, containing blood at different saturations, flowing through the *cuvette*. A dual reference sample was withdrawn from the arterial and venous circuits, analyzed for $S_{ca}O_2$ and $S_{cv}O_2$ and stored with PPG data collected during the analysis.

The venous desaturation and PPG data collection was repeated until $S_{cv}O_2$ reached a value of approximately 60%. After completing the data collection stage, the combined averaged R values for both circuits were calculated using the approach outlined in Section 4.4.2. The results will be shown and discussed in Section 5.2.

4.6 System Validation

The system validation phase of the prototype development entailed collecting and analyzing PPG data from human volunteers and using these data in correlation with the calibration curves presented in Section 5.2 to calculate either $S_{pa}O_2$ or $S_{pv}O_2$. These calculated values were compared with reference $S_{ca}O_2$ or $S_{cv}O_2$ values obtained using a Bayer Rapidlab 865 blood gas analyzer to analyze blood samples withdrawn from the volunteers.

Four objectives were identified for the system validation. These were:

1. To verify the operation of the APG.

2. To determine the accuracy of the calibration curves presented in Section 5.2 at high saturation values. This objective involved only the 660/910 nm sensor in conventional pulse oximeter mode, as this sensor was well-suited to high saturation values and naturally detectable PPG data was available.

3. To determine the accuracy and validity of the hypothesis that that the overall absorption by two volumes of blood with differing oxygen saturations would be a linear combination of the individual saturation values. Only the 660/910 nm sensor was tested in conjunction with the APG for this objective, due to time constraints imposed by the testing procedure. This will be discussed in more detail in Section 4.6.2.

4. To determine the accuracy of above-mentioned calibration curves for both the 660/910 nm and 740/880 nm sensors at low saturations. The APG was used to generate artificial PPG data for this objective.

4.6.1 Test Population

Ethical approval for conducting the *in vivo* tests was obtained from the Comittee of Human Research at the University of Stellenbosch. Twelve Volunteers, complying with inclusion criteria, were recruited from the University of Stellenbosch campus. The inclusion criteria were:

1. Volunteer weight $\geq 50\,\text{kg}$
2. Volunteer age ≥ 18 years
3. Written informed consent had to be given
4. Volunteer blood parameters had to be normal

All *in vivo* tests were conducted at Tygerberg Academical Hospital on six different days. Two volunteers were tested during each day, with each test lasting approximately 30 minutes.

4.6.2 Procedure

The room in which the clinical testing was conducted, was prepared beforehand by the clinical assistant. The system was set up in the prepared room and pretesting procedures completed to ensure correct operation of the system.

Each test subject was firstly informed on all the risks associated with the test procedure and was required to sign a written informed consent form to participate in the testing. The subject was then asked to sit in a chair next to the test bench to support the subject's left arm and to keep movement to a minimum during the testing procedure.

A pressure cuff from a conventional sphygmomanometer was wrapped around the subject's lower left arm, to be inflated during a later stage of the validation procedure to simulate the occluded nature of tissues affected by peripheral vascular afflictions. Occlusion had to be simulated to validate the APO's performance, due to the lack of patients suffering from diseases such as *meningococcemia*. The APG's pressure cuff was positioned around the subject's left hand index finger. After this, the 660/910 nm sensor was positioned on the tip of the subject's left hand index finger. This setup can be seen in Figure 4.18.

A capillary blood sample was withdrawn from the subject's right hand by means of a normal blood withdrawal procedure conducted by the clinical assistant. The $S_{ca}O_2$ of this blood sample was measured using a Bayer Rapidlab 865 blood gas analyzer. This saturation value served as the golden standard for comparison with $S_{pa}O_2$ values calculated by the APO system . Three $S_{pa}O_2$ values were sequentially measured, using the system with the 660/910 nm sensor in a similar manner to conventional systems, with the wrist cuff and APG deflated or inactive. All PPG and saturation data were stored in MS Excel. This concluded the high saturation validation procedure. Results for the high saturation validation will be discussed in Section 5.3.2.

For the APG operation and arterio-venous hypothesis validation objectives, the wrist cuff was inflated to a pressure of 160 mmHg. This pressure was sufficient to cut off all normal blood circulation to the subject's hand to simulate the occluded nature of affected tissue. Occluded PPG data were collected and stored for the validation of the APG's performance. A venous blood sample was immediately withdrawn from a vein on top of the subject's left hand and analyzed using the

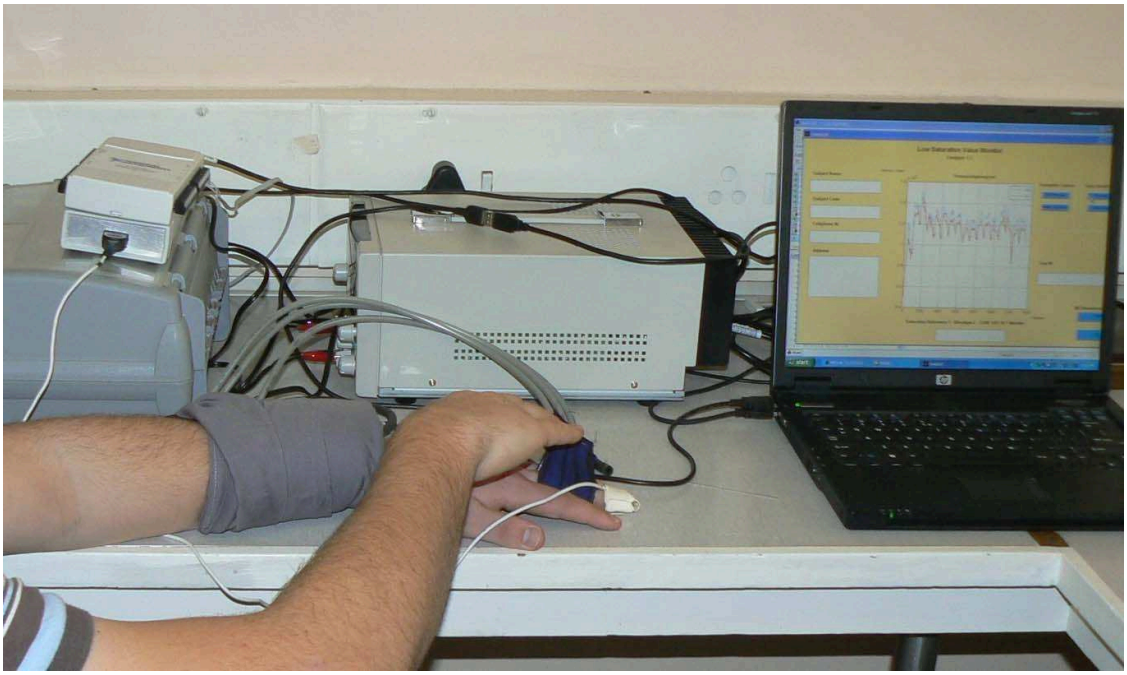

Figure 4.18: *In Vivo* Validation Setup

blood gas analyzer to obtain a $S_{cv}O_2$ value. The APG was activated directly after withdrawing the venous sample. The artificial PPG that was induced in the finger was measured using the 660/910 nm sensor, analyzed for $S_{pv}O_2$ and stored in conjunction with the reference $S_{cv}O_2$ value. In testing the validity of the arterio-venous hypothesis, stated as objective three in Section 4.6, it was assumed that S_aO_2 would remain stable for long enough after occlusion to assume that the $S_{ca}O_2$ measured for the high saturation validation could be used as input to calculate $S_{pv}O_2$. Due to the time needed to collect PPG data for the 660/910 nm sensor, S_aO_2 would decrease to a unknown value if PPG data had to be collected for the 740/880 nm sensor as well. Thus only the 660/910 nm sensor was tested in validating the arterio-venous hypothesis. Results for the APG operation and arterio-venous hypothesis validation will be discussed in Sections 5.3.1 and 5.3.4, respectively.

The wrist cuff was kept inflated for a short period of time, typically 5 minutes, to allow overall saturation values in the tip of the subject's left index finger to decrease to a suitably low value. This was done as to validate the low saturation performance of the APO, as stated in Section 4.6. Care was taken to ensure that the time elapsed

from wrist cuff inflation to wrist cuff deflation did not exceed 10 minutes to ensure that no tissue damage occurred due to O_2 deprivation. The subject was in control of the pressure release valve of the lower arm cuff at all times to enable him/her to release the pressure if undue discomfort was experienced in the hand. A capillary blood sample was withdrawn from one of the subject's left hand fingers by the clinical assistant. Due to the occlusion of the hand, it was not always possible to obtain a full blood sample from one finger alone. In the event of this happening, a second finger was pricked and palpated to obtain a full sample. Differences in the capillary saturation values between fingers were assumed to be negligible. The blood sample was analyzed to obtain a S_cO_2 value using the reference blood gas analyzer. The APG was activated directly after withdrawing the capillary sample. The artificial PPG that was induced in the finger was measured by first using the 660/910 nm sensor and then the low saturation 740/880 nm sensors. All PPG data were processed to obtain S_pO_2 values and stored in conjunction with the measured S_cO_2 values. Results for the low saturation validation will be discussed in Section 5.3.3.

After the procedure was completed, the APG system was deactivated by means of the GUI on the PC and the APG deflated. The lower arm cuff was deflated and removed, restoring normal blood circulation in the subject's hand. After this, the sensor and APG was removed from the subject's finger, signaling the end of the validation procedure.

Chapter 5

Results

An overview of the system development as described in Chapter 4 can be seen in Figure 5.1. The main aim was to accurately measure SO_2. A system was designed to measure SO_2 in low saturation and perfusion scenarios. The system was calibrated using an *in vitro* calibration approach and the calibration results were verified with a photon diffusion theory system simulation. Using the empirical and simulated calibration results, the system was used to calculate either $S_{pa}O_2$ or $S_{pv}O_2$. The calculated results were validated with reference SO_2 values measured by means of a co-oximetry system.

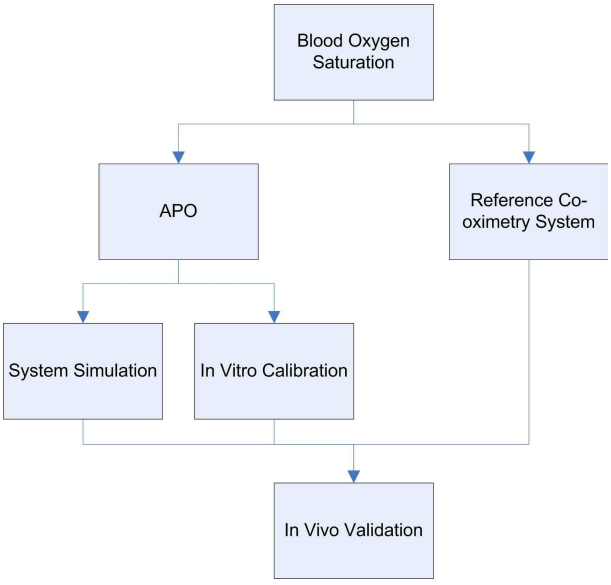

Figure 5.1: System Development Overview

5.1 System Simulation

As mentioned in Section 4.2, a system simulation was conducted to verify and provide information on calibration curve behaviour subjected to various physiological scenarios which could not necessarily be investigated using an *in vitro* or *in vivo* experimental setup. In this study, the propagation properties of light through human tissue was modeled using photon diffusion theory.

Using the approach followed by Schmitt (1991), a mathematical relationship between R and S_aO_2 for conventional pulse oximetry was derived as Equation 4.5. This relationship was modified to include the effects of venous pulsatile behaviour, as seen in Equation 4.25. These relationships could then be used to calculate the theoretical calibration curves for specified sensors utilizing LEDs at specific wavelengths. Calibration curves for the 660/910 nm and 740/880 nm sensors are depicted in Figures 5.2 and 5.3. The optical constants that was used as input to these models can be found in Table 4.3. The theoretical calibration curves could be used to calculate S_pO_2 from the value of R calculated from a normal physiological PPG. A more detailed discussion of this application will be provided in Section 5.3.

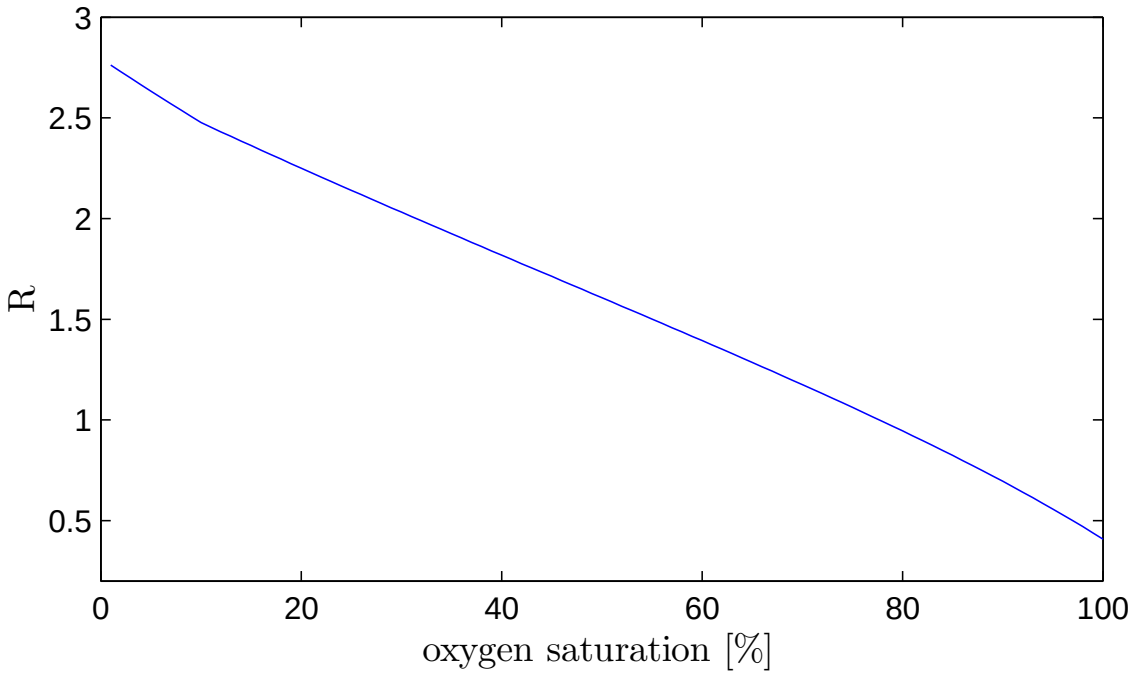

Figure 5.2: Simulated 660/910 nm Calibration Curve (H=45%; V_a=V_v=5%; d=10 mm; F=0.013; Arterio-Venous ΔSO_2=10%)

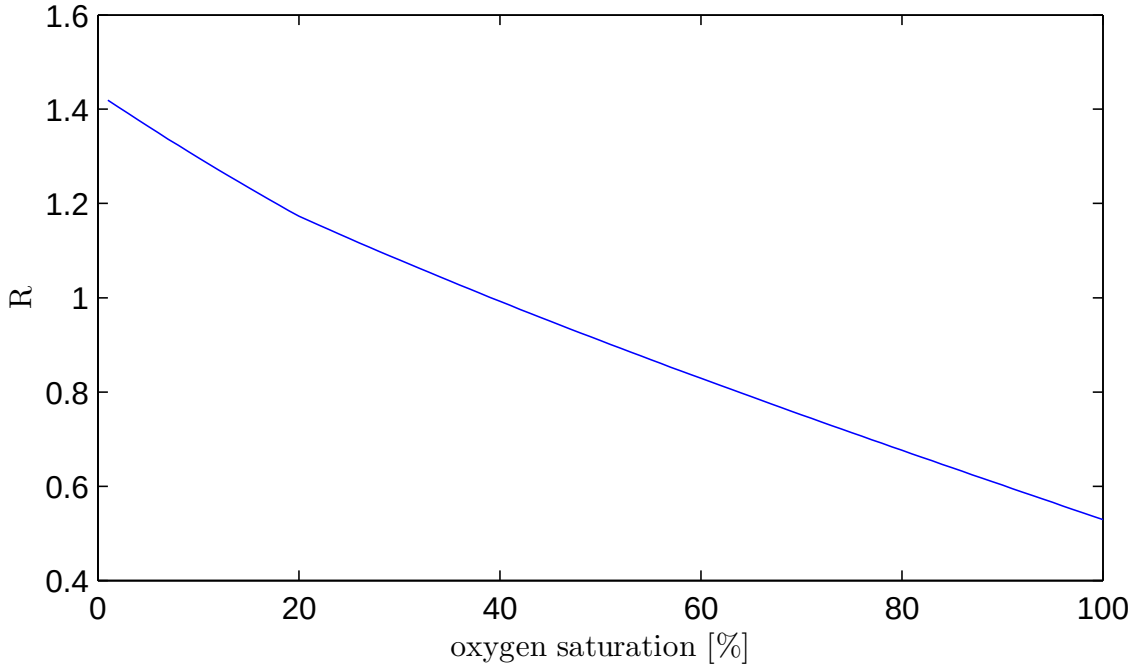

Figure 5.3: Simulated 740/880 nm Calibration Curve (H=45%; V_a=V_v=5%; d=10 mm; F=0.013; Arterio-Venous ΔSO_2=10%)

As can be seen from Figures 5.2 and 5.3, the 660/910 nm sensor is more sensitive to changes in S_aO_2 than the 740/880 nm sensor. This behaviour is due to the selection of wavelengths to maximise the quantities $(\sigma_{ab,ir}^{0\%} - \sigma_{ab,ir}^{100\%})$ and $(\sigma_{ab,r}^{100\%} - \sigma_{ab,r}^{0\%})$ in Equation 4.5, as noted by Schmitt (1991). This is the approach normally followed by pulse oximeter manufacturers to optimise sensor performance.

The system simulation was valuable in the sense that it could provide information on the behaviour of the calibration curves when subjected to changes in physiological variables, such as hematocrit, blood volume, finger thickness and arterio-venous saturation difference. Changes in the order of natural variation, have been studied and recorded by Schmitt (1991). Examples of curve behaviour subjected to changes in blood volume and hematocrit are shown in Figures 5.4 and 5.5.

As can be seen from Figures 5.4 and 5.5, variations in physiological parameters only have a notable effect on the calibration curve when saturation values decrease to less than 70-80%. It is well known in the medical community that conventional pulse oximeter functionality is questionable in the low saturation range, a fact

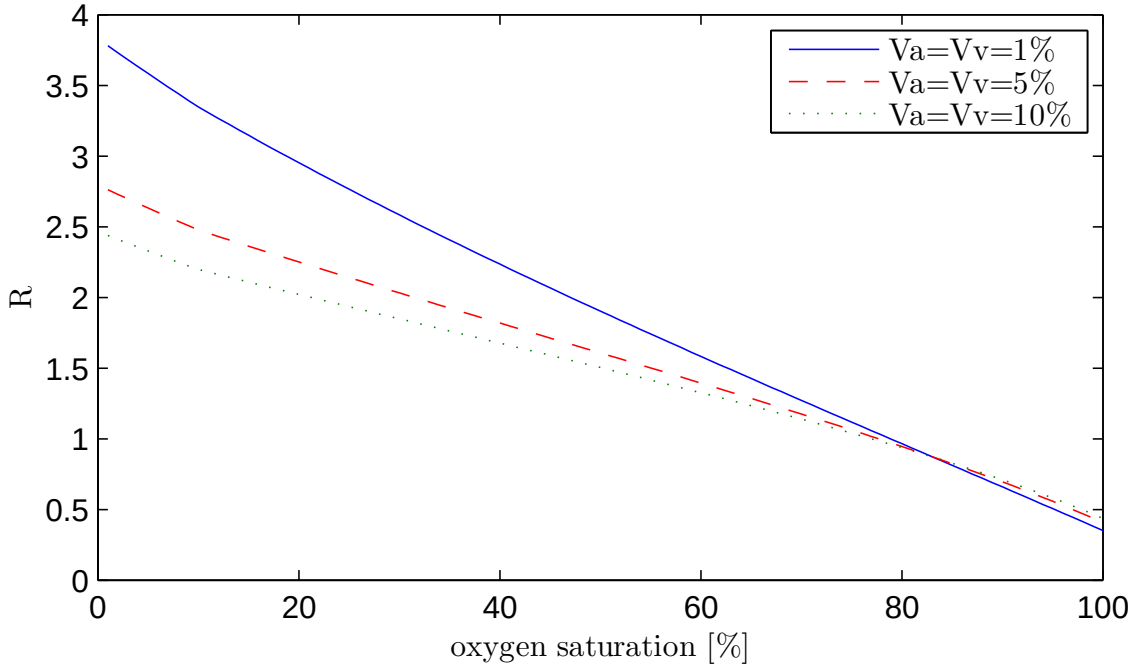

Figure 5.4: Simulated Blood Volume Variation in 660/910 nm Calibration Curve (H=45%; d=10 mm; F=0.013; Arterio-Venous ΔSO_2=10%)

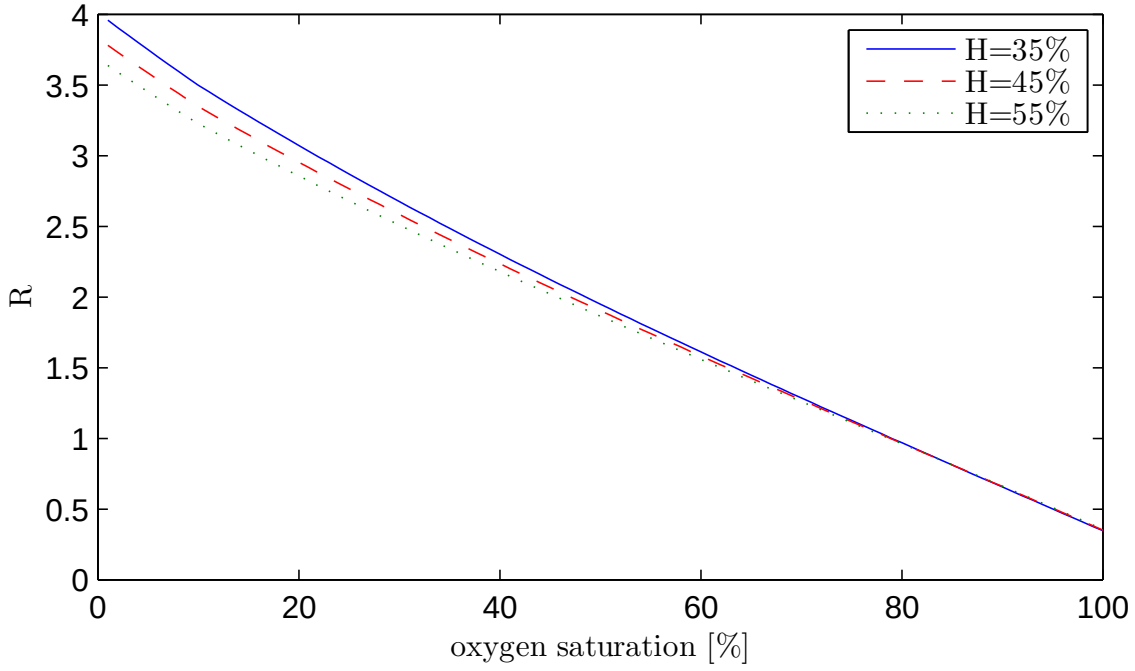

Figure 5.5: Simulated Hematocrit Variation in 660/910 nm Calibration Curve (d=10 mm; F=0.013; V_a=V_v=1%; Arterio-Venous ΔSO_2=10%)

that has been experimentally verified in studies done by Severinghaus and Naifeh (1987) and Severinghaus *et al.* (1989). This inaccuracy is probably due to the fact that most manufacturers utilize a high saturation *in vivo* calibration procedure and extrapolates this calibration data into the lower saturation range (Stabile and Reynolds, 2002), neglecting the effects of physiological variations as shown above.

As mentioned earlier, a mathematical relationship between R, S_aO_2 and S_vO_2 was developed to simulate calibration curves for arterial and venous pulsatile or arterio-venous behaviour. As can be seen from Equation 4.25, R is dependent on both S_aO_2 and S_vO_2, resulting in 10 000 (100x100) possible calibration curves for different combinations of S_aO_2 and S_vO_2 if the curves are based on a 1% resolution. If it is assumed that S_aO_2 is known, a calibration curve relating R and S_vO_2 could be calculated. These curves for the 660/910 nm sensor are plotted in Figure 5.6 for different values of S_aO_2.

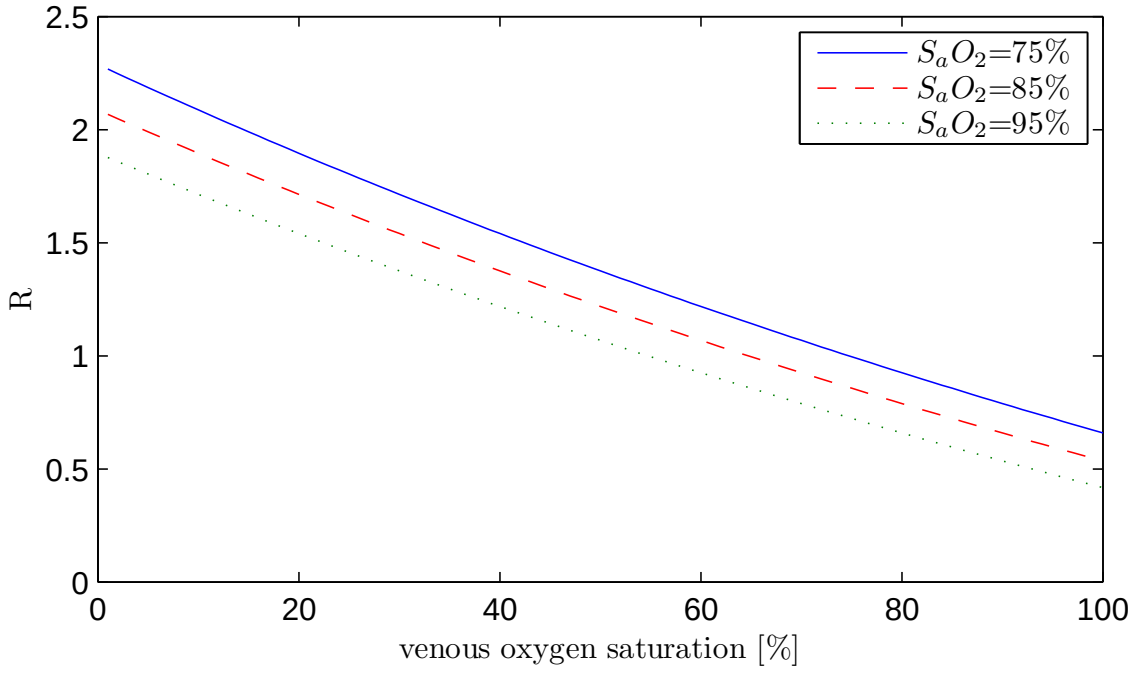

Figure 5.6: Simulated S_aO_2 Variation in 660/910 nm Calibration Curve (H=45%; d=10 mm; F=0.013; V_a=V_v=1%

The slope of the R/S_vO_2 calibration curve is dependent on the arterial-to-venous compliance ratio, as discussed in Section 4.2.2.C, while the overall y-coordinate placement of the curve is dependent on S_aO_2. An arterial-to-venous ratio of 1:2

would for example, deliver a calibration curve with a steeper slope than that of a arterial-to-venous ratio of 2:1. The dependency of y-coordinate placement on S_aO_2 can be seen in Figure 5.6.

5.2 System Calibration

A system calibration was conducted to obtain wavelength specific calibration curves. Based on an existing calibration method analysis done in Section 4.5.1, an *in vitro* calibration procedure, using a blood phantom, was used. Three sets of calibration runs were conducted during this phase of the system development. These were the calibration of the 660/910 nm sensor, the calibration of the 740/880 nm sensor and the *in vitro* arterio-venous validation.

During the calibration procedures for both the 660/910 nm and 740/880 nm sensors, only the the arterial sub circuit of the calibration setup, as outlined in Section 4.5.2, was used. Blood was firstly fully oxygenated and then deoxygenated in a stepwise manner, whilst collecting, storing and analyzing PPG data. Calibration curves for the 660/910 nm and 740/880 nm sensors, calculated using the approach outlined in Section 4.5.3, are plotted in Figures 5.7 and 5.8. The data collected for the curves were fitted with quadratic polynomials based on the curved behaviour of the simulation results presented in Figures 5.4 and 5.5. Commercial calibration curves, as presented by Nellcor Technical Staff (2004), Schmitt (1991) and Zonios *et al.* (2004) also exhibit this quadratic behaviour. In Figures 5.7 and 5.8 the different symbols represents different data sets and the lines the quadratic fits to these data sets.

The three different datasets presented for the 660/910 nm sensor calibration curves in Figure 5.7, resulted from an iterative procedure to perfect the calibration procedure. During the first calibration procedure, the excess saline was not drained from the venous reservoir of the Lilliput oxygenator, resulting in a very low hematocrit (H=13%) calibration curve. Only one unit of expired whole blood was available for this calibration run. For the second calibration run, the excess saline was drained from the oxygenator's venous reservoir, as explained in Section 4.5.3, but not from the circuit piping. This resulted in a higher, but still lower than normal, hematocrit (H=24%) calibration curve when the saline mixed with the single

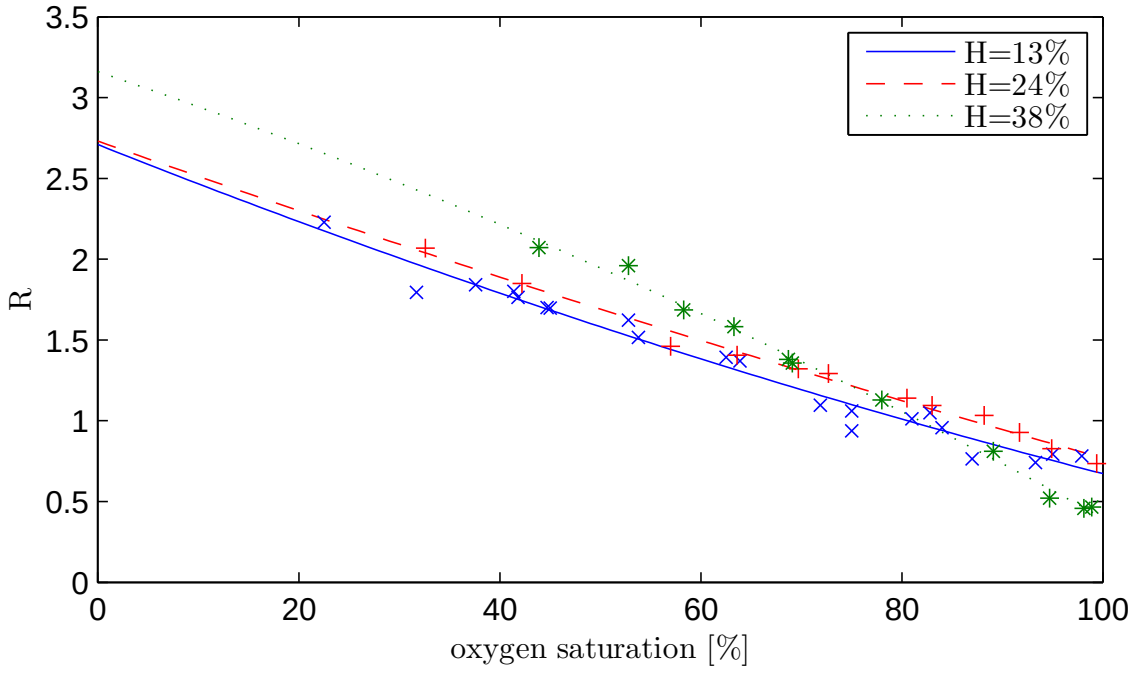

Figure 5.7: *In vitro* Empirical 660/910 nm Calibration Curve

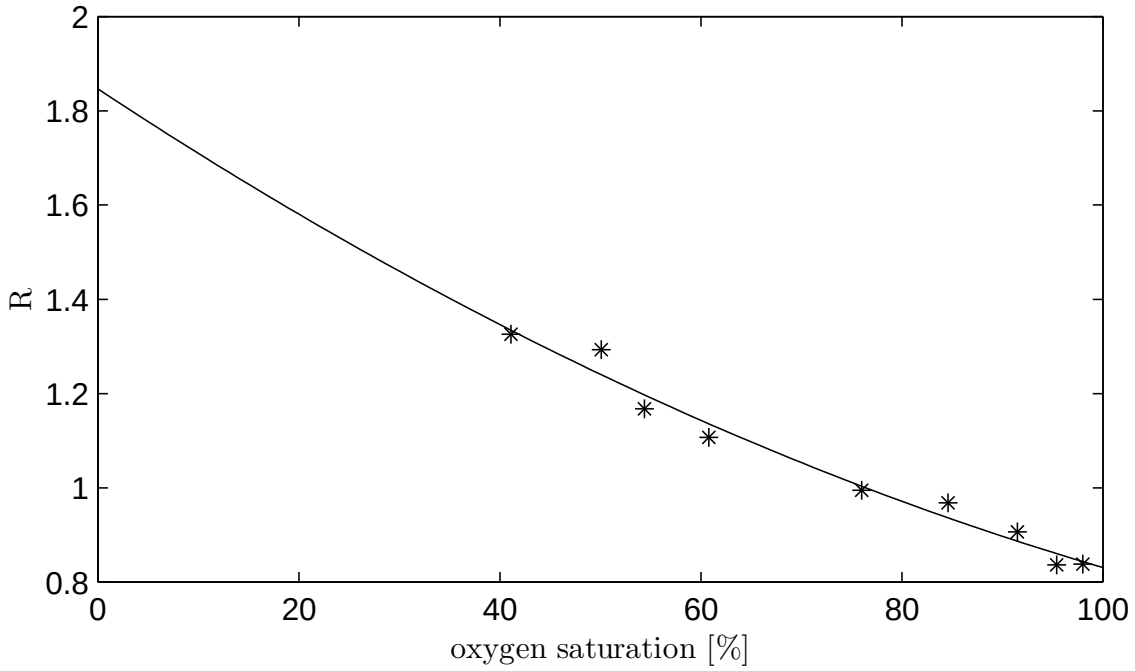

Figure 5.8: *In vitro* Empirical 740/880 nm Calibration Curve (H=38%)

Table 5.1: *In Vitro* Arterio-Venous Validation Results

Sensor	Trial #	Signal Quality[a]	R Stability[a]	$S_{pv}O_2$		Reference $S_{cv}O_2$
				Simulation[b]	Curve	
660/910 nm	1	+	0	82	89	83
660/910 nm	2	-	-	46	57	75
660/910 nm	3	+	-	29	41	71
660/910 nm	4	+	0	50	63	63
740/880 nm	1	+	0	1	1	83
740/880 nm	2	-	-	1	72	75
740/880 nm	3	+	+	22	100	71
740/880 nm	4	+	+	1	48	63

[a](+) Good; (0) Average; (-) Bad
[b]H=45%; d=10 mm; F=0.013; V_a=V_v=5%

available whole blood unit for this run. During the third calibration procedure, these issues were eliminated by first draining the excess saline from both the oxygenator's venous reservoir and the circuit piping before injecting the blood and by using two units of expired whole blood. This iterative procedure had the bonus of displaying in what manner hematocrit changes can affect empirical calibration curves.

As can be seen from Figures 5.7 and 5.8, the 660/910 nm sensor's calibration curve has a steeper slope than that of the 740/880 nm sensor, verifying the 660/910 nm sensor's superior sensitivity to changes in S_aO_2, as discussed in Section 5.1

Both the arterial and venous circuits in the calibration setup were used during the *in vitro* arterio-venous validation stage. The validation stage, as explained in Section 4.5.3, entailed calculating $S_{pv}O_2$ from an R value calculated by measuring arterial and venous pulsations. This calculation of $S_{pv}O_2$ was dependent on the prerequisite that the value of S_aO_2 was known. Two blood samples were withdrawn from the setup for each desaturation step and analyzed to obtain reference blood gas values for $S_{ca}O_2$ and $S_{cv}O_2$. Calculated $S_{pv}O_2$ and reference $S_{cv}O_2$ values can be seen in Table 5.1. PPG quality (shape and amplitude repeatability) and R stability (repeatability of R values calculated for different PPG peaks) is also indicated in Table 5.1.

As can be seen from Table 5.1, the calculated $S_{pv}O_2$ values were generally not in agreement with the reference $S_{cv}O_2$ values. Results were random and did

not present any repeatable behaviour. This is probably due to the complexity to set up the calibration experiment to accurately simulate physiological arterial-to-venous compliance ratios. Additionally, pressure pulse propagation discrepancies in the arterial and venous circuits would also deliver inaccurate results. The *in vitro* validation phase was not continued after the initial tests, as the amount of variables that could lead to inaccurate results were too many. The complete redesign of the calibration setup that would be needed to account for all these variables, was not considered a viable option. The validation of the arterio-venous hypothesis was shifted to an *in vivo* approach, as discussed in Section 5.3.4.

5.3 System Validation

The system validation phase entailed the *in vivo* evaluation of the accuracy of the simulated and empirical calibration curves presented in Sections 5.1 and 5.2 and the repeatability of the measurements. As mentioned in Section 4.6, the system validation phase had four objectives, namely, verifying the operation of the APG, evaluating curve performance under conventional high saturation value conditions, testing the validity of the arterio-venous hypothesis in conjunction with the AGP and evaluating APO curve performance in low saturation value scenarios.

5.3.1 APG Verification

The APG verification objective was simply a visual comparison of occluded PPG data before and after APG activation. PPG data for a subject before and after APG activation is shown in Figure 5.9. As can be seen, the APG has a pronounced effect on pulse amplitude and shape, enabling the effective extraction R which is a factor of arterial and venous pulsatile behaviour. The y-axis in Figure 5.9 is representative of arbitrary numbers allocated to the PPG during the A/D conversion of the detected light intensities.

5.3.2 High Saturation Validation

Only the 660/910 nm sensor's calibration curves were evaluated during the high saturation validation. This was due to the fact that the 660/910 nm sensor was

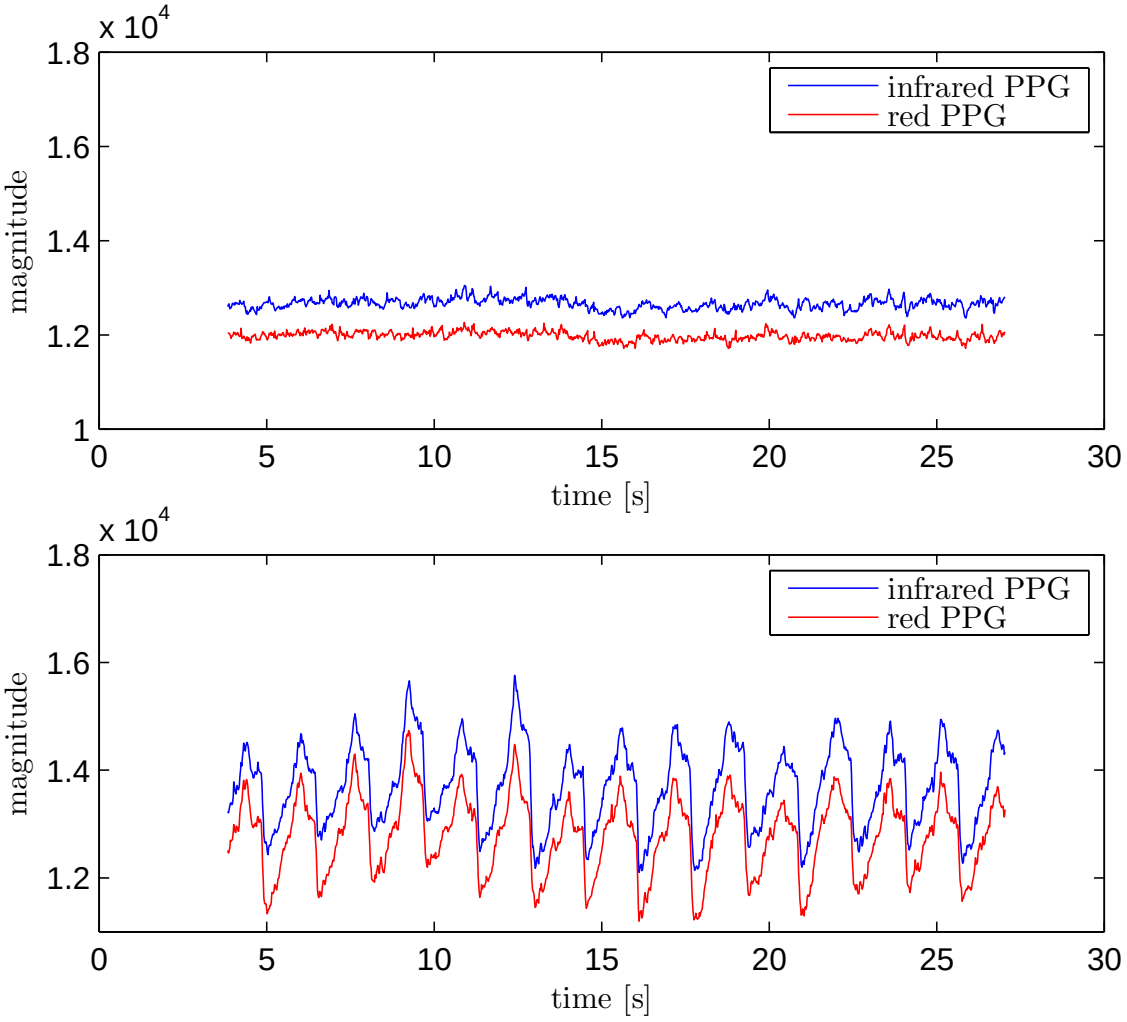

Figure 5.9: PPG on Occluded Tissue Before and After APG Application

specifically designed to perform optimally under high saturation conditions. The 740/880 nm sensor is not optimally suited for high saturation scenarios and was not used under these circumstances.

PPG and reference $S_{ca}O_2$ data were collected following the procedure described in Section 4.6.2. The PPG data were analyzed to extract an averaged R value, using the signal processing technique outlined in Section 4.4.2. These R values were used as input to the theoretical and empirical calibration curves of the 660/910 nm sensor to calculate $S_{pa}O_2$. The simulated curves used were calculated using the same approach followed to obtain the calibration curve presented in Figure 5.2, but with physiological parameters such as hematocrit and finger diameter individually

adapted for each volunteer. Calculated $S_{pa}O_2$ values were analyzed for accuracy and repeatability through comparison with the reference $S_{ca}O_2$ values. A comparative representation of the $S_{ca}O_2$ and $S_{pa}O_2$ values measured for twelve volunteers are depicted in Figures 5.10 and 5.11, whilst numerical $S_{ca}O_2$ and $S_{pa}O_2$ data can be found in Appendix D. Figure 5.10 presents saturation data calculated using the 660/910 nm sensor's empirical calibration curve, whilst Figure 5.11 presents the calculated results using the simulated calibration curve. Different symbols represent data collected from different volunteers.

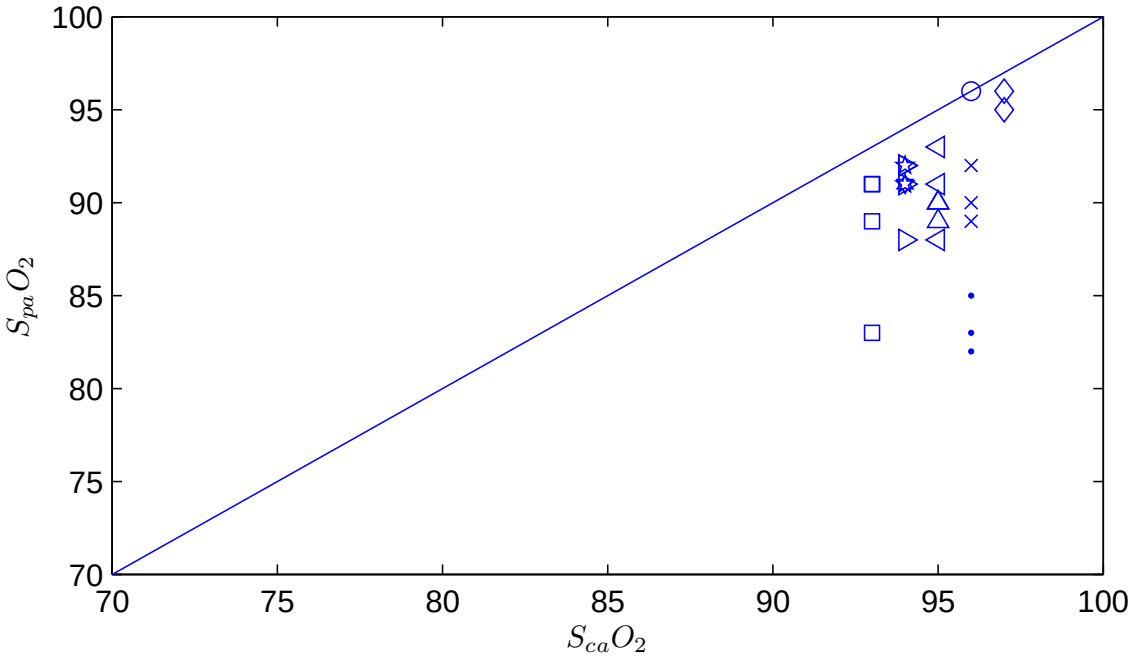

Figure 5.10: Empirical *In Vivo* High SO_2 Results (*In Vitro* Curve)

As can be seen from Figures 5.10 and 5.11, both the empirical and simulated calibration curves produce $S_{pa}O_2$ values that are situated beneath the diagonal line representing the reference $S_{ca}O_2$ values. This indicates a low indication error in both calibration curves, although it can be seen that the error for the empirical calibration curve is smaller than that of the simulated curve. $S_{pa}O_2$ bias and precision, as calculated using the approach described by Bland and Altman (1986), was -4.8±3.86% for the empirical calibration curve and -6.2±4.35% for the simulated calibration curve. The bias error in the empirical calibration curve is most likely due to the *in vitro* calibration approach that was followed, as opposed to

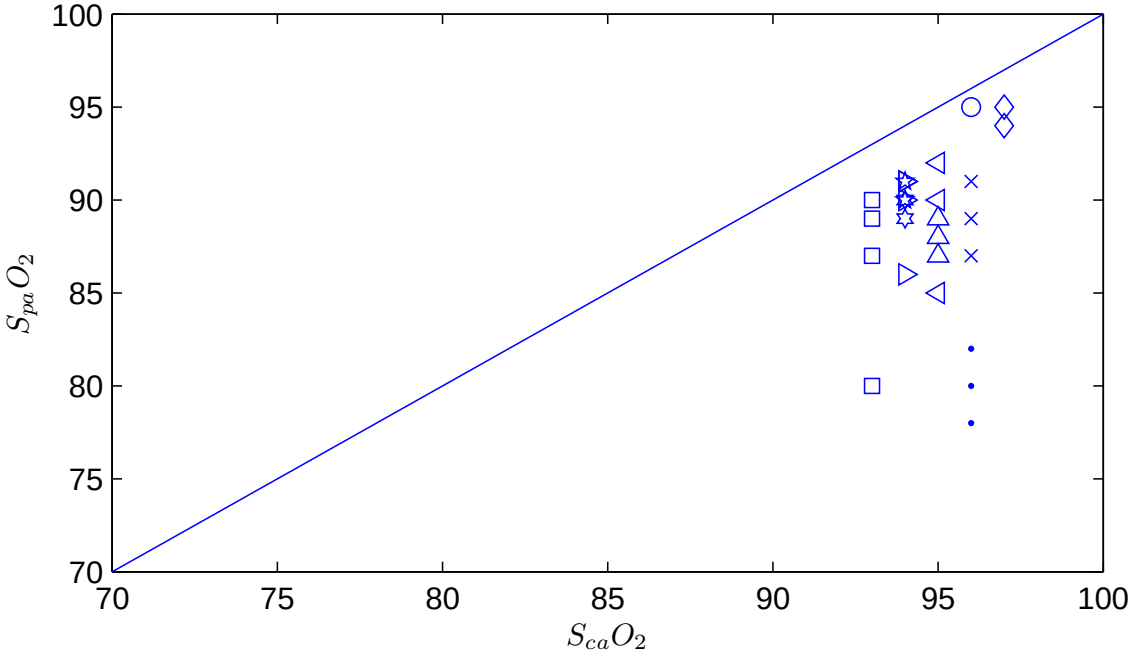

Figure 5.11: Empirical *In Vivo* High SO_2 Results (Simulated Curve)

the conventional *in vivo* calibration procedure as described in Section 4.5.1. The *in vitro* method is subject to inaccuracies resulting from the simulation of tissue properties by using a blood phantom, as opposed to the *in vivo* method, which is not. The bias error resulting from the use of the simulated curve is most likely due to small discrepancies between the physical process of light propagation through human tissue and the modelling of light propagation as a diffusive process.

Intra volunteer results show small variations in $S_{pa}O_2$ values, indicating good sensor repeatability. This good repeatability for the 660/910 nm sensor in high saturation scenarios is in good agreement with studies done by Mannheimer *et al.* (1997).

5.3.3 Low Saturation Validation

The low saturation validation was done to evaluate the accuracy and repeatability of low saturation $S_{pa}O_2$ measurements calculated using the empirical and simulated calibration curves, presented in Sections 5.1 and 5.2. The performance of both the 660/910 nm and 740/880 nm sensors were evaluated, despite the fact that the 660/910 nm sensor is not optimally suited for low saturation applications

(Mannheimer *et al.*, 1997).

In order to conduct the *in vivo* low saturation validation, low saturation conditions had to be induced in the tissue under consideration. This was done following a tissue occlusion procedure, as described in Section 4.6.2. Measurements were conducted after a period of occlusion, to allow overall saturation values in the tissue to decrease to a suitable level. It was assumed that S_aO_2 and S_vO_2 values would be similar after a sufficient period of time, and that a general S_gO_2 could be used for both. The APG was used to induce an artificial pulse in the occluded tissue.

Comparative representations of $S_{cg}O_2$ and $S_{pg}O_2$ values measured for twelve volunteers with the 660/910 nm and 740/880 nm sensors, is depicted in Figures 5.12 to 5.15, whilst numerical $S_{cg}O_2$ and $S_{pg}O_2$ data can be found in Appendix D.

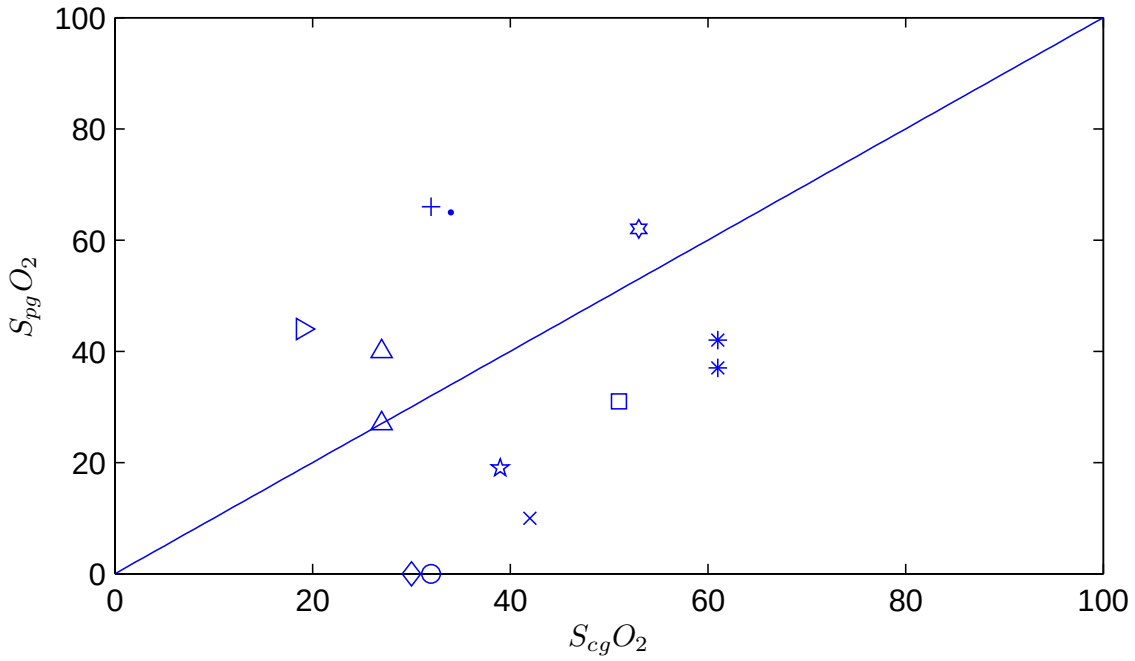

Figure 5.12: Empirical 660/910 nm *In Vivo* Low SO_2 Results (*In Vitro* Curve)

It is evident from Figures 5.12 and 5.13 that $S_{pg}O_2$ values calculated using the empirical and simulated calibration curves are neither accurate, nor repeatable. This is in good agreement with low saturation studies done by Severinghaus and Naifeh (1987), Severinghaus *et al.* (1989) and Mannheimer *et al.* (1997). Mannheimer *et al.* (1997) postulates that these accuracy and repeatability issues are as a result of a mismatch in mean photon path length changes at 660 nm and 910

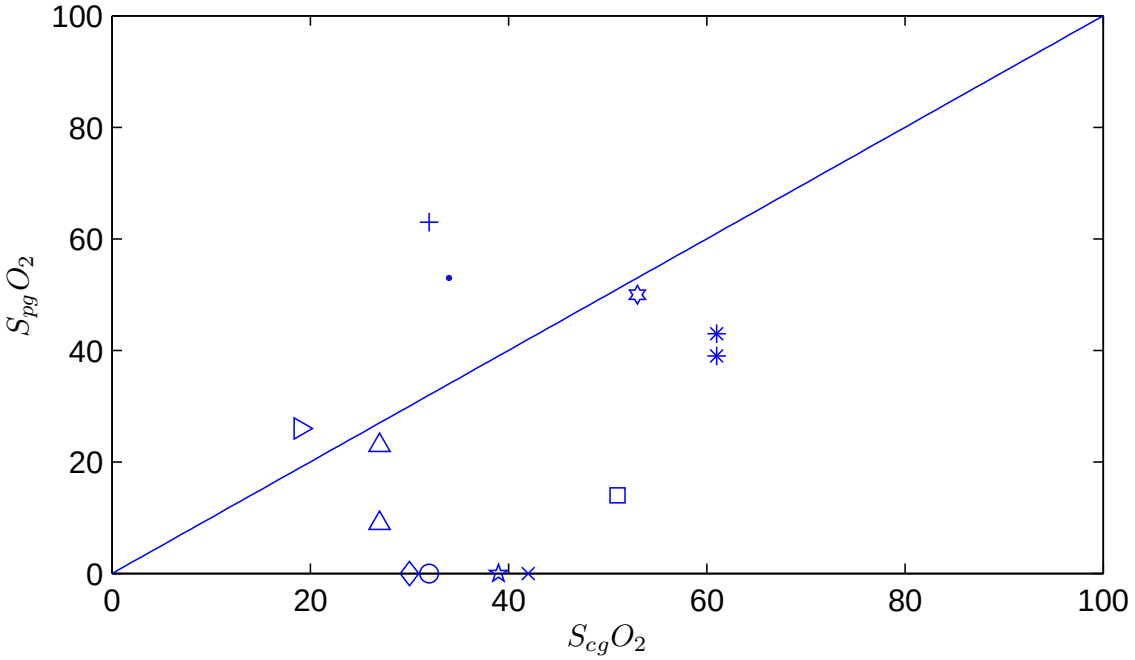

Figure 5.13: Empirical 660/910 nm *In Vivo* Low SO_2 Results (Simulated Curve)

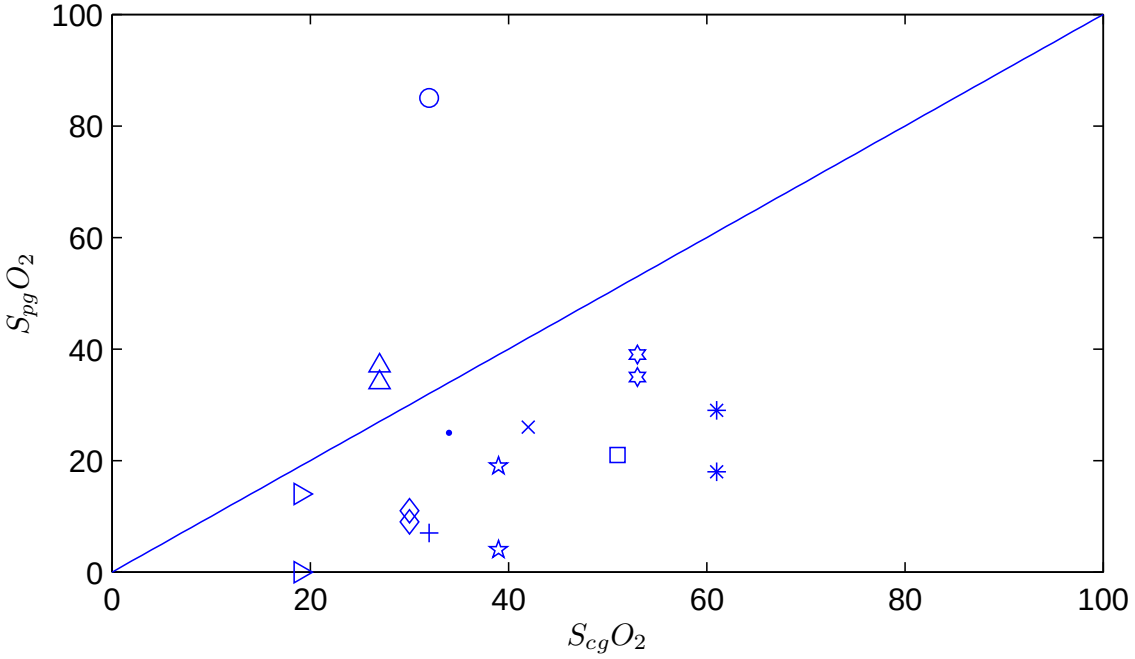

Figure 5.14: Empirical 740/880 nm *In Vivo* Low SO_2 Results (*In Vitro* Curve)

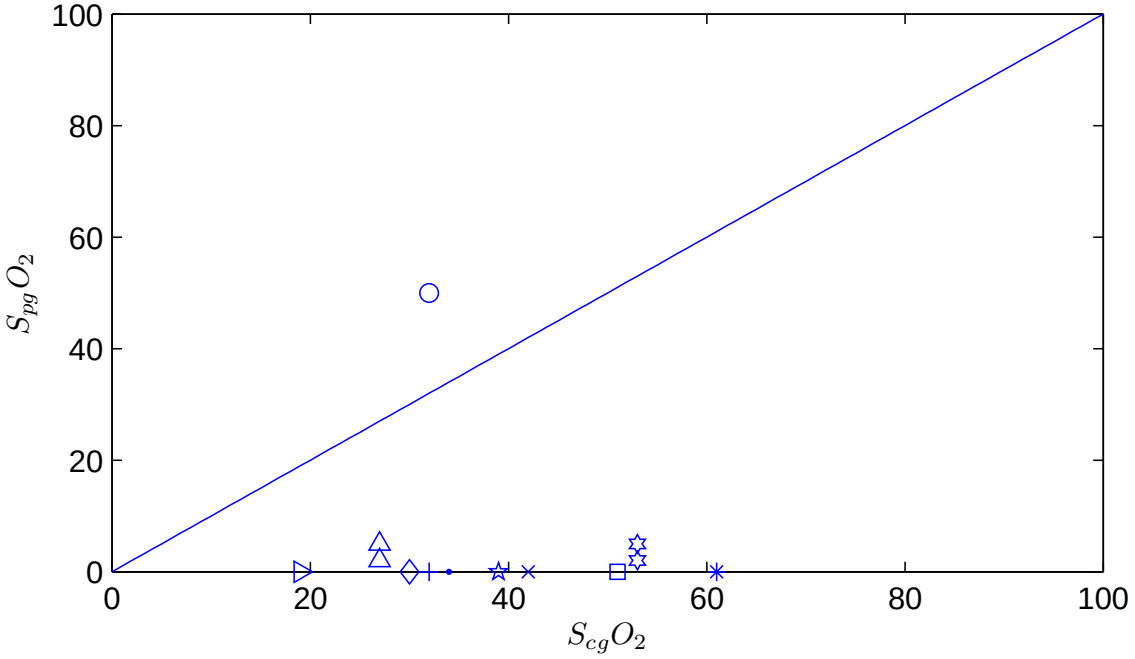

Figure 5.15: Empirical 740/880 nm *In Vivo* Low SO_2 Results (Simulated Curve)

nm. These photon path length changes are as a result of changes in physiological parameters between calibration and validation.

Inaccuracies in calculated $S_{pg}O_2$ values could also result from inaccurate calibration curves at low saturations. Due to the low repeatability of the $S_{pg}O_2$ values, it is difficult to formulate a conclusion on the curve accuracy, but if bias errors are considered, the empirical calibration curve presented in Figure 5.14 seems to be more accurate than the simulated calibration curve presented in Figure 5.15. The empirical and simulated bias and precision values were -5±24.75% and -14.5±23.07%, respectively.

Figures 5.14 and 5.15 show that $S_{pg}O_2$ values calculated using the 740/880 nm sensor show similar behaviour to those calculated using the 660/910 nm sensor. Figure 5.14 does however show much improved precision, taking into account that the 740/880 nm sensor has a less sensitive calibration curve compared to that of the 660/910 nm sensor. R values calculated from the 740/880 nm sensor's PPG would have had to be much more repeatable than R values from the 660/910 nm sensor's PPG, as small changes in R would result in large $S_{pg}O_2$ changes. Improved low saturation repeatability using the 740/880 nm sensor was verified by Mannheimer

et al. (1997).

If the bias errors of the 740/880 nm sensor's low saturation data are considered, it seems that the empirical calibration curve is again more accurate than the simulated calibration curve. The empirical and simulated bias and precision values were -13.6±21.38% and -34.4±18.4%, respectively. Studies done by Zonios *et al.* (2004) verified the empirical results by demonstrating that a traditional empirical calibration curve also delivered low $S_{pg}O_2$ values when compared to the reference $S_{cg}O_2$ values in the range of 20-60%.

5.3.4 Arterio-Venous Validation

The arterio-venous validation was done to determine the accuracy and validity of the hypothesis that the overall absorption by two volumes of blood with differing oxygen saturations would be a linear combination of the individual saturation values. Validation was done by comparing the accuracy and repeatability of $SpvO_2$ values calculated by means of empirical and simulated calibration curves, to reference $S_{cv}O_2$ values. Simulated arterio-venous calibration curves can be seen as Figure 5.6. Only the 660/910 nm sensor was tested during this phase, due to time constraints imposed by the testing procedure, as discussed in Section 4.6.2.

Arterio-venous validation, as explained in Section 4.6.2, was done by occluding the blood supply to the subject's left hand after withdrawing a reference $S_{ca}O_2$ blood sample. Artificial PPG data induced by the APG on the subject's finger was recorded and analyzed for $S_{pv}O_2$ using empirical and simulated calibration curves that have been modified to take the reference $S_{ca}O_2$ values into account. $S_{cv}O_2$ values obtained from a venous blood sample was used as reference. Comparative representations of $S_{cv}O_2$ and $S_{pv}O_2$ values measured for 12 subjects, is depicted in Figures 5.16 and 5.17. All results presented are for an arterial-to-venous compliance ratio of 1:1.

As can be seen from Figures 5.16 and 5.17, the calculated $S_{pv}O_2$ from both the empirical and simulated calibration curves are not very accurate nor repeatable. The empirical results do however show that for approximately 66% of the subjects, $S_{pv}O_2$ values were within 10% of the reference.

Bias and precision values for the empirical and simulated calibration curves, after the statistical outliers were removed, were 0.5±7.18% and -10.9±8.14%, re-

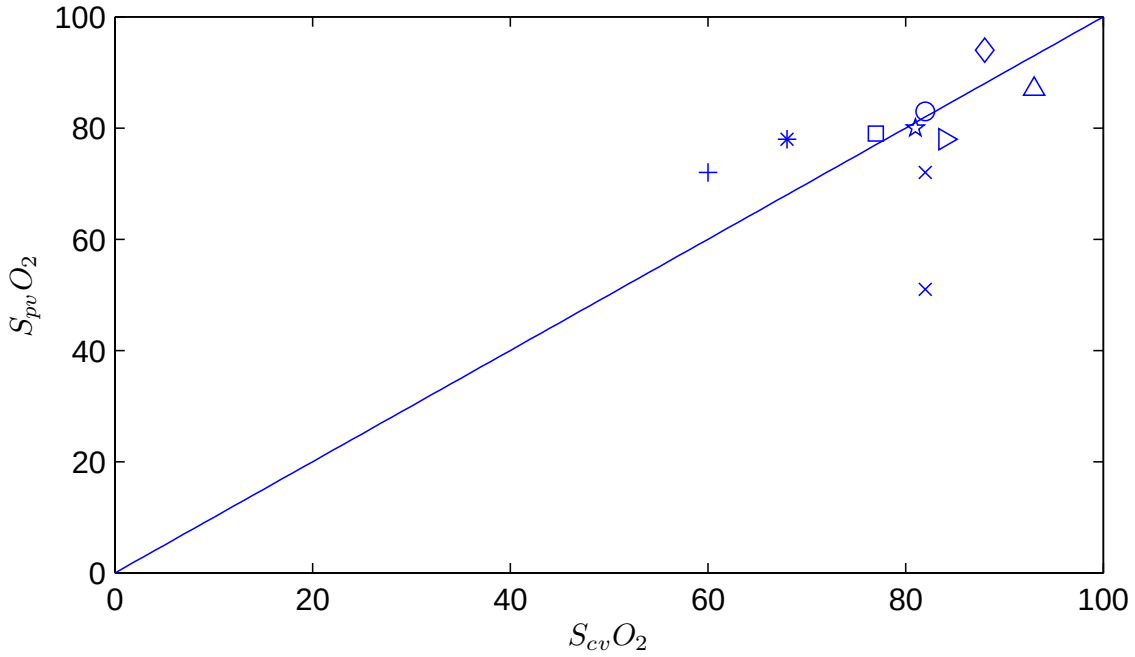

Figure 5.16: Empirical *In Vivo* Arterio-Venous Results (*In Vitro* Curve)

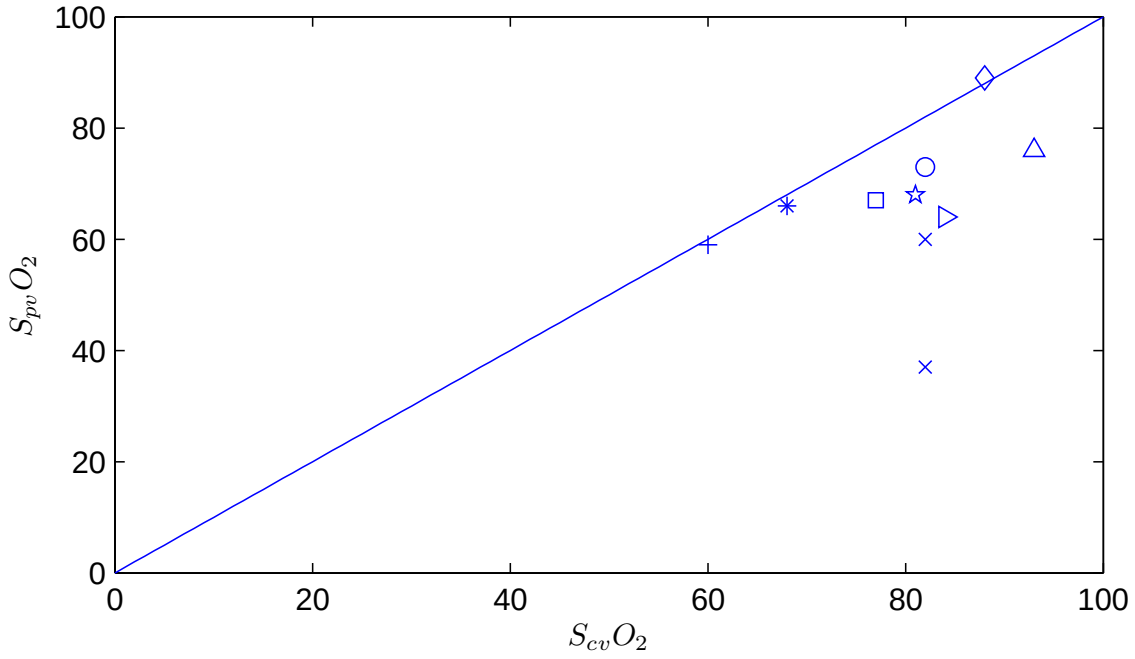

Figure 5.17: Empirical *In Vivo* Arterio-Venous Results (Simulated Curve)

spectively. Qualitatively, this indicates that the empirical calibration curve is more accurate than the simulated. As the arterio-venous calibration curves were directly derived from the arterial calibration curves presented in Figures 5.2 and 5.7, bias errors in these curves would also have propagated into the arterio-venous calibration curves.

The precision issues can most likely be attributed to discrepancies in arterial-to-venous ratios between different subjects, as well as PPG variants as a result of intrinsic APG behaviour which can be attributed to its design. These issues will be discussed in more detail in Section 5.4.

5.4 Discussion

In pulse oximetry, the accuracy of any S_pO_2 measurement is dependent on the accuracy of the pulse oximeter's calibration curve. This is the approach followed by most pulse oximter manufacturers and the reason behind using an *in vivo* calibration procedure. In the scope of this study however, this approach was not possible, with an *in vitro* approach being followed instead. This *in vitro* approach also has its drawbacks however, with the mismatch of optical properties, as explained by Mannheimer *et al.* (1997), being a major contributor. A photon diffusion simulation was conducted to investigate the effect that these property mismatches would have on calibration curves. Calibration curves for the *in vitro* calibration and simulation of the 660/910 nm and 740/880 nm sensors are shown in Figures 5.18 and 5.19. Figure 5.18 also shows the simulated calibration curves for subjects 3 and 7 based on physiological parameters.

As can be seen from Figure 5.18, the *in vitro* calibration curve and the simulation curve calculated by using the physiological properties of the *in vitro* calibration, are remarkably similar. In adapting the simulation for a finger diameter of 10 mm, the calculated curve did not deviate significantly in the saturation range 80-100%. The calibration curves presented by Schmitt (1991) also shows good correlation with *in vivo* commercial calibration curves. It can thus be concluded that the *in vitro* calibration curve is a relatively good substitute for an *in vivo* calibration curve in the high saturation range, verified by the accuracy and repeatability of the S_paO_2 results presented in Figure 5.10. It has to be noted however, that the bias in S_paO_2

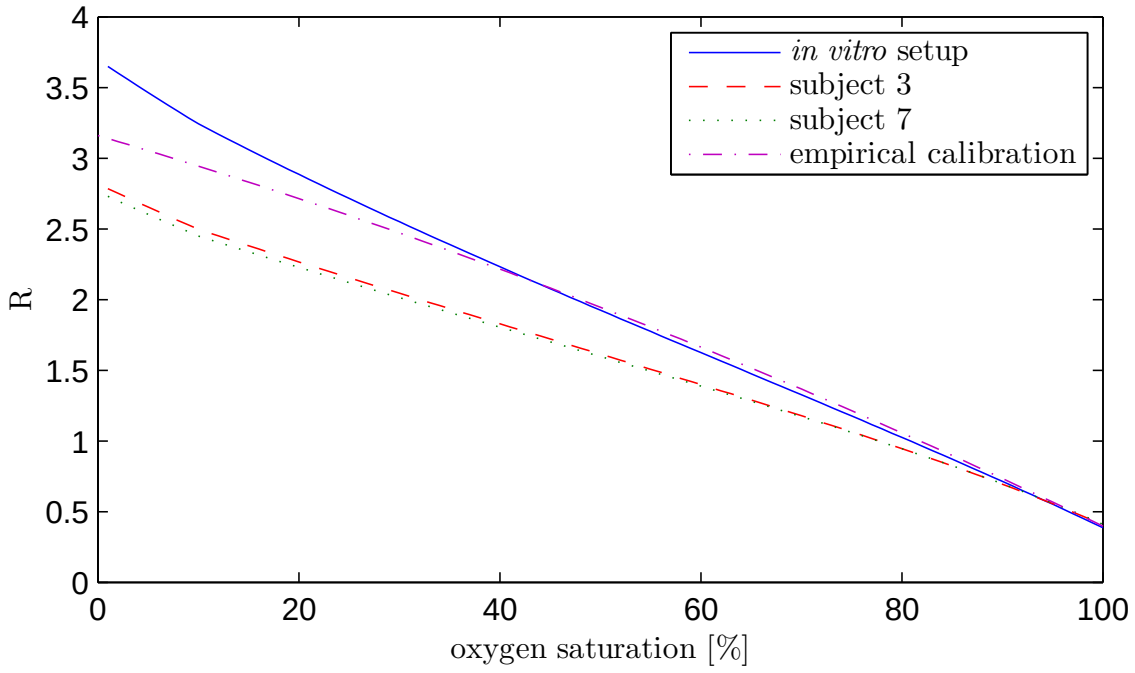

Figure 5.18: 660/910 nm Empirical and Simulated Calibration Curve Comparison

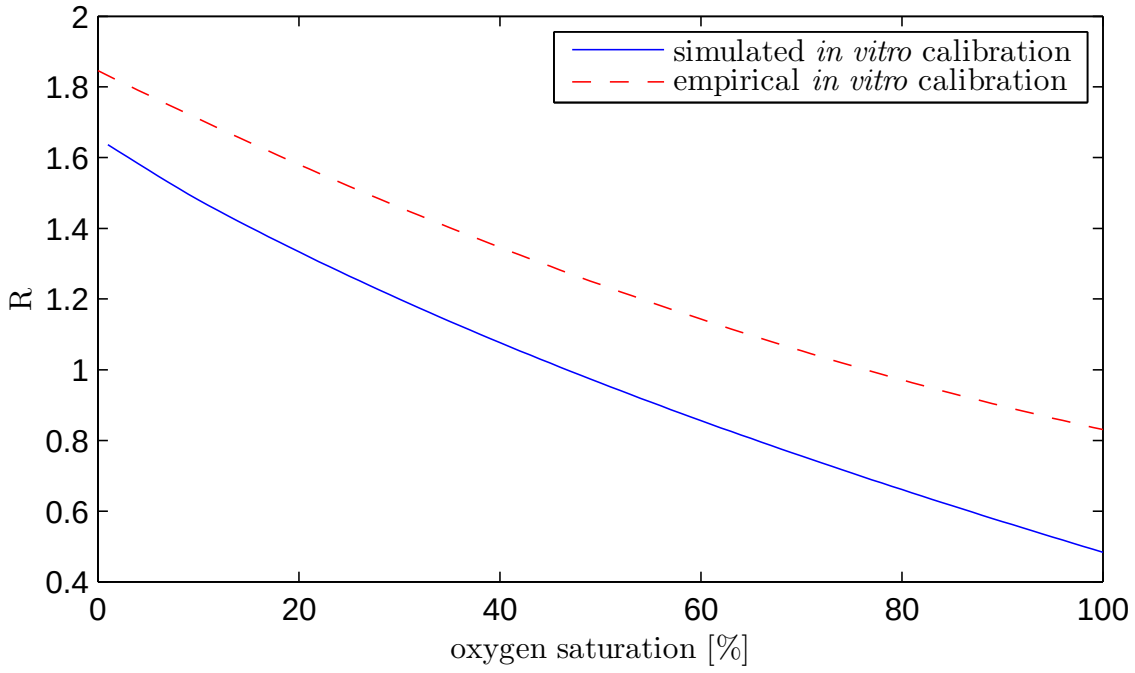

Figure 5.19: 740/880 nm Empirical and Simulated Calibration Curve Comparison

using the *in vitro* calibration curve is -4.8%, which is more than the ±1-2% for conventional *in vivo* curves. The errors in $S_{pa}O_2$ values presented in Figure 5.10 are most likely due to the use of a blood phantom to simulate optical transmission through tisue.

The empirical and simulated calibration curves obtained for the 740/880 nm sensor were not similar, as can be seen in Figure 5.19. The simulated calibration curve was however similar to results presented by Mannheimer *et al.* (1997). The constant DC offset between the curves, was most likely caused by hardware related issues such as the emitting intensity discrepancy between the selected 740 nm and 880 nm LEDs or LED emitting angle differences.

Figure 5.18 also displays the large deviations in calibration curves that variations in physiological parameters can cause at low saturations. The simulated curves presented were calculated by using subject specific physiological parameters measured during the *in vivo* validation phase. It was noted that these deviations were only noticeable in the saturation range 0-80%. This indicated that the *in vitro* calibration curves would not be accurate in the low saturation range, as the physiological parameter changes between the *in vitro* calibration and *in vivo* validation would have a pronounced effect on the calibration curve. The inaccuracy of the empirical and simulated calibration curves can be clearly seen in the results presented in Figures 5.12 to 5.15. Accuracy seemed to be best when using the empirical calibration curves for both the 660/910 nm and 740/880 nm sensors, indicating that photon diffusion theory, or alternatively the optical constants used, while being able to provide qualitative information on calibration curve behaviour, is most likely not an accurate representation of light propagation through human tissue in low saturation scenarios.

The accuracy and repeatability errors of the *in vivo* low saturation measurements could also have been affected by the operating principle of the pressure cuff. Even though the APG has been shown in Figure 5.9 to be effective in generating pulsatile blood behaviour in the finger, some design issues still exist. By fixing the cuff diameter by means of Velcro strips, no repeatable and sustainable method was available to ensure that each pneumatic pressure pulse would induce a repeatable blood pulse. If, for instance, the pressure cuff was fixed to fit more tightly around subject 1's finger than subject 2's finger, the pressure exerted on subject 1's finger would be greater than that exerted on subject 2's finger. Blood pulses in subject

1's finger would thus have a greater amplitude than in subject 2's finger. This effect was also noticeable during individual PPG data acquisition periods as the Velcro yielded under stress. It was thus not possible with the current design to ensure that all artificial blood pulses had similar pulse volumes, a factor that has a major effect in low saturation scenarios where physiological parameter variations have a major influence on sensor performance (Mannheimer *et al.*, 1997). Variations in a subject PPG and its effect on R can be seen in Figure 5.20

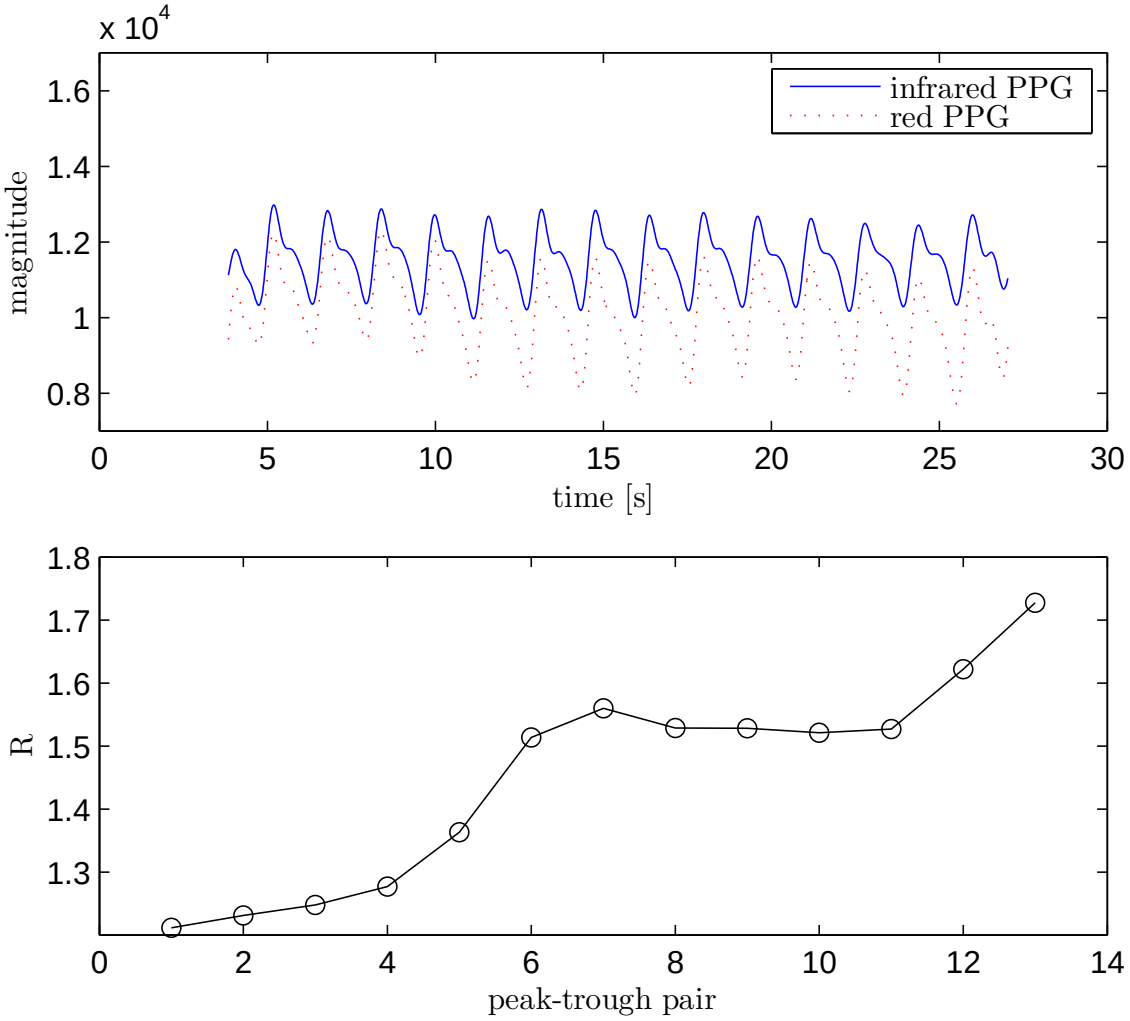

Figure 5.20: APG effect on R

When comparing low saturation results for the 660/910 nm and 740/880 nm sensors, it is evident that the 740/880 nm sensor has much improved repeatability

over the 660/910 nm sensor. This can be noted from Figure 5.14 where, even though the majority of the data points are lower than the reference, the data points are spaced closer together than the data points in Figure 5.12. Additionally, the lower sensitivity of the 740/880 nm sensor's calibration curve requires the R values to be spaced closer together to achieve the same saturation repeatability than that required for the 660/910 nm sensor.

The arterio-venous results, although not very repeatable, do seem to indicate that the measurement of $S_{pv}O_2$ is possible, taking into account that an arterial-to-venous compliance ratio of 1:1 was used as first approximation throughout the calculations.

Interestingly, it can be noted from Figure 5.16 that all ±1-2% calculations that are outside the range $S_{cv}O_2$±10% are much lower than the reference. This may be due to inaccurate calibration curves at the mid saturation range, inaccurate arterial-to-venous ratios or pneumatic pressure discrepancies caused by the pressure cuff design, as described above.

To demonstrate the effect of the arterial-to-venous compliance ratio, take the $S_{pv}O_2$ values measured for subject 2 as an example. The first $S_{pv}O_2$ value was calculated at 51% with a reference $S_{cv}O_2$ of 82%. If the arterial-to-venous ratio is changed from 1:1 to 1:5, the calculated $S_{pv}O_2$ value equals 70%. This is analogous to the novel arterio-venous hypothesis stated as Equation 4.1. With $S_{pv}O_2$ contributing to a larger extent to the $S_{pm}O_2$, the calculated $S_{pv}O_2$ is higher than with the original arterial-to-venous compliance ratio of 1:1. Similar improvements can be shown for all low $S_{pv}O_2$ values.

Pneumatic pressure discrepancies may also have a pronounced effect on $S_{pv}O_2$ measurements. In the arterio-venous hypothesis, it is assumed that the pressure exerted on the finger is higher than systolic pressure and that an artificial pulse is thus induced in both the arterial and venous circulation. This assumption is only valid if the pressure cuff's diameter is sufficiently small to ensure efficient pressure transmittance from the higher-than-systolic pneumatic pressure in the cuff to the finger. If the Velcro yields during data acquisition or the cuff is too loosely adjusted around the finger, the pressure transmitted to the finger may be insufficient to induce an artificial pulse in the arterial circulation. This would cause the 'combined arterial and venous R' to be representative of only venous pulsations. If a $S_{pa}O_2$ is used in conjunction with this venous R, the calculated $S_{pv}O_2$ would

be much lower than the reference $S_{cv}O_2$.

Chapter 6

Conclusion and Recommendations

6.1 Conclusion

The availability of continuous and non-invasive blood oxygen saturation information will provide surgeons and medical practitioners with a valuable tool in making intervention decisions regarding ischaemic tissue. In patients suffering from *meningococcemia*, this decision is vital as the spread of ischaemic conditions in peripheries is often rapid.

Pulse oximetry, the current benchmark for non-invasive measuring of S_aO_2, has limited application in these ischaemic tissues, due to low S_aO_2 values and low perfusion conditions. This study attempted to address these limitations by developing an artificial pulse oximeter capable of accurately measuring both S_aO_2 and S_vO_2 in low saturation and perfusion scenarios.

A 660/910 nm LED pair and a 740/880 nm LED pair sensor were designed to provide accuracy at both high and low saturations, respectively. The absence of an AC component in the PPG was addressed by incorporating an APG into the design to induce an artificial AC component. S_aO_2 and S_vO_2 were calculated according to an arterio-venous hypothesis dependent on arterial-to-venous compliance. The APO was calibrated for both high and low saturation ranges using an empirical *in vitro* calibration approach. APO validation was done by means of *in vivo* studies. A theoretical model, based on photon diffusion theory, was used to validate both calibration and validation results.

It can be concluded from this study that the *in vitro* calibration technique

followed is relatively accurate in high saturation scenarios, but that accuracy is still inferior to an *in vivo* calibration approach. The theoretical model showed close correlation with the 660/910 nm sensor's calibration curve at high saturation, indicating that photon diffusion theory is an accurate representation of light propagation in tissue at high saturation. Theoretical and empirical results did not agree for the 740/880 nm sensor, which is most likely due to inaccurate optical constants.

Results obtained for both the 660/910 nm and the 740/880 nm sensors showed bias and precision errors at low saturation. The 740/880 nm sensor did however show superior precision when compared to the 660/910 nm sensor at low saturation. It can thus be concluded that the 740/880 nm sensor is better suited for low saturation scenarios.

The validation of the arterio-venous hypothesis showed bias and precision errors for S_vO_2. When it is considered however, that these calculations were based upon an initial approximation of arterial-to-venous compliance, the results indicate that the APO is capable of measuring S_vO_2.

Although the results presented in this study are neither comprehensive nor entirely conclusive, it is the opinion of the author that the accurate determination of S_aO_2 and S_vO_2 with the APO would be possible with minor improvements to ensure a more standardized measurement method.

6.2 Recommendations

The simulation, calibration and validation results, presented in Chapter 5, indicate that accuracy and repeatability are problematic areas for the APO system, especially in low saturation scenarios. It is however the opinion of the author that certain improvements can be made to the hardware, the calibration and the validation procedure to improve the overall APO performance.

6.2.1 Hardware Recommendations

In the design of the 740/880 nm sensor, the LEDs as specified in Appendix A, was used. As can be seen from the datasheets in Appendix A, the ELS-740-994 LED has a specified radiant power of 6,5 mW at a forward current of 50 mA, while the ELS-880-894 LED has a specified radiant power of 12 mW at the same forward

current. Radiant intensity is also specified for the ELS-880-894 LED, but not the ELS-740-994 LED and is most likely not similar. These emittance discrepancies between the LEDs were probably the cause for the large discrepancies between the empirical and theoretical calibration curves presented in Figure 5.19. Even though the effects of differences in radiant power and intensity parameters would be present and eliminated during the calibration phase, it still results in an inaccurate theoretical explanation of curve behaviour and as such, only adds to calibration curve uncertainty. It is thus recommended that alternative 740 nm and 880 nm LEDs, with similar operating parameters, are used.

As explained in Section 5.4, the design of the pressure cuff might have affected the accuracy and repeatability of the APO system. The main issue was the inability to standardize the cuff diameter before and during PPG data acquisition. This resulted in differing pneumatic pressures being exerted on subjects, even though pneumatic pressure in the APG could be controlled. A complete redesign of the pressure cuff is recommended. An improved concept is shown in Figure 6.1.

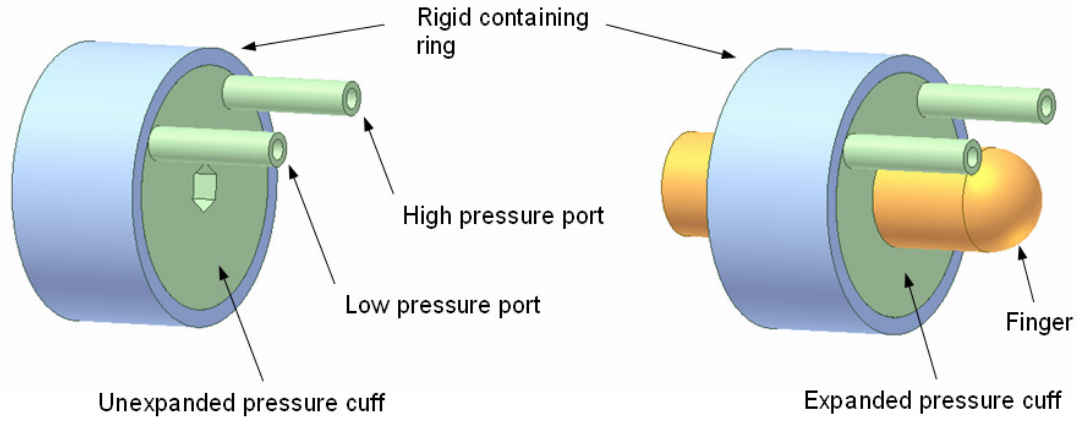

Figure 6.1: Improved Pressure Cuff Concept

In Figure 6.1, the pressure cuff consists of a rigid ring, a pressure cuff and high and low pressure ports. The containing ring is sufficiently large to accommodate fingers of varying diameters and serves to limit the outside diameter of the pressure cuff. The pressure cuff is situated on the inside of the containing ring and is large

enough to completely fill the space on the inside of the containing ring if fully inflated.

The deflated prototype is slid over the finger in the manner indicated in Figure 6.1. The pressure cuff is inflated to an initial and controllable pressure. This low starting pressure provides an accurate and repeatable starting condition. By designing the pressure cuff to be sufficiently large to fill the space on the inside of the containing ring, the pressure cuff will expand to adapt to the finger's diameter and efficiently transfer pressure pulses to the finger. The containing ring provides a rigid outside parameter to improve accuracy and repeatability during APG operation.

The high and low pressure ports are included to provide a complete APO system to measure $S_{pa}O_2$ and $S_{pv}O_2$ in normal perfusion and hypoperfusion scenarios. Low pressure pneumatic pulses, but at higher pressure than the starting pressure, are transmitted through the pressure cuff to measure $S_{pv}O_2$ with the 740/880 nm sensor. By ensuring that the pressure is lower than systolic blood pressure, the blood pulses will only be induced in the venous circulation, causing R to be dependent only on venous pulsations. $S_{pv}O_2$ can then be calculated by using a calibration curve that is accurate at low or mid range saturations. Higher than systolic pressure pulses are then transmitted through the pressure cuff to measure $S_{pa}O_2$ using the $S_{pv}O_2$ values calculated earlier, the arterio-venous hypothesis as stated in Section 4.6 and accurate arterial-to-venous compliance ratios. The 660/910 nm sensor will be used for this purpose. The combined arterial and venous R is analyzed for $S_{pa}O_2$ using a 660/910 nm arterio-venous calibration curve. Low and high pressure pulses are applied at frequencies that ensure minimal interference from normal systolic pulses.

Compressed air will be stored in two separate pressure vessels to provide the low and high pressure air. These pressure vessels will be large enough to ensure that the high air demand will not result in pronounced pressure drops in the system, while the compressor's air supply rate will be sufficient to meet the demand. The starting, low and high pressure within the system will be continuously monitored to ensure the correct operation of the system.

The modified system, as stated above, will only be suited for use on a digit. For use on a limb or part of the trunk, the design would have to be modified to enable effective pressure transfer to the tissue.

An alternative to the arterio-venous hypothesis presented in this study would be the five wavelength system proposed by Aoyagi (2003). The system as proposed by Aoyagi (2003) aims to eliminate or minimize the effect of motion artifacts on pulse oximeter performance. In doing so, the system possibly opens the way for the determination of $S_{pv}O_2$ without the need for the arterio-venous hypothesis and its accompanying compliance ratio uncertainties. As the five wavelength system is dependent on arterial and venous pulsations, the system should still be used in conjunction with the APG. The dual-wavelength sensor would then be replaced with a five wavelength alternative.

6.2.2 Calibration Recommendations

The *in vitro* calibration curves presented in Figures 5.7 delivered high saturation values that were relatively repeatable when compared to the reference, as shown in Figure 5.10. Accuracy was, however, not good when compared to commercial pulse oximeters that exhibit much lower errors (Zonios *et al.*, 2004). Commercial pulse oximeter calibration curves are obtained by utilizing an *in vivo* calibration procedure. It is thus recommended that the 660/910 nm sensor is calibrated for high saturation using an *in vivo* calibration approach.

For low saturation scenarios, the *in vitro* calibration setup discussed in Section 4.5.2 can be modified to minimize the pronounced effect that physiological parameter variations have on curve behaviour at low saturations. The *in vitro* setup can be modified so the experimental parameters closely resembles physiological parameters. The *cuvette* depth could, for instance, be increased to 10 mm to more accurately resemble actual physiological finger diameter data. Hematocrit could also be closely controlled around the normal 45% value. Resident blood volume in the *cuvette* could be controlled by pressurizing the milk chamber. A higher milk pressure will ensure a lower blood volume and vice versa. Milk pressure would have to be closely monitored and controlled to deliver repeatable results. Additional procedures that reduce pressure and flow velocity related artifacts could also be included in the calibration setup (Edrich *et al.*, 2000).

A factor that could also contribute to *in vitro* calibration curve inaccuracy, is RBC haemolysis. It was noted that lactate levels in the blood used during the calibration runs, rose to high levels at the completion of the runs. Increased lactate

levels are a good indication of RBC haemolysis. Haemolysis would have the effect of altering the scattering coefficient the blood, modifying the light propagation properties of the blood. It is thus recommended that only whole blood that has normal lactate levels is used during the calibration phase.

Alternatively, the occlusion studies done as part of the *in vivo* validation phase, as explained in Section 4.6.2, can be used to obtain a low saturation *in vivo* calibration curve. A factor to watch out for would be the volume of the artificial blood volume pulse. The APG generates a pulse in both the arterial and venous circulations, approximately doubling the blood volume pulse. This could have a major effect on the calibration curve. Another issue could be discrepancies between S_aO_2 and S_vO_2 after the occlusion period has passed. If S_aO_2 and S_vO_2 values are not very similar when the PPG data is collected, the calibration curve will not be accurate at low saturations due to the fact the both saturations have an effect on the calculated R.

6.2.3 Validation Recommendations

As noted in Section 6.2.2, differences in S_aO_2 and S_vO_2 values during the *in vivo* low saturation validation phase could have a major effect on R values. This effect is due the the fact that R is dependent on both S_aO_2 and S_vO_2. Alternative validation studies, such as the *in vivo* studies done on sheep by Zonios *et al.* (2004), should be considered.

List of References

Aoyagi, T. (1994). Apparatus for calibrating pulse oximeters world patent. USP5278627.

Aoyagi, T. (2003). Pulse oximetry: Its invention, theory, and future. *Journal of Anesthesia*, vol. 17, pp. 259–266.

Bickler, P.E., Feiner, J.R. and Severinghaus, J.W. (2005). Effects of skin pigmentation on pulse oximeter accuracy at low saturation. *Anesthesiology*, vol. 102, pp. 715–719.

Billauer, E. (2007). Peak detection.
Available at: `www.billauer.co.il/peakdet.html`

Bland, J.M. and Altman, D.G. (1986). Statistical method for assessing agreement between two methods of clinical measurement. *The Lancet*, pp. 307–310.

Carter, B.G., Carlin, J.B., Tibballs, J., Mead, H., Hochmann, M. and Osborne, A. (1998). Accuracy of two pulse oximeters at low arterial hemoglobin-oxygen saturation. *Critical Care Medicine*, vol. 26, pp. 1128–33.

Casciani, J.R., Mannheimer, P.D., Nierlich, S.L. and Ruskewicz, S.J. (1995). Pulse oximeter sensor optimized for low saturation. PCT/US1995/004050.

Chan, D., Smith, P.R., Caine, M.P., Spyt, T., Boehm, M. and Machin, D. (2003). Preliminary clinical investigations of a new noninvasive venous pulse oximeter. *Novel Optical Instrumentation for Biomedical Applications*, vol. 5143, pp. 232–239.

Chan, H.D. and Smith, P.R. (2003). Venous pulse oximetry world patent. USP7263395.

Clinical Dynamics Corporation (1996). Smartsat pulse oximetry analyzer operation manual.

Coetzee, F.M. and Elghazzawi, Z. (2000). Noise-resistant pulse oximetry using a synthetic reference signal. *IEEE Transactions on Biomedical Engineering*, vol. 47, pp. 1018–26.

Cooke, J. (2000). When pulse oximeters fail motion and low perfusion. *American Society of Anesthesiologists*, vol. A-554.

Cooke, J. (2002). Tolerance of portable pulse oximeters to motion and low perfusion. Available at: `http://www.anestech.org/media/Publications/Annual_2002/`

de Kock, J.P. and Tarassenko, L. (1991). In vitro investigation of the factors affecting pulse oximetry. *Journal of Biomedical Engineering*, vol. 13, pp. 61–6.

de Kock, J.P. and Tarassenko, L. (1993). Pulse oximetry: Theoretical and experimental models. *Medical and Biological Engineering and Computing*, vol. 31, pp. 291–300.

Dippenaar, R., Smith, J., Goussard, P. and Walters, E. (2006). Meningococcal purpura fulminans treated with medicinal leeches. *Pediatric Critical Care Medicine*, vol. 7, pp. 476–478.

Echiadis, A.S., Crabtree, V.P., Bence, J., Hadjinikolaou, L., Alexiou, C., Spyt, T.J. and Hu, S. (2007). Non-invasive measurement of peripheral venous oxygen saturation using a new venous oximetry method: Evaluation during bypass in heart surgery. *Physiological Measurement*, vol. 28, pp. 897–911.

Edrich, T., Flaig, M., Knitza, R. and Rall, G. (2000). Pulse oximetry: An improved in vitro model that reduces blood flow-related artifacts. *IEEE Transactions on Biomedical Engineering*, vol. 47, pp. 338–343.

Edrich, T., Knitza, R. and Rall, G. (1998). Can the blood content of the tissues be determined optically during pulse oximetry without knowledge of the oxygen saturation? *Engineering in Medicine and Biology Society*, vol. 6, pp. 3072–3075.

Elwell, C. and Hebden, J. (1999). Near-infrared spectroscopy. Available at: `http://www.medphys.ucl.ac.uk/research/borg/research/`

Enderle, J.D., Blanchard, S.M. and Bronzino, J.D. (2005). *Introduction to Biomedical Engineering*. Elsevier Academic Press.

Faber, D.J., Aalders, M.C.G., Mik, E.G., Hooper, B.A., van Gemert, M.J.C. and van Leeuwen, A.G.J.M. (2004). Oxygen saturation-dependent absorption and scattering of blood.

Fairchild Semiconductor Technical Communications (2005). LM317 3-terminal positive adjustable regulator.

Festo Technical Communications (2004). Festo solenoid coils MSF/MSN1.

Foo, J.Y. and Wilson, S.J. (2006). A computational system to optimise noise rejection in photoplethysmography signals during motion or poor perfusion states. *Medical and Biological Engineering and Computing*, vol. 44, pp. 140–145.

Friebel, M. and Meinke, M. (2006). Model function to calculate the refractive index of native hemoglobin in the wavelength range of 250-1100 nm dependent on concentration. *Applied Optics.*, vol. 45, pp. 2838–2842.

Gonchukov, S.A., Lazarev, Y.B. and Podkolzin, A.A. (2000). Laser refractometry of biological fluids. *Instruments and Experimental Techniques*, vol. 43, pp. 826–828.

Graybeal, J. and Petterson, M. (2004). Adaptive filtering and alternative calculations revolutionizes pulse oximetry sensitivity and specificity during motion and low perfusion. *Engineering in Medicine and Biology Society*, vol. 2, pp. 5363–5366.

Hammer, M., Schweitzer, D., Michel, B., Thamm, E. and Kolb, A. (1998). Single scattering by red blood cells. *Applied Optics*, vol. 7, pp. 7410–7418.

Hiraoka, M., Firbank, M., Essenpreis, M., Cope, M., Arridge, S.R., van der Zee, P. and Delpy, D.T. (1993). A Monte Carlo investigation of optical pathlength in inhomogeneous tissue and its application to near-infrared spectroscopy. *Physics in Medicine and Biology*, vol. 38, pp. 1859–1876.

Hornberger, C., Knoop, P., Matz, H., Dörries, F., Konecny, E., Gehring, H., Otten, J., Bonk, R., Frankenberger, H., Wouters, P., Gil-Rodriguez, J., Ponz, L., Avgerinos, J., Karoutis, A., Ikiades, A. and Weininger, S. (2002). A prototype device for standardized calibration of pulse oximeters ii. *Journal of Clinical Monitoring and Computing*, vol. 17, pp. 203–209.

Hummler, D.H., Engelmann, A., Pohlandt, F., Högel, J. and Franz, A.R. (2004). Accuracy of pulse oximetry readings in an animal model of low perfusion caused by emerging pneumonia and sepsis. *Intensive Care Medicine*, vol. 30, pp. 709–713.

Hummler, D.H., Engelmann, A., Pohlandt, F., Högel, J. and Franz, A.R. (2006). Decreased accuracy of pulse oximetry measurements during low perfusion caused by sepsis: Is the perfusion index of any value? *Intensive Care Medicine*, vol. 32, pp. 1428–1431.

Jacques, S.L. (1998). Skin optics summary. Oregon Medical Laser Centre News. Available at: `http://omlc.ogi.edu/news/jan98/skinoptics.html`

Jagomagi, K., Raamat, R., Talts, J., Ragun, U., Lansimies, E. and Jurvelin, J. (2005). Recording of dynamic arterial compliance changes during hand elevation. *Clinical Physiology and Functional Imaging*, vol. 25, pp. 350–356.

Jensen, L.A., Onyskiw, J.E. and Prasad, N.G. (1998). Meta-analysis of arterial oxygen saturation monitoring by pulse oximetry in adults. *Heart and Lung : The Journal of Critical Care*, vol. 27, pp. 387–408.

Jones, B. (1998). A reappraisal of the use of infrared thermal image analysis in medicine. *IEEE Transactions on Medical Imaging*, vol. 17, pp. 1019–1027.

Jones, B. and Plassmann, P. (2002). Digital infrared thermal imaging of human skin. *IEEE Engineering in Medicine and Biology Magazine*, vol. 21, pp. 41–48.

Jorgensen, J., Schmid, E., König, V., Faisst, K., Huch, A. and Huch, R. (1995). Limitations of forehead pulse oximetry. *Journal of Clinical Monitoring and Computing*, vol. 11, pp. 253–256.

Jubran, A. (2004). Pulse oximetry. *Intensive Care Medicine*, vol. 30, pp. 2017–2020.

Kamat, V. (2002). Pulse oximetry. *Indian Journal of Anaesthesia*, vol. 46, pp. 261–268.

Kandel, G. and Aberman, A. (1983). Mixed venous oxygen saturation: Its role in the assessment of the critically ill patient. *Archives of Internal Medicine*, vol. 143, pp. 1400–1402.

Kawarada, A., Shimazu, H., Ito, H. and Yamakoshi, K. (1988). Noninvasive measurement of arterial elasticity in various human limbs. *Medical and Biological Engineering and Computing*, vol. 26, pp. 641–646.

Kelleher, J.F. (1988). Pulse oximetry. *Journal of Clinical Monitoring and Computing*, vol. 5, pp. 37–62.

Krenz, G.S. and Dawson, C.A. (2003). Flow and pressure distributions in vascular networks consisting of distensible vessels. *American Journal of Anesthesia of Physiology-Heart and Circulatory Physiology*, vol. 284, pp. H2192–2203.

Lee, W.W., Mayberry, K., Crapo, R. and Jensen, R.L. (2002). The accuracy of pulse oximetry in the emergency department. *The American Journal of Emergency Medicine*, vol. 18, pp. 427–431.

Leuthner, T. (1994). Development system for pulse oximetry. *Medical and Biological Engineering and Computing*, vol. 32, pp. 596–598.

Lindberg, L.G., Vegfors, M., Lennmarken, C. and Öberg, P.A. (1995). Pulse oximeter signal at various blood flow conditions in an in vitro model. *Medical and Biological Engineering and Computing*, vol. 33, pp. 87–91.

Lindholm, P., Blogg, S.L. and Gennser, M. (2007). Pulse oximetry to detect hypoxemia during apnea: Comparison of finger and ear probes. *Aviation, Space and Environmental Medicine*, vol. 78, pp. 770–773.

Lovell, A.T., Hebden, J.C., Goldstone, J.C. and Cope, M. (1999). Determination of the transport scattering coefficient of red blood cells. *Proceedings of SPIE Optical Tomography and Spectroscopy of Tissue III*, vol. 3597, p. 175.

Lu, J.Q., Yang, P. and Hu, X. (2005). Simulations of light scattering from a biconcave red blood cell using the finite-difference time-domain method. *Journal of Biomedical Optics*, vol. 10, p. 024022.

Lutter, N., Urankar, S., Kozma, E. and Schuettler, J. (2001). Accuracy of third generation pulse oximeters at motion and low perfusion.
Available at: `http://www.anestech.org/media/Publications/Annual_2001/`

Mahmud, H.J. and Shadab, A. (2007). Meningococcemia.
Available at: `http://www.emedicine.com/med/topic1445.htm`

Mannheimer, P., Cascini, J., Fein, M. and Nierlich, S. (1997). Wavelength selection for low-saturation pulse oximetry. *IEEE Transactions on Biomedical Engineering*, vol. 44, pp. 148–158.

Mannheimer, P.D. and Porges, P.C. (2004). Pulse oximeter sensor with piece-wise function. USP6801797.

Martini, F. and Bartholomew, E. (2003). *Essentials of Anatomy and Physiology*. 3rd edn. Prentice Hall, Upper Saddle River.

Masimo Corporation (2005). Signal extraction technology.

Masimo Corporation (2006). Monitoring SpO during conditions involving low peripheral perfusion.
Available at: `http://www.masimo.com/pdf/whitepaper/LAB3692A.pdf`

Meinke, M., Müller, G., Helfmann, J. and Friebel, M. (2007). Empirical model functions to calculate hematocrit-dependent optical properties of human blood. *Applied optics*, vol. 46, pp. 1742–53.

Michel, B. (2007). Miecalc.
Available at: `http://www.lightscattering.de/MieCalc/eindex`

Milonovich, L.M. (2007). Meningococcemia: epidemiology, pathophysiology, and management. *Journal of Pediatric Health Care*, vol. 21, pp. 75–80.

Mundley, A.J., Sik, M.J. and Shaw, A. (1989). A test object for assessing pulse oximeters. *The Lancet*, pp. 1048–1049.

National Instruments Technical Communications (2006). National instruments USB-621x specifications.

Nellcor Technical Staff (2004). A technology overview of the nellcor oximax pulse oximetry system.
Available at: `http://www.nellcor.com/_Catalog/PDF/Product/OxiMaxTechNote`

Pierce, R. (1972). *An Determination of the Average Scattering and Absorption Cross Sections of Human Red Blood Cells for Near-Infrared Light.* Ph.D. thesis, University of Washington, Seattle.

Pologe, J.A. (1987). Pulse oximetry: Technical aspects of machine design. *International Anesthesiology Clinics*, vol. 25, pp. 137–53.

Prahl, S. (1998). Tabulated molar extinction coefficient for hemoglobin in water.
Available at: `http://omlc.ogi.edu/spectra/hemoglobin/summary.html`

Ramos-e-Silva, M. and Pereira, A.L.C. (2005). Life-threatening eruptions due to infectious agents. *Clinics in Dermatology*, vol. 23, pp. 148–156.

Razi, E. and Hossein, A. (2006). A comparison of arterial oxygen saturation measured both by pulse oximeter and arterial blood gas analyzer in hypoxemic and non-hypoxemic pulmonary diseases. *Turkish Respiratory Journal*, vol. 7, pp. 43–47.

Reinhart, K. and Bloos, F. (2005). The value of venous oximetry. *Current Opinion in Critical Care*, vol. 11, pp. 259–263.

Reinhart, K., Rudolph, T., Bredle, D., Hannemann, L. and Cain, S. (1989). Comparison of central-venous to mixed-venous oxygen saturation during changes in oxygen supply/demand. *Chest*, vol. 95, pp. 1216–1221.

Reynolds, K.J., Moyle, J.T.B., Sykes, M.K. and Hawn, C.E.W. (1992). Response of 10 pulse oximeters to an in vitro test system. *British Journal of Anaesthesia*, vol. 68, pp. 365–369.

Reynolds, L., Johnson, C. and Ishimaru, A. (1976). Diffuse reflectance from a finite blood medium: Applications to the modeling of fiber optic catheters. *Applied Optics*, vol. 15, pp. 2059–2067.

Reynolds, L., Molocho, J. and Ishimaru, A. (1974). Optical cross-sections of human erythrocytes. *Proceedings of the 27th Annual Conference on Engineering in Medicine and Biology*, vol. 16, p. 58.

Schallom, L., Sona, C., McSweeney, M. and Mazuski, J. (2007). Comparison of forehead and digit oximetry in surgical/trauma patients at risk for decreased peripheral perfusion. *Heart & lung: The Journal of Critical Care*, vol. 36, pp. 188–94.

Schmitt, J.M. (1991). Simple photon diffusion analysis of the effects of multiple scattering on pulse oximetry. *IEEE Transactions on Bio-Medical Engineering*, vol. 38, pp. 1194–1203.

Schmitt, J.M., Meindl, J.D. and Mihm, F.G. (1986). An integrated circuit-based optical sensor for in vivo measurement of blood oxygenation. *IEEE transactions on Biomedical Engineering*, vol. 33, pp. 98–107.

Schmitt, J.M., Zhou, G.X., Walker, E.C. and Wall, R.T. (1990). Multilayer model of photon diffusion in skin. *Journal of the Optical Society of America*, vol. 7, pp. 2141–2153.

Schuster, A. (1905). Radiation through a foggy atmosphere. *The Astrophysical Journal*, vol. 21.

Severinghaus, J.W. and Naifeh, K.H. (1987). Accuracy of response of six pulse oximeters to profound hypoxia. *Anesthesiology*, vol. 67, pp. 551–8.

Severinghaus, J.W., Naifeh, K.H. and Koh, S.O. (1989). Errors in 14 pulse oximeters during profound hypoxia. *Journal of Clinical Monitoring and Computing*, vol. 5, pp. 72–81.

Shah, N. and Estanol, L. (2006). Comparison of three new generation pulse oximeters during motion and low perfusion in volunteers. *Anesthesiology*, vol. 105, p. A929.

Shimada, Y., Yoshiya, I., Oka, N. and Hamaguri, K. (1984). Effects of multiple scattering and peripheral circulation on arterial oxygen saturation measured with a pulse-type oximeter. *Medical and Biological Engineering and Computing*, vol. 22, pp. 475–478.

Simpson, C.R., Kohl, M., Essenpreis, M. and Cope, M. (1998). Near-infrared optical properties of ex vivo human skin and subcutaneous tissues measured using the Monte Carlo inversion technique. *Physics in Medicine and Biology*, vol. 43, pp. 2465–2478.

Sinex, J.E. (1999). Pulse oximetry: Principles and limitations. *The American Journal of Emergency Medicine*, vol. 17, pp. 59–66.

Sise, M.J., Hollingsworth, P., Brimm, J.E., Peters, R.M., Virgilio, R.W. and Shackford, S.R. (1981). Complications of the flow-directed pulmonary artery catheter: A prospective analysis in 219 patients. *Critical care medicine*, vol. 9, pp. 315–8.

Stabile, N. and Reynolds, K.J. (2002). Technological review of pulse oximeter simulators. *Journal of Clinical Engineering*, vol. 27, p. 287.

Steinke, J.M. and Shepherd, A.P. (1988). Diffusion model of the optical absorbance of whole blood. *Journal of the Optical Society of America*, vol. 5, pp. 813–822.

Tremper, K.K. (1984). Transcutaneous pO2 measurement. *Canadian Anaesthetists' Society Journal*, vol. 31, pp. 664–677.

Tremper, K.K. and Barker, S.J. (1989). Pulse oximetry. *Journal of Clinical Monitoring*, vol. 70, pp. 98–108.

Uystepruyst, C.H., Coghe, J., Bureau, F. and Lekeux, P. (2000). Evaluation of accuracy of pulse oximetry in newborn calves. *Veterinary Journal*, vol. 159, pp. 71–6.

Van de Louw, A., Cracco, C., Cerf, C., Harf, A., Duvaldestin, P., Lemaire, F. and Brochard, L. (2001). Accuracy of pulse oximetry in the intensive care unit. *Intensive Care Medicine*, vol. 27, pp. 1606–13.

Villanueva, R., Bell, C., Kain, Z.N. and Colingo, K.A. (1999). Effect of peripheral perfusion on accuracy of pulse oximetry in children. *Journal of Clinical Anesthesia*, vol. 11, pp. 317–22.

Vining, G. (1997). *Statistical Methods for Engineers*. 1st edn. Duxbury Press, CA.

Volgyesi, G.A., Kolesar, R. and Lerman, J. (1990). An in vitro model for evaluating the accuracy of pulse oximeters. *Canadian Journal of Anaesthesia*, vol. 37, p. S67.

Wahr, J.A. and Tremper, K.K. (1995). Noninvasive oxygen monitoring techniques. *Critical Care Clinics*, vol. 11, pp. 199–217.

Webster, J.G. (1997). *Design of Pulse Oximeters*. 1st edn. Taylor & Francis.

Wener, K. (2005). Meningococcemia.
Available at: `http://www.healthline.com/adamcontent/meningococcemia`

Wukitsch, M.W., Petterson, M.T., Tobler, D.R. and Pologe, J.A. (1988). Pulse oximetry: Analysis of theory, technology, and practice. *Journal of Clinical Monitoring and Computing*, vol. 4, pp. 290–301.

Yoxall, C. and Weindling, A. (1996). The measurement of peripheral venous oxyhemoglobin saturation in newborn infants by near infrared spectroscopy with venous occlusion. *Pediatric Research*, vol. 39, pp. 1103–1106.

Yoxall, C.W. and Weindling, A.M. (1997). Measurement of venous oxyhaemoglobin saturation in the adult human forearm by near infrared spectroscopy with venous occlusion. *Medical and Biological Engineering and Computing*, vol. 35, pp. 331–336.

Zhou, G.X., Schmitt, J.M. and Walker, E.C. (1993). Electro-optical simulator for pulse oximeters. *Medical and Biological Engineering and Computing*, vol. 31, pp. 534–539.

Zonios, G., Shankar, U. and Iyer, V. (2004). Pulse oximetry theory and calibration for low saturations. *IEEE Transactions on Biomedical Engineering*, vol. 51, pp. 818–822.

Appendices

Appendix A

Datasheets

SMD LED ELS-740-994

Radiation	Type	Technology	Case
Infrared	TOP LED	AlGaAs/AlGaAs	PLCC-2

Description
High-power, high-speed,
double heterostructure with removed substrate

Applications
Optical communications,
safety equipment, automation

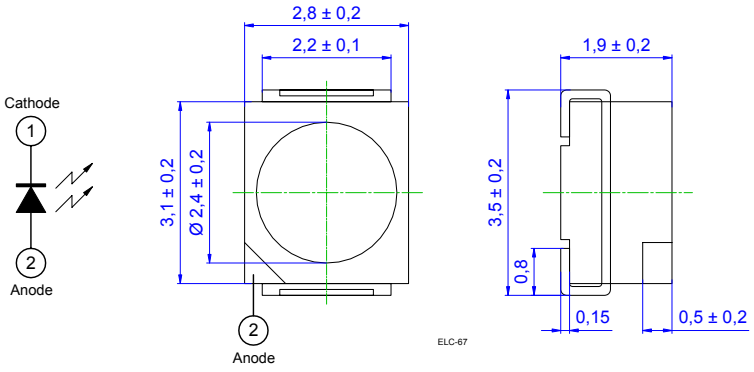

Maximum Ratings
T_{amb} = 25°C, unless otherwise specified

Parameter	Test conditions	Symbol	Value	Unit
Forward current (DC)		I_F	50	mA
Peak forward current	($t_P \leq 50$ µs, t_P/T = 1/2)	I_{FM}	100	mA
Surge forward current	($t_P \leq 10$ µs)	I_{FSM}	1000	mA
Reverse voltage	I_R=100 µA	V_R	5	V
Operating temperature range		T_{amb}	-40...+85	°C
Storage temperature range		T_{stg}	-40…+90	°C

Optical and Electrical Characteristics
T_{amb} = 25°C, unless otherwise specified

Parameter	Test conditions	Symbol	Min	Typ	Max	Unit
Forward voltage	I_F = 50 mA	V_F		2.0	2.5	V
Radiant power	I_F = 50 mA	Φ_e		6.5		mW
Peak wavelength	I_F = 50 mA	λ_p		740		nm
Spectral bandwidth at 50%	I_F = 50 mA	$\Delta\lambda_{0.5}$		30		nm
Viewing angle	I_F = 50 mA	2φ		120		deg.
Switching time	I_F = 50 mA	t_r, t_f		30		ns

rev.07/05

EPIGAP Optoelektronik GmbH, D-12555 Berlin, Köpenicker Str. 325 b, Hs. 201, Tel.: +49-30-6576 2543, Fax.: +49-30-6576 2545

Figure A.1: ELS-740-994 Datasheet

SMD LED ELS-880-894-3

Radiation	Type	Technology	Case
Infrared	SMD	AlGaAs/AlGaAs	0805

Description
High-power, high-speed,
double heterostructure with removed substrate

Applications
Optical communications,
safety equipment, automation

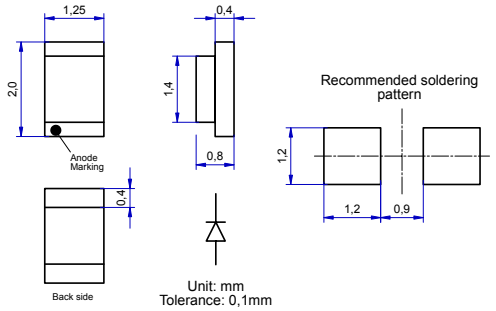

Maximum Ratings
T_{amb} = 25°C, unless otherwise specified

Parameter	Test conditions	Symbol	Value	Unit
Forward current (DC)		I_F	50	mA
Peak forward current	($t_P \leq 100$ µs, $t_P/T = 1/10$)	I_{FM}	100	mA
Peak forward current	($t_P \leq 100$ µs, $t_P/T = 1/100$)	I_{FM}	500	mA
Reverse voltage	I_R = 100 µA	V_R	5	V
Power dissipation		P_D	80	mW
Operating temperature range		T_{amb}	-40...+85	°C
Storage temperature range		T_{stg}	-55…+85	°C

Optical and Electrical Characteristics
T_{amb} = 25°C, unless otherwise specified

Parameter	Test conditions	Symbol	Min	Typ	Max	Unit
Forward voltage	I_F = 50 mA	V_F		1.4	1.9	V
Radiant power	I_F = 20 mA	Φ_e		4.8		mW
Radiant power	I_F = 50 mA	Φ_e		12		mW
Radiant intensity	I_F = 20 mA	I_e		1.2		mW/sr
Radiant intensity	I_F = 50 mA	I_e		4.0		mW/sr
Peak wavelength	I_F = 50 mA	λ_p	860	875	890	nm
Viewing angle	I_F = 50 mA	φ		120		deg.
Switching time	I_F = 100 mA	t_r, t_f		25		ns

rev.08/02

EPIGAP Optoelektronik GmbH, D-12555 Berlin, Köpenicker Str. 325 b, Hs. 201, Tel.: +49-30-6576 2543, Fax.: +49-30-6576 2545

Figure A.2: ELS-880-894-3 Datasheet

Appendix B

Circuit Diagrams

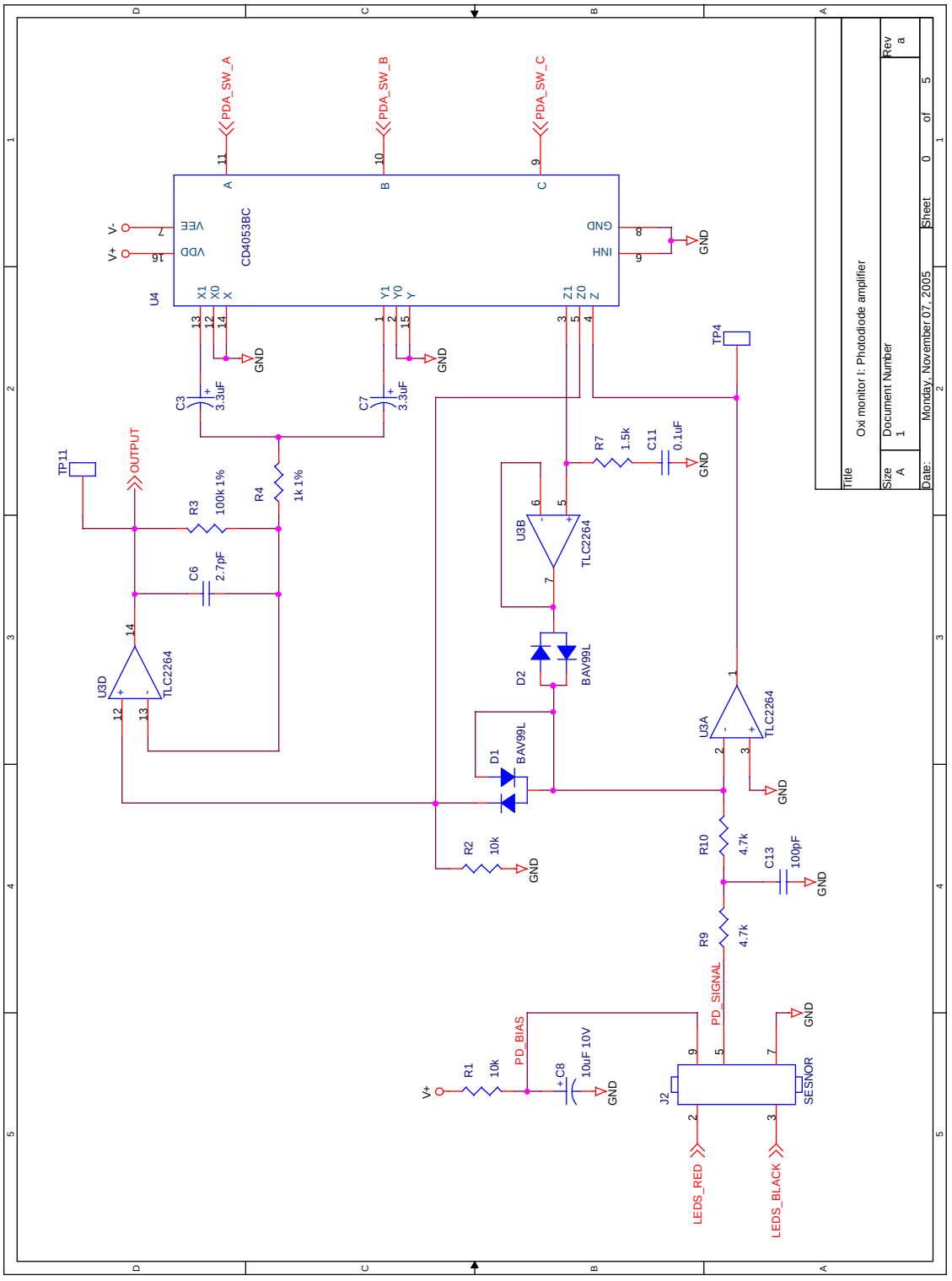

Figure B.1: Photodiode Amplifier (Orcad Capture)

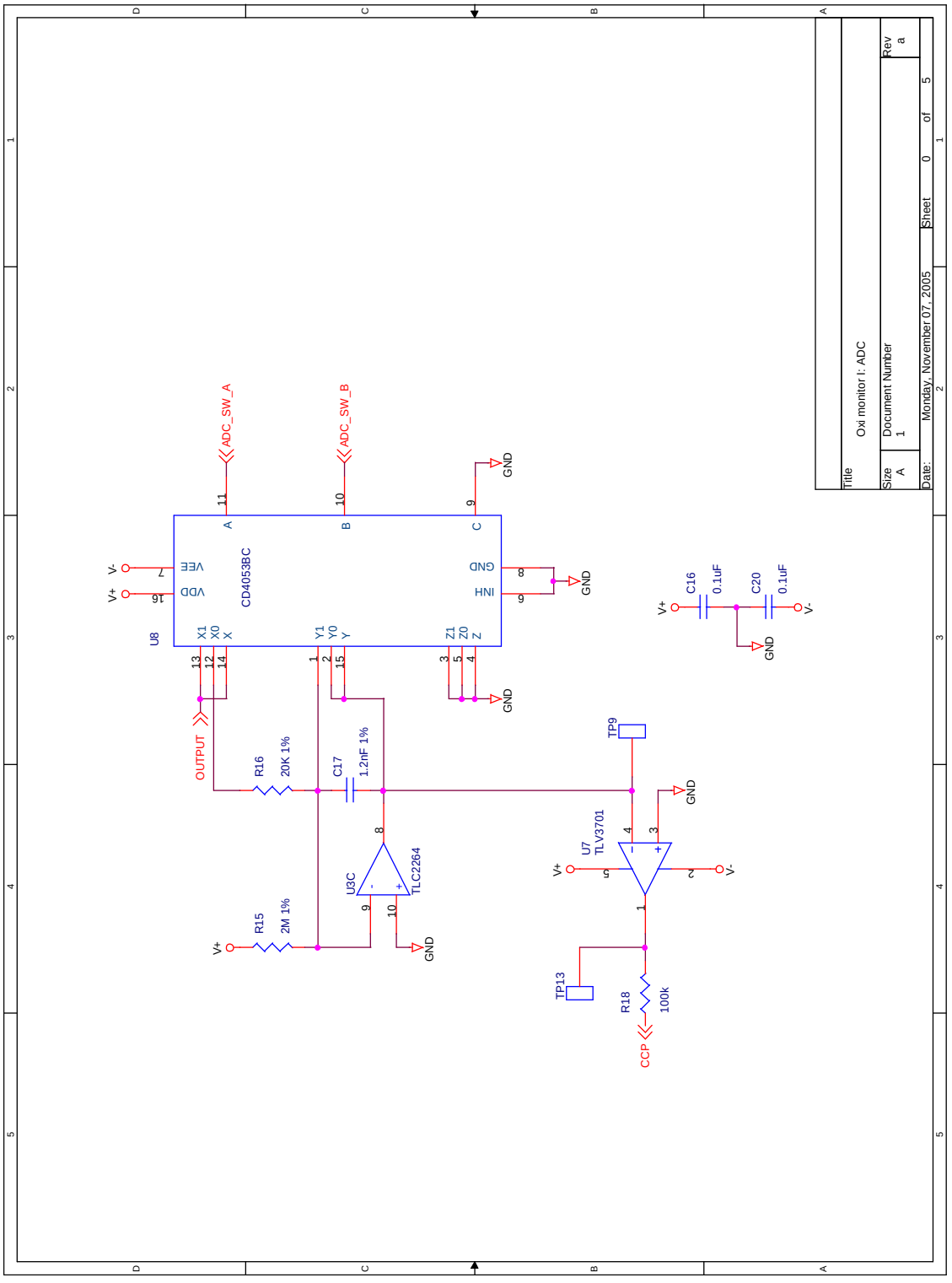

Figure B.2: A/D Converter Base (Orcad Capture)

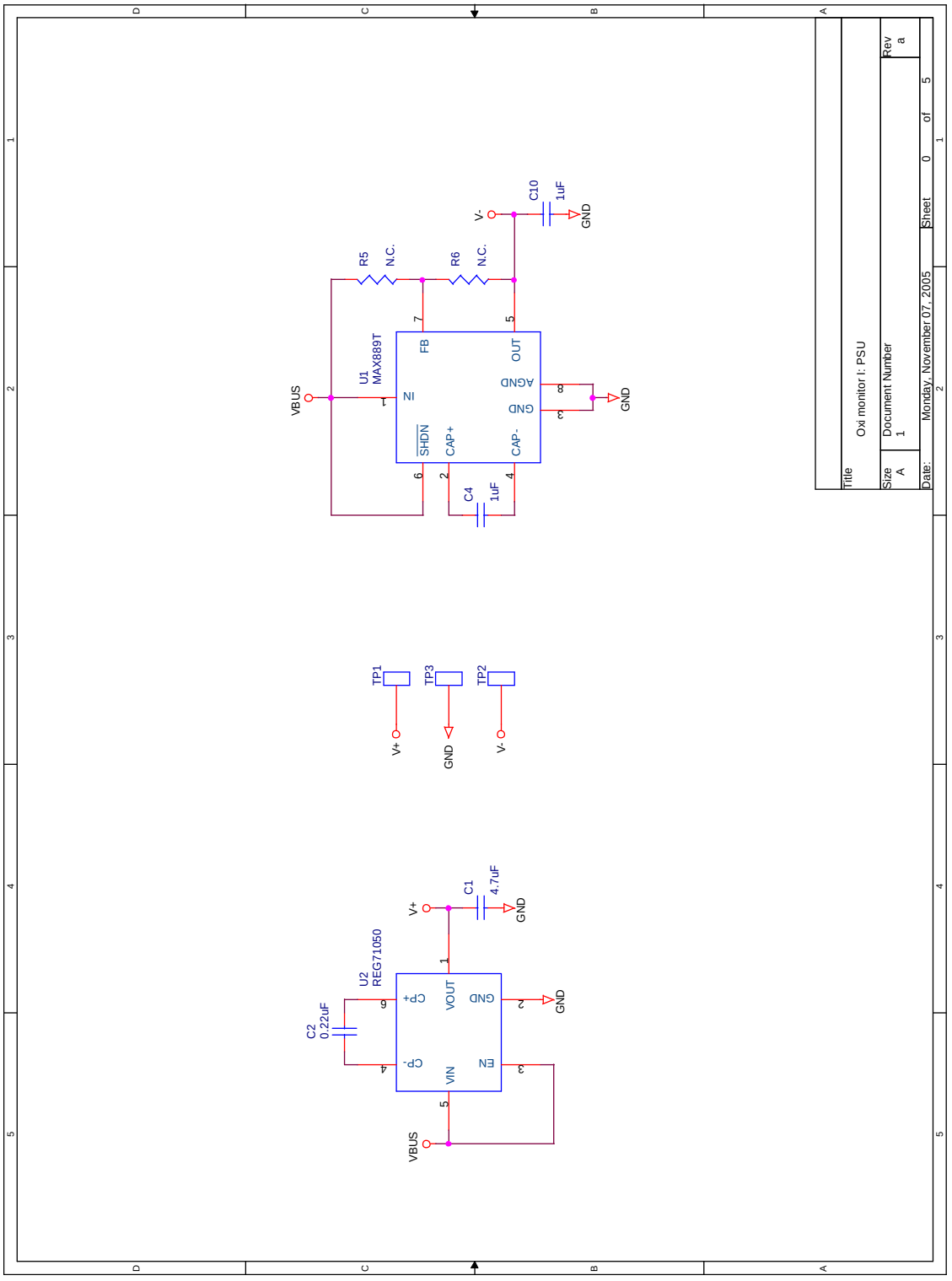

Figure B.3: Power Supply Unit (Orcad Capture)

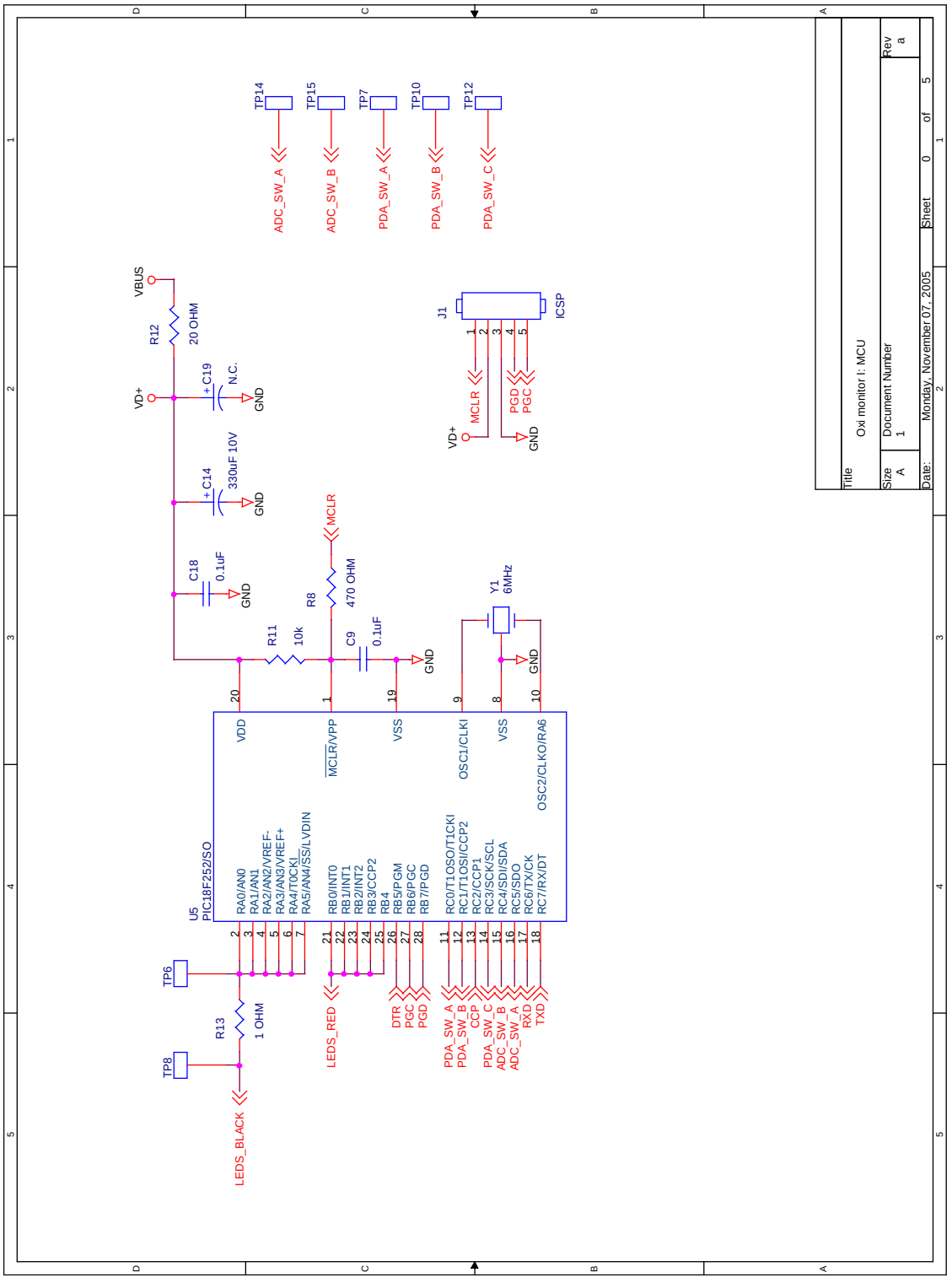

Figure B.4: Microcontroller Unit (Orcad Capture)

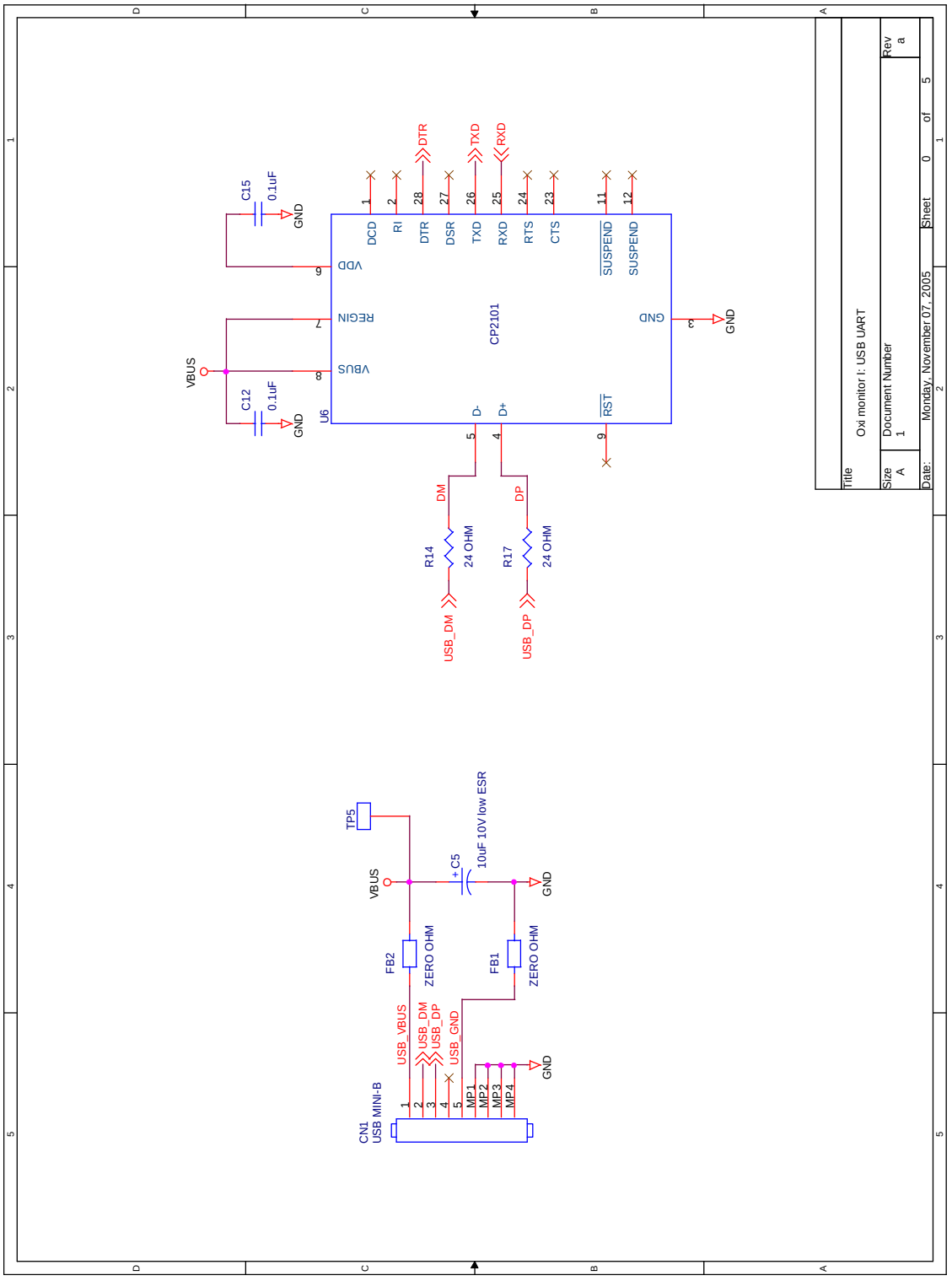

Figure B.5: USB Universal Asynchronous Receiver/Transmitter (Orcad Capture)

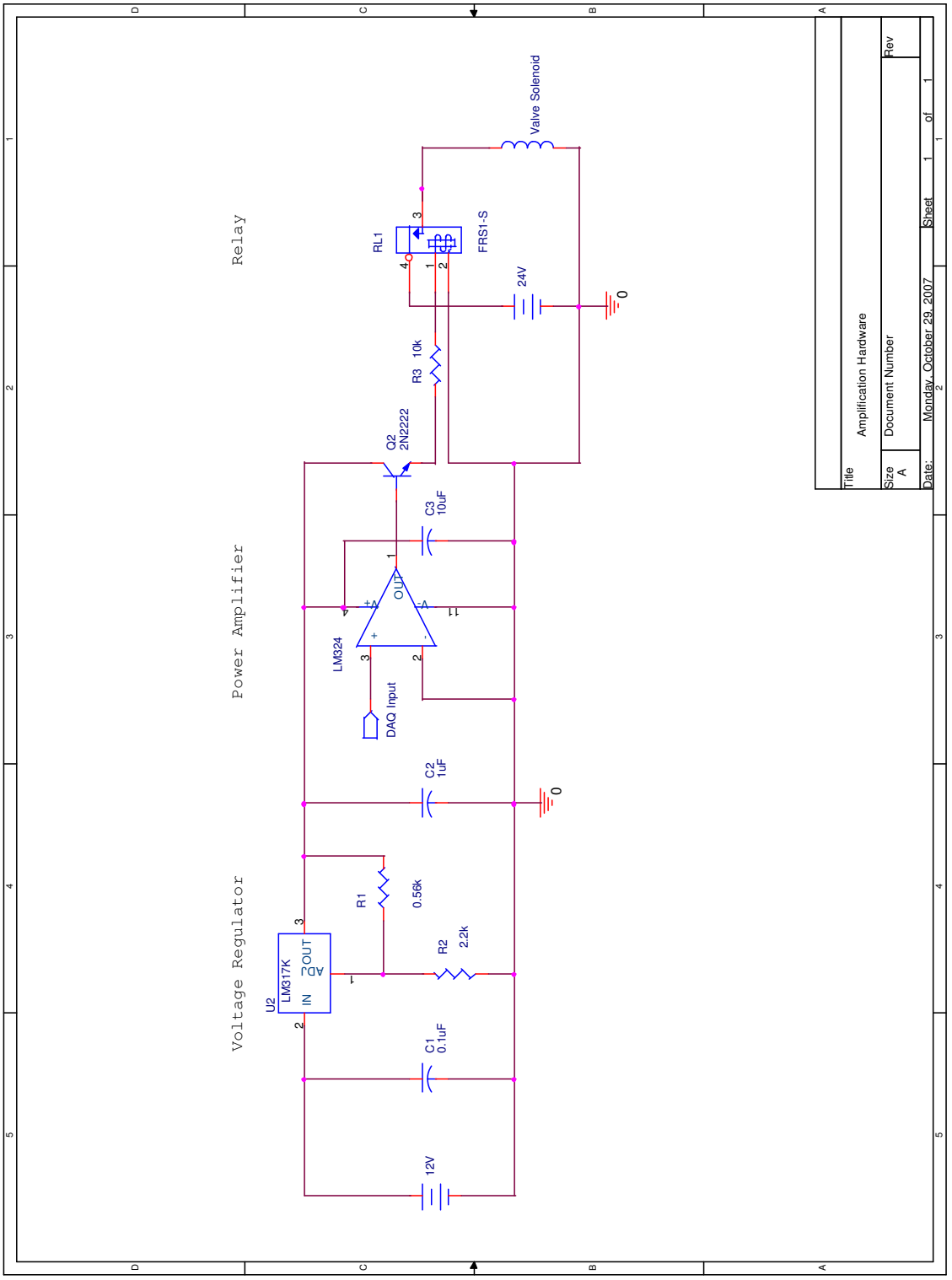

Figure B.6: Output Amplifier (Orcad Capture)

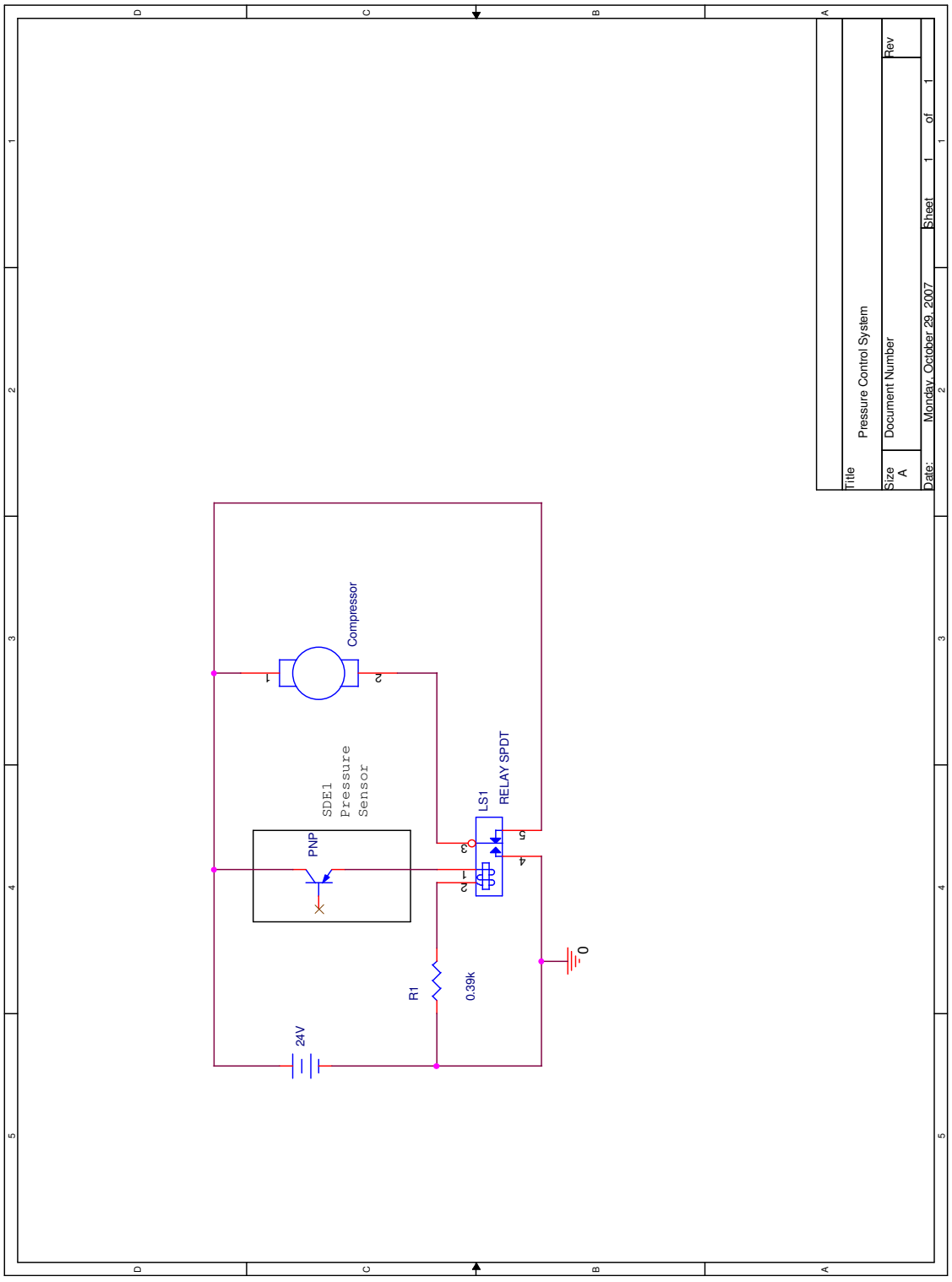

Figure B.7: Pressure Control System (Orcad Capture)

Appendix C

Mechanical Components

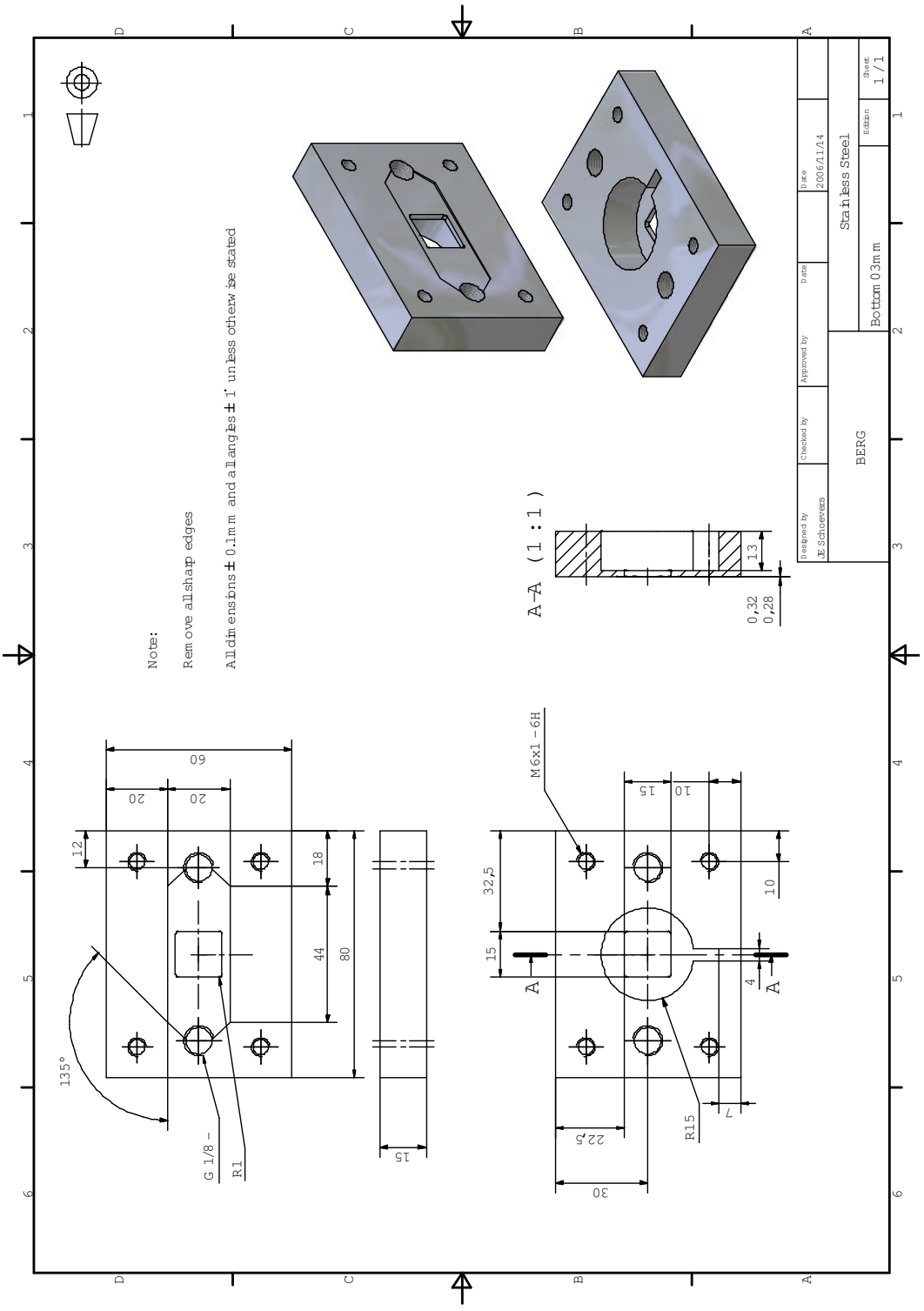

Figure C.1: Top *Cuvette* Component (AutoDesk Inventor 9)

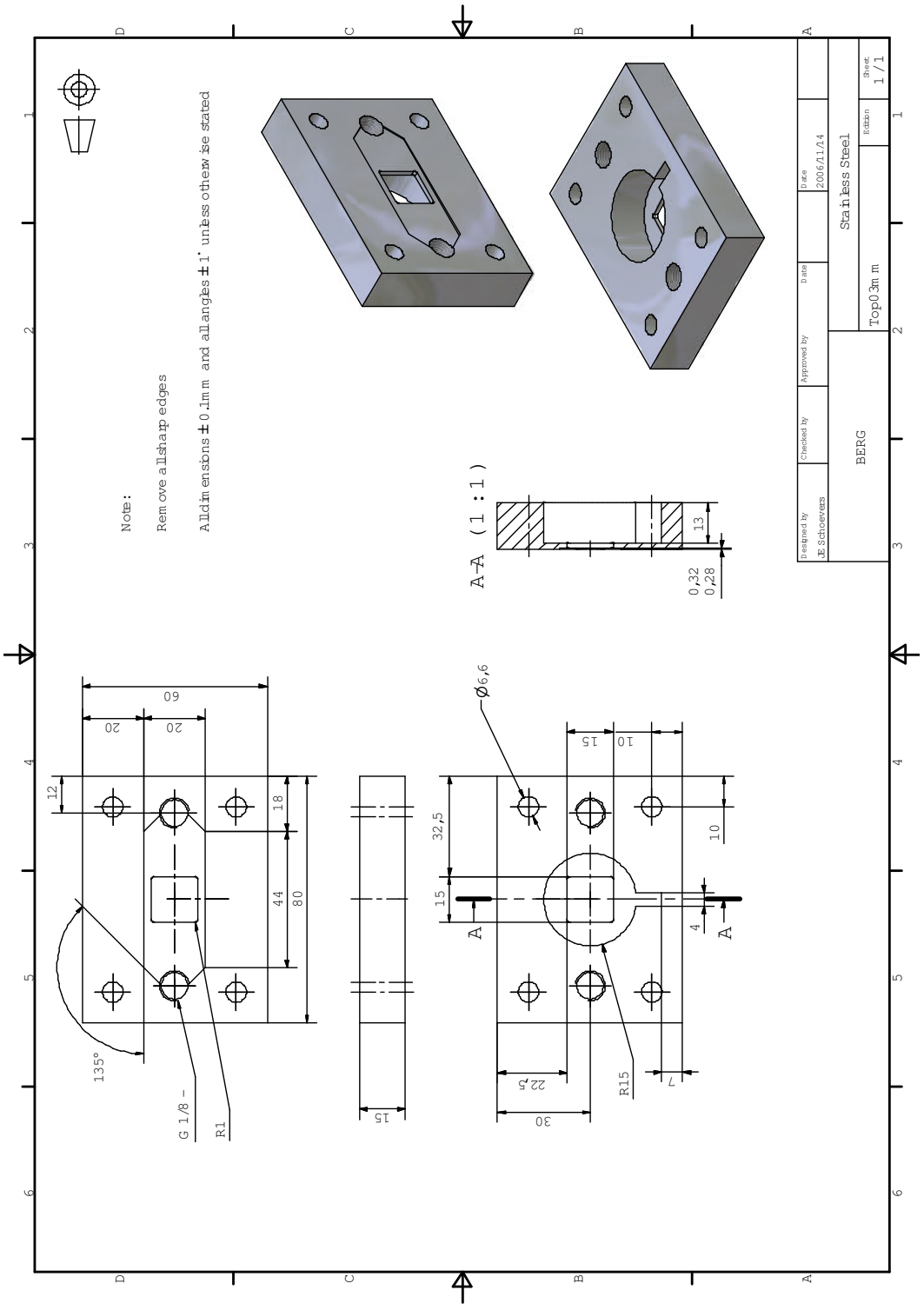

Figure C.2: Base *Cuvette* Component (AutoDesk Inventor 9)

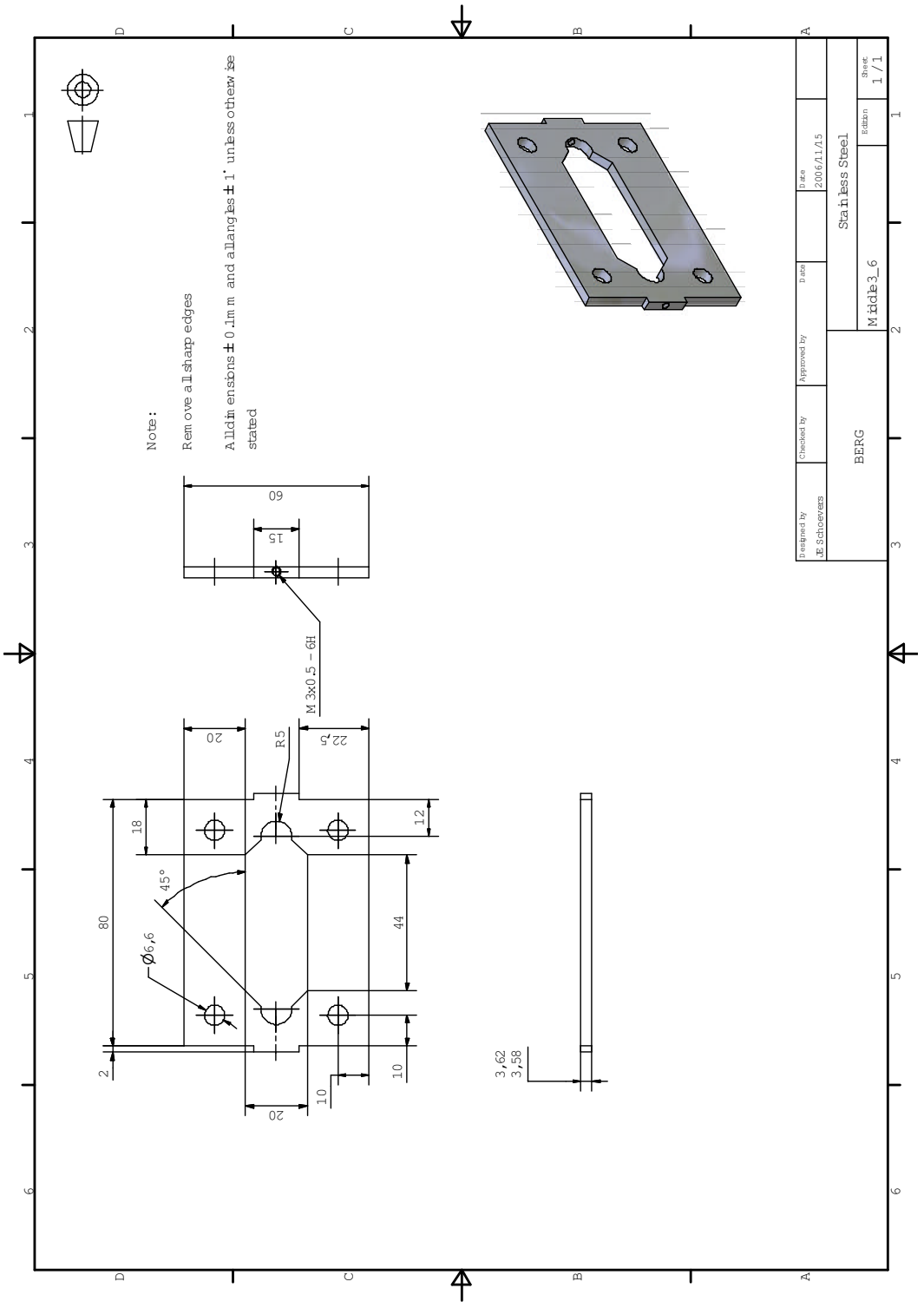

Figure C.3: Middle *Cuvette* Component (AutoDesk Inventor 9)

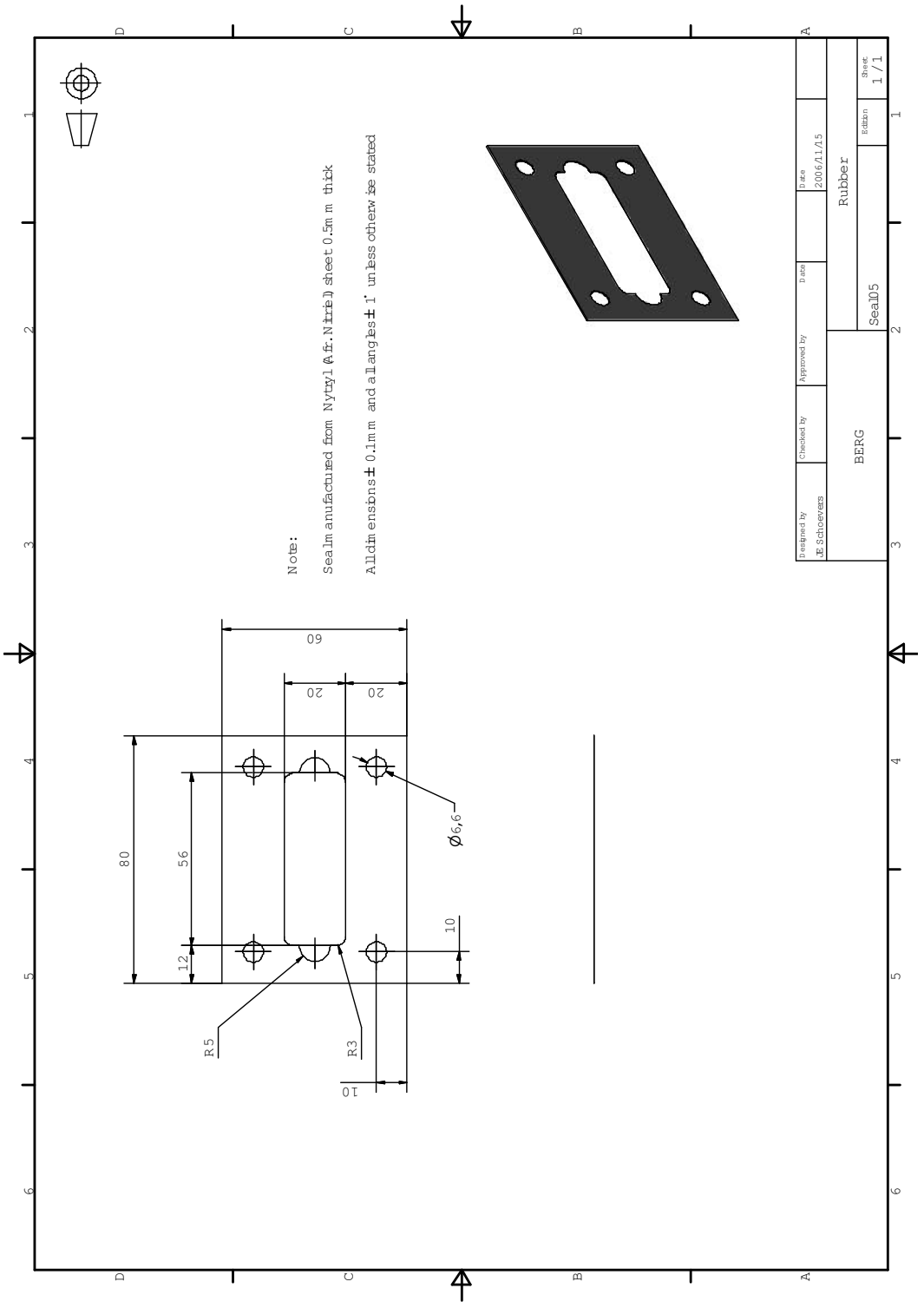

Figure C.4: *Cuvette* Seal (AutoDesk Inventor 9)

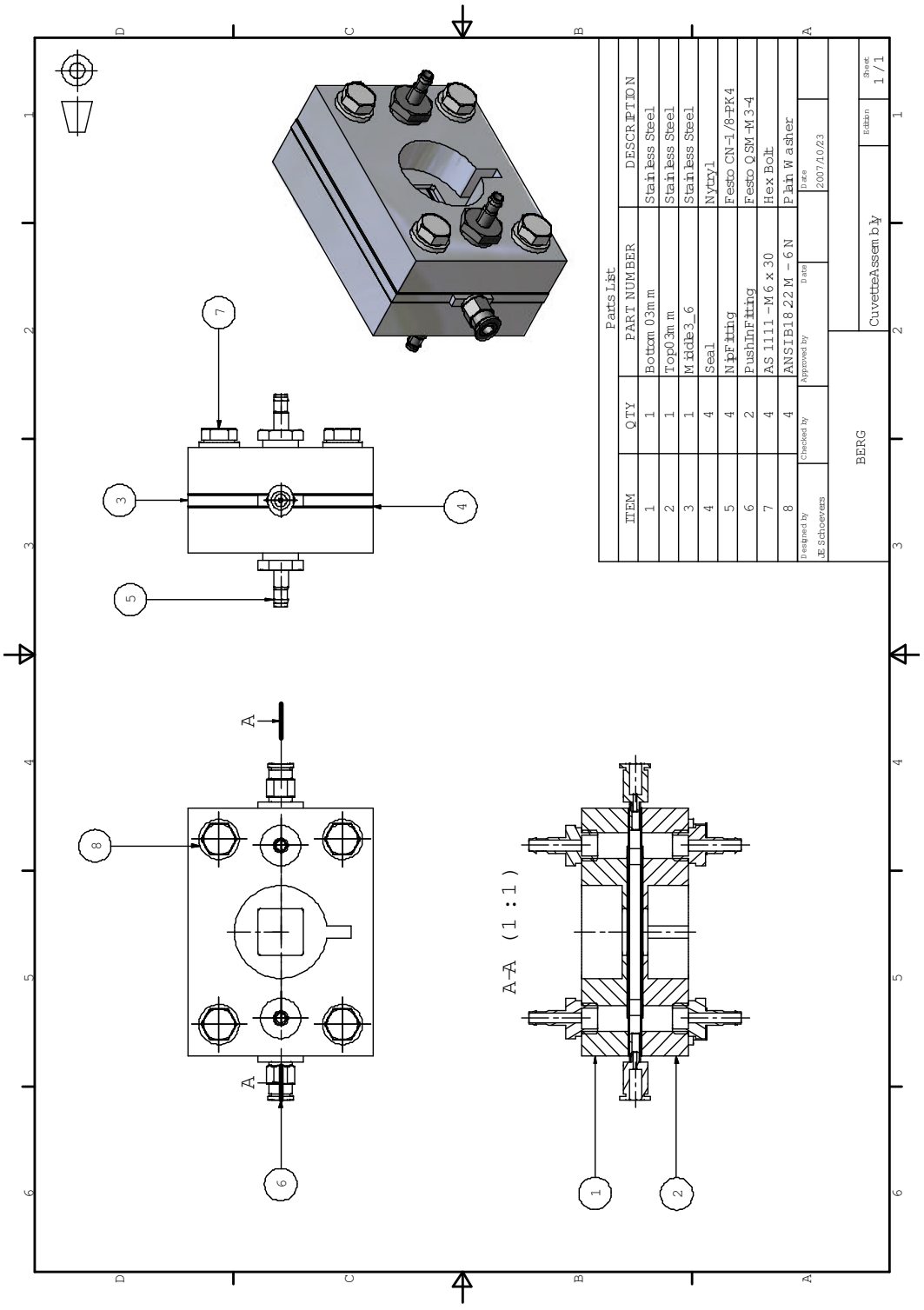

Figure C.5: *Cuvette* Assembly (AutoDesk Inventor 9)

Table C.1: Part Catalogue Numberss

Part	System	Supplier	Catalogue ID	#
Compressor	APG	Mantech Elec.	QJT-27QB	2
Non-return Valve	APG	Festo	H-QS-6	2
T-Fitting	APG	Festo	TJK-1/4	1
Push-in Fitting	APG	Festo	QS-1/4-4	1
Push-in Fitting	APG	Festo	QS-1/4-6	3
Push-in Fitting	APG	Festo	QS-1/8-4	1
Push-in Fitting	APG	Festo	QS-1/8-6	1
Push-in Fitting	APG	Festo	QS-M5-6	3
Sleeve	APG	Festo	QM-1/4-1/4	1
Accumulator	APG	Festo	CRVZ5-0.4	1
Pressure Sensor	APG	Festo	SDE1-D2-G2-WQ4-C-P2-M8	1
Pressure Lead	APG	Festo	SIM-M8-4GD-2.5-PU	1
Valve Bank	APG	Festo	BMFH-3-5-M5	1
Valve Solenoid	APG	Festo	MSFG-24DC/42AC	3
Solenoid Lead	APG	Festo	KMF-1-24DC-2.5-LED	3
Flow Regulator	APG	Festo	GR-QS-6-LF	3
Relay	APG	Mantech Elec.	FRS1-S	4
Sleeve	Pressure Cuff	Festo	QM-1/8-1/8	3
Push-in Fitting	Pressure Cuff	Festo	QS-1/8-6	3
Barbed Fitting	Pressure Cuff	Festo	CN-1/8-PK6	3
Push-in Fitting	Cuvette	Festo	QSM-M3-4	2
Barbed Fitting	Cuvette	Festo	CN-1/8-PK4	2

Appendix D

Numerical *In Vivo* Validation Results

Table D.1: *In Vivo* Validation Results for High SO_2

Subject	Trial #	Signal Quality[a]	R Stability[a]	$S_{pa}O_2$ Curve	Δ	Sim[b]	Δ	Reference $S_{ca}O_2$
1	1	+	0	96	0	95	-1	96
2	1	+	0	89	-7	87	-9	96
2	2	+	+	90	-6	89	-7	96
2	3	0	+	92	-4	91	-5	96
3	1	-	-	-	-	-	-	92
4	1	-	-	-	-	-	-	95
5	1	0	0	91	-2	89	-4	93
5	2	+	-	83	-10	80	-13	93
5	3	+	0	89	-4	87	-6	93
5	4	0	0	91	-2	90	-3	93
6	1	+	+	96	-1	95	-2	97
6	2	+	+	95	-2	95	-2	97
6	3	+	+	95	-2	94	-3	97
7	1	+	+	90	-5	89	-6	95
7	2	+	+	89	-6	87	-8	95
7	3	+	+	90	-5	88	-7	95
8	1	+	+	91	-3	90	-4	94
8	2	+	+	92	-2	91	-3	94
8	3	+	0	88	-6	86	-8	94
8	4	0	+	92	-2	91	-3	94
9	1	+	+	93	-2	92	-3	95
9	2	+	+	91	-4	90	-5	95
9	3	+	+	88	-7	85	-10	95
10	1	+	+	92	-2	91	-3	94
10	2	0	+	92	-2	91	-3	94
10	3	+	0	91	-3	90	-4	94
11	1	0	+	91	-3	90	-4	94
11	2	0	+	91	-3	89	-5	94
12	1	-	-	85	-11	82	-14	96
12	2	+	0	82	-14	78	-18	96
12	3	0	-	83	-13	80	-16	96

[a](+) Good; (0) Average; (-) Bad
[b]Simulation variable values dependent on subject

Table D.2: *In Vivo* Validation Results for Low SO_2 (660/910 nm)

Subject	Trial #	Signal Quality[a]	R Stability[a]	$S_{pg}O_2$				Reference $S_{cg}O_2$
				Curve	Δ	Sim[b]	Δ	
1	1	-	-	0	-32	0	-32	32
2	1	-	-	10	-32	0	-42	42
3	1	0	-	66	+34	63	+31	32
4	1	0	-	37	-24	39	-22	61
4	2	+	+	42	-19	43	-18	61
5	1	+	0	31	-20	14	-37	51
6	1	+	0	0	-30	0	-30	30
7	1	+	-	27	0	9	-18	27
7	2	+	+	40	+17	23	-4	27
8	1	-	-	44	+25	26	+7	19
9	-	-	-	-	-	-	-	-
10	1	0	-	19	-20	0	-39	39
11	1	+	+	62	+9	50	-3	53
12	1	+	+	65	+31	53	+19	34?

[a](+) Good; (0) Average; (-) Bad
[b]Simulation variable values dependent on subject

Table D.3: *In Vivo* Validation Results for Low SO_2 (740/880 nm)

Subject	Trial #	Signal Quality[a]	R Stability[a]	$S_{pg}O_2$				Reference $S_{cg}O_2$
				Curve	Δ	Sim[b]	Δ	
1	1	0	-	85	+53	50	-18	32
2	1	+	+	26	-16	0	-42	42
3	1	-	-	7	-25	0	-32	32
4	1	+	+	29	-32	0	-61	61
4	2	+	+	18	-43	0	-61	61
5	1	+	+	21	-30	0	-51	51
6	1	+	+	9	-21	0	-30	30
6	2	+	+	11	-19	0	-30	30
7	1	+	+	34	+7	2	-25	27
7	2	0	+	37	+10	5	-22	27
8	1	0	+	0	-19	0	-19	19
8	2	0	0	14	-5	0	-19	19
9	-	-	-	-	-	-	-	-
10	1	0	+	19	-20	0	-39	39
10	2	+	+	4	-35	0	-39	39
11	1	+	+	35	-18	2	-51	53
11	2	+	+	39	-14	5	-48	53
12	1	0	+	25	-9	0	-34	34?
12	2	+	+	25	-9	0	-34	34?

[a](+) Good; (0) Average; (-) Bad
[b]Simulation variable values dependent on subject

Table D.4: *In Vivo* Arterio-Venous Validation Results

Subject	Trial #	Signal Quality[a]	R Stability[a]	$S_{pv}O_2$				Reference $S_{cv}O_2$
				Curve	Δ	Sim[b]	Δ	
1	1	+	+	83	+1	73	-9	82
2	1	0	-	51	-31	37	-45	82
2	2	0	+	72	-10	60	-22	82
3	1	0	0	72	+12	59	-1	60
4	1	0	0	78	+10	66	-2	68
5	1	+	+	79	+2	67	-10	77
6	1	0	+	94	+6	89	+1	88
7	1	-	-	87	-6	76	-17	93
8	1	0	0	78	-6	64	-20	84
9	1	+	+	80	-3	67	-16	83
9	2	+	+	55	-28	40	-43	83
10	1	-	-	80	-1	68	-13	81
11	1	0	-	56	-36	40	-52	92
11	2	+	-	0	-92	0	-92	92
12	1	0	-	42	-39	30	-51	81
12	2	0	-	44	-37	31	-50	81

[a](+) Good; (0) Average; (-) Bad
[b]Simulation variable values dependent on subject